AERODYNAMIC AND AEROELASTIC RESPONSES OF A NACA0012 WING IN STALL CONDITIONS TO EXTERNAL HARMONIC FLOW EXCITATION

RÉPONSES AÉRODYNAMIQUES ET AÉROÉLASTIQUES D'UNE AILE NACA0012 EN CONDITIONS DE DÉCROCHAGE SOUMISE À UNE EXCITATION HARMONIQUE D'ÉCOULEMENT EXTERNE

Doctor of Philosophy
in
Mechanical Engineering

March 2026

By

Xiaoyang Zhang

Dissertation Committee:
Dr. Thomas Krause
Dr. Dominique Poirel
Dr. Weixing Yuan (NRC)
Dr. Amor Jnifene
Dr. Shem Lau-Chapdelaine
Dr. Frederick Gosselin (Poly Montréal)

This dissertation is submitted for the degree of
Doctor of Philosophy

ABSTRACT

This thesis investigates the aerodynamic and aeroelastic responses of an airfoil to harmonic gusts at transitional Reynolds numbers ($Re_c \approx 10^5$). Combining low-speed wind tunnel experiments with high-fidelity numerical simulations and reduced-order modeling, the study characterizes the interaction between unsteady flows and wing response across three distinct configurations.

First, the aerodynamic response of a stationary wing to harmonic transverse gusts is examined, with a focus on gust-induced dynamic stall. In the pre-stall regime, the measured lift aligns with linear predictions from Küssner's and Sears functions. However, around static stall, transverse gusts drive the wing into deep post-stall, inducing pronounced nonlinear effects including lift enhancement and hysteresis. By defining an effective angle of attack that incorporates the gust angle, the study demonstrates a strong analogy between gust-induced and classical pitch-induced dynamic stall, attributed to the alternating upwash and downwash inherent in the gust field. Concurrent numerical simulations provide flow structure evolution of the dynamic stall process, which aids in a deeper understanding of the phenomenon.

Subsequently, the research extends to aeroelastic interactions, examining a one-degree-of-freedom (one-DOF) pitch oscillator undergoing stall flutter under transverse gust excitation. Two distinct response regimes are documented: quasi-periodic beating out of synchronization, and a finite 1:1 lock-in band in which the pitch frequency synchronizes with the gust. A forced van der Pol (F-VdP) oscillator is employed to model this behavior. The model successfully reproduces essential experimental features, including the synchronization window and the qualitative dependence on forcing and oscillation amplitude levels, consistent with the system behaving as a limit-cycle oscillator under external forcing.

Finally, the study addresses the less-explored domain of harmonic longitudinal (streamwise) gusts. In contrast to the transverse case, the response to longitudinal gusts exhibits features of a parametric modulation mechanism: a 2:1 lock-in band and a distinct spectral peak of beating. The system is modeled using a minimal Mathieu-type van der Pol (M-VdP) oscillator featuring stiffness modulation, whose numerical solutions are validated by experimental observations. The minimal model also predicts behavior beyond the experimental constraints, on a sound theoretical basis.

Collectively, this work advances the understanding of underexplored gust-induced nonlinear aerodynamics and aeroelastic phenomena. It provides new physical insights into gust-airfoil coupling, which are relevant to the design of rotorcraft, unmanned aerial vehicles (UAVs), and wind-turbine blades operating in unsteady inflow conditions.

RÉSUMÉ

Cette thèse étudie les réponses aérodynamiques et aéroélastiques d'un profil d'aile soumis à des rafales harmoniques à des nombres de Reynolds de transition ($Re_c \approx 10^5$). En combinant des expériences en soufflerie à basse vitesse avec des simulations numériques de haute fidélité et une modélisation d'ordre réduit, l'étude caractérise l'interaction entre les écoulements instationnaires et la réponse de l'aile à travers trois configurations distinctes.

Premièrement, la réponse aérodynamique d'une aile fixe à des rafales transversales harmoniques est examinée, avec un accent particulier sur le décrochage dynamique induit par la rafale. Dans le régime de pré-décrochage, la portance mesurée concorde avec les prédictions linéaires des fonctions de Küssner et de Sears. Cependant, au voisinage du décrochage statique, les rafales transversales entraînent l'aile dans un régime de décrochage profond, induisant des effets non linéaires marqués, notamment une augmentation de la portance et de l'hystérésis. En définissant un angle d'attaque effectif qui intègre l'angle de la rafale, l'étude démontre une forte analogie entre le décrochage dynamique induit par la rafale et le décrochage dynamique classique induit par le tangage, attribuée à l'alternance des courants ascendants et descendants inhérents au champ de rafales. Des simulations numériques concomitantes permettent de suivre l'évolution de la structure de l'écoulement lors du processus de décrochage dynamique, facilitant ainsi une compréhension approfondie du phénomène.

Par la suite, la recherche s'étend aux interactions aéroélastiques en examinant un oscillateur de tangage à un degré de liberté (1-DDL) subissant un flottement de décrochage sous l'excitation d'une rafale transversale. Deux régimes de réponse distincts sont documentés : un battement quasi-périodique hors synchronisation, et une bande de synchronisation finie 1:1 dans laquelle la fréquence de tangage se synchronise avec la rafale. Un oscillateur de van der Pol forcé (F-VdP) est employé pour modéliser ce comportement. Le

modèle reproduit avec succès les caractéristiques expérimentales essentielles, notamment la fenêtre de synchronisation et la dépendance qualitative vis-à-vis des niveaux de forçage et d'amplitude d'oscillation, confirmant que le système se comporte comme un oscillateur à cycle limite sous forçage externe.

Enfin, l'étude aborde le domaine moins exploré des rafales longitudinales (sens de l'écoulement) harmoniques. Contrairement au cas transversal, la réponse aux rafales longitudinales présente les caractéristiques d'un mécanisme de modulation paramétrique : une bande de synchronisation 2:1 et un pic spectral de battement distinct. Le système est modélisé à l'aide d'un oscillateur de van der Pol de type Mathieu (M-VdP) minimal présentant une modulation de raideur, dont les solutions numériques sont validées par les observations expérimentales. Ce modèle minimal prédit également des comportements au-delà des contraintes expérimentales, sur une base théorique solide.

Collectivement, ce travail fait progresser la compréhension des phénomènes aérodynamiques non linéaires et aéroélastiques induits par les rafales. Il apporte de nouveaux éclairages physiques sur le couplage rafale-profil d'aile, particulièrement pertinents pour la conception de giravions, de drones (UAV) et de pales d'éoliennes opérant dans des conditions d'écoulement instationnaires.

ACKNOWLEDGMENTS

First and foremost, I would like to express my deepest gratitude to my supervisors, Dr. Dominique Poirel and Dr. Weixing Yuan, for their invaluable guidance, patience, rigor, and continuous support throughout this research.

Dr. Poirel's deep insight into unsteady aerodynamics and nonlinear dynamics was instrumental in shaping the direction of this thesis. I am particularly grateful for the freedom he encouraged for me to explore beyond conventional boundaries and to push past my current understanding. My PhD program would not have been possible without the opportunity at NRC that Dr. Yuan provided prior to my admission to RMC. Throughout my PhD, his guidance extended well beyond academic research.

I would like to thank the members of my dissertation committee for their time, careful reading and constructive feedback, which helped improve the quality of this work. I am grateful for their thoughtful questions and suggestions during the examination process.

I am grateful to Prof. Azemi Benaïssa for guidance on experimental equipment and for valuable discussions throughout this research. I also thank the technicians at the RMC workshop, for their diligent assistance in fabricating the experimental rigs.

The author also acknowledges the financial support of the National Research Council Canada, the Natural Sciences and Engineering Research Council of Canada, and the Department of National Defence.

Finally, I dedicate this work to my family. I would like to thank my parents for their unwavering support, and my partner, Xixi Guo, for her love, companionship, and encouragement throughout this journey.

SELECTED PUBLICATIONS

The research presented in this thesis has yielded several peer-reviewed journal articles and presentations at international conferences. During the PhD candidacy, the author also contributed to two additional peer-reviewed journal articles as a co-author. While these latter works represent significant contributions to the fields of unsteady aerodynamics and aeroelasticity, they are not included in the main body of this thesis to maintain its thematic focus.

Journal Publications (First Author)

- Lock-in during stall flutter under parametric excitation by harmonic longitudinal gusts. *Journal of Fluid Mechanics*, under revision, 2026.
- Lock-in during stall flutter forced by periodic transverse gusts. *Journal of Fluids and Structures*, under review, 2026.
- Dynamic stall induced by a periodic transverse gust of an airfoil at transitional Reynolds numbers. *Physics of Fluids*, vol. 37, no. 12, 2025.

Journal Publications (Second Author)

- Numerical modeling of aerodynamic response to gusts and gust effect mitigation. *Aerospace Science and Technology*, vol. 154, Art. no. 109467, 2024.
- Numerical stabilization for flutter analysis procedure. *Aerospace*, vol. 10, no. 3, Art. no. 302, 2023.

Selected Conference Proceedings/Presentations

- Stall Flutter Response to Longitudinal Gusts at Transitional Reynolds Numbers. *The 7th Symposium on Flow-Induced Vibration and Fluid-Structure Interaction (FSSIC 2025)*, Oshawa, ON, 2025.
- Experimental Investigation of Lock-In During Stall Flutter Forced by Transverse Harmonic Gust. *AIAA SciTech 2025 Forum*, Orlando, FL, 2025.
- Aerodynamic Response to Transverse Gusts in Pre- and Post-stall Regimes. *AIAA SciTech 2024 Forum*, Orlando, FL, 2024.
- Study of the Wake Flow Downstream of Two Oscillating Vanes. *CSME-CFD 2023 Congress*, Sherbrooke, QC, 2023.
- Numerical Simulation of Gust Response of a One-DOF Wing in Stall Flutter. *CASI AERO 2021 Conference (Virtual)*, 2021.

A comprehensive record of the author's journal articles and conference proceedings/ presentations is detailed in the Appendix A.

TABLE OF CONTENTS

LIST OF TABLES

LIST OF FIGURES

NOMENCLATURE

Latin symbols

b	Half-chord, $b = c/2$. [m]
c	Chord length (generic). [m]
c_V	Vane chord length. [m]
c_W	Wing chord length. [m]
C_D	Drag coefficient. [–]
C_L	Lift coefficient. [–]
C_M	Pitching-moment coefficient (e.g., about $0.25c$ or $0.30c_W$ as specified). [–]
C_N	Normal-force coefficient. [–]
d	Characteristic projected length on a cross-stream plane (as used in Strouhal definition). [m]
D	Drag force. [N]
f	Frequency (generic). [Hz]
f_b	Beating frequency. [Hz]
f_g, f_V	Gust frequency or vane oscillation frequency. [Hz]
f_s	Vortex-shedding frequency. [Hz]
f_θ	Primary pitch oscillation frequency. [Hz]
$f_{\theta,0}$	Natural pitch frequency in uniform flow (no gust). [Hz]
F_g	Nondimensional gust forcing level. [–]
GR	Transverse gust ratio, $\mathrm{GR} = \lvert v_{g,\max}\rvert/U_\infty$. [–]
GR_u	Steamwise gust ratio, $\mathrm{GR}_u = \lvert u_{g,\max}\rvert/U_\infty$. [–]
I	Mass moment of inertia about the pitch axis (as used in pitch-only minimal model). [kg·m^2]
I_u	Streamwise turbulence intensity, $I_u = \sigma_u/U_\infty$. [–]
I_v	Transverse turbulence intensity, $I_v = \sigma_v/U_\infty$. [–]
k	Reduced frequency, $k = \omega c_W/(2U_\infty) = \pi f_V c_W/U_\infty$. [–]

L	Lift force. [N]
M	Pitching moment (generic). [N·m]
$r(t)$	Slowly varying response amplitude in averaged (slow-flow) equations. [–]
$\mathrm{Re}, \mathrm{Re}_c$	Chord Reynolds number. [–]
Str	Strouhal number, $\mathrm{Str} = f_s d/U_\infty$. [–]
t	Dimensional time. [s]
$u(t)$	Streamwise velocity component. [m/s]
u_g, v_g	Longitudinal and transverse gust velocity perturbations. [m/s]
$\bar{u}$	Mean streamwise velocity component. [m/s]
U_∞	Freestream velocity. [m/s]
$v(t)$	Transverse velocity component. [m/s]
$v_{g,\max}$	Peak transverse gust velocity amplitude. [m/s]
x	Normalized pitch response in reduced-order models, $x = \theta/\bar{\theta}_0$. [–]

Greek symbols

α	Angle of attack (AOA). [deg or rad]
α_0	Geometric angle of attack. [deg or rad]
$\alpha_g(t)$	Gust angle (downwash-integrated gust angle). [deg or rad]
$\alpha_{g,\max}$	Maximum gust angle, $\alpha_{g,\max} = \tan^{-1}(\mathrm{GR})$. [deg or rad]
α_e	Effective angle of attack, $\alpha_e = \alpha_0 + \alpha_g$. [deg or rad]
δ	Detuning from principal parametric resonance, $\delta = \Omega - 2$. [–]
Δ	Detuning from principal externally forcing resonance, $\Delta = \Omega - 1$. [–]
ϵ	Small parameter (weak nonlinearity/forcing) in the Forced van der Pol (F-VdP) model, $\lvert\epsilon\rvert \ll 1$. [–]
ε	Stiffness-modulation amplitude in the Mathieu-type van der Pol (M-VdP) model, $\lvert\varepsilon\rvert \ll 1$. [–]
θ	Pitch angle (aeroelastic DOF). [deg or rad]
$\bar{\theta}_0$	Averaged oscillation amplitude. [deg or rad]
λ_g	Reduced gust wavelength, $\lambda_g = U_\infty/(c_W f_V) = \pi/k$. [–]
μ	Effective aeroelastic damping parameter in VdP models, $0 < \mu \ll 1$. [–]

$\tilde{\mu}$	Normalized damping parameter, $\tilde{\mu} = \mu/\omega_0$. [–]
Ω	Frequency ratio, $\Omega = \omega_g/\omega_0$. [–]
σ_u	Standard deviation (RMS) of streamwise velocity fluctuations. [m/s]
σ_v	Standard deviation (RMS) of transverse velocity fluctuations. [m/s]
τ	Nondimensional time, $\tau = \omega_0 t$. [–]
ω	Angular frequency (generic). [rad/s]
ω_0	Natural flutter frequency (no-gust condition). [rad/s]
ω_g	Gust angular frequency. [rad/s]

Subscripts and notation

$(\cdot)_\infty$	Freestream quantity.
$(\cdot)_0$	Baseline / reference / no-gust quantity.
$(\cdot)_g$	Gust-related quantity.
$(\cdot)_{\max}$	Maximum value.
$(\cdot)_V$, $(\cdot)_W$	Vane-related and wing-related quantity, respectively.
$\dot{(\cdot)}$	Derivative with respect to dimensional time t.
$(\cdot)'$	Derivative with respect to nondimensional time τ.
$\bar{(\cdot)}$	Mean or reference value (context-dependent).

Abbreviations

AOA	Angle of attack.
B–L	Beddoes–Leishman (dynamic stall model).
CF	Coupled/coalescence flutter.
CFD	Computational Fluid Dynamics.
CTA	Constant-temperature anemometer.
DOF	Degree of freedom.
LCO	Limit-cycle oscillation.
LE / TE	Leading / trailing edge.
LEV / TEV	Leading / trailing edge vortex.
LES	Large Eddy Simulation.

LG / TG	Longitudinal gust / transverse gust.
LSB	Laminar separation bubble.
LSF	Laminar separation flutter.
PIV	Particle image velocimetry.
PSD	Power spectral density.
ROM	Reduced-order model.
SAO / LAO	Small-amplitude oscillation / large-amplitude oscillation.
SF	Stall flutter.
VdP	Van der Pol.
UAM / UAV	Urban Air Mobility / Unmanned Aerial Vehicle.

Chapter 1

INTRODUCTION

1.1 Motivation

The study of aerodynamic and aeroelastic responses to externally imposed unsteady inflow remains a fundamental challenge, particularly in strongly nonlinear regimes. Classical unsteady aerodynamic theories—such as those of Theodorsen [1], Wagner [2], Küssner [3], and Sears [4]—provide a rigorous foundation for analyzing lifting surfaces under small perturbations, but they are largely built on linearization and potential-flow assumptions. Consequently, these frameworks have limited predictive capability when large-scale atmospheric disturbances and/or separated-flow physics introduce strong nonlinearity and non-stationarity, leading to complex fluid–structure coupling that departs markedly from linear theory.

Specifically, at transitional Reynolds numbers ($Re \approx 10^5$), the boundary layer and separation process can be susceptible to external perturbations, so small changes in inflow conditions may trigger excessive changes in vortex formation, reattachment, and load hysteresis. Characterizing how external flow excitation interacts with the lifting surface near or beyond stall, either stationary or oscillating, is essential for advancing a mechanistic understanding of nonlinear fluid–structure interaction in this regime, yet it remains comparatively underexplored. Accordingly, this research seeks to bridge this gap by developing a benchmark database and accompanying analyses of gust-excited nonlinear

aerodynamic and aeroelastic responses.

These scientific questions are directly relevant to Urban Air Mobility (UAM) and related small-aircraft concepts, which operate in low-altitude environments where gust encounters are frequent, and the vehicle mass and inertia are relatively small. In such settings, gust-induced changes in aerodynamic loads and aeroelastic response can affect (i) safety margins and controllability, (ii) energy consumption through increased control effort, and (iii) ride quality through vibration and acceleration. Thus, advances in mechanistic understanding and predictive modeling of gust-excited nonlinear aeroelasticity support the development of robust design envelopes and control strategies for gusty operating conditions.

1.2 Problem Statement

The primary scientific problem addressed in this thesis is the absence of a unified, mechanistic framework for describing the aerodynamic and aeroelastic response of lifting surfaces subjected to harmonic gusts as external flow excitation, particularly at transitional Reynolds numbers ($Re \approx 10^5$) and at high angles of attack (AOA). Near static stall, transverse (vertical) gusts can induce dynamic-stall-like behavior by modulating the effective angle of attack. However, it remains unclear to what extent this gust-induced dynamic stall is analogous to the classical pitch-induced dynamic stall, and how transitional boundary-layer physics and flow transition influence the onset, hysteresis, and vortex evolution associated with these gust-induced unsteady loads.

Another fundamental gap concerns the excitation type imposed by different gust components in an aeroelastic system. Transverse gusts primarily act as an external forcing input, whereas longitudinal (streamwise) gusts can introduce parametric modulation through time-varying inflow speed and dynamic pressure. A systematic experimental investigation that distinguishes these mechanisms and quantifies their respective response

regimes remains limited in the literature. Moreover, when such gust excitations interact with self-excited aeroelastic instabilities, such as stall flutter, the coupled system becomes a nonlinear oscillator subject to an imposed input. The coexistence of two competing frequencies—the intrinsic stall-flutter frequency and the gust frequency—raises the question of whether canonical nonlinear-dynamics phenomena, including frequency locking (synchronization/lock-in) and amplitude modulation (beating), arise and how they affect the stability boundary and response amplitude. Establishing high-quality experimental evidence for these regimes, together with interpretable reduced-order models (ROMs), provides a benchmark database for advancing predictive nonlinear aeroelastic theory under gust excitation.

1.3 Thesis Objectives

The overarching aim of this thesis is to develop a mechanistic understanding of how flow disturbances, as idealized by harmonic gusts in this thesis, influence aerodynamic loads and aeroelastic performance and stability of lifting surfaces at transitional Reynolds numbers ($Re_c \approx 10^5$) and large AOAs. To achieve this aim, the thesis pursues the following objectives:

1. **Aerodynamic characterization under transverse gusts:** Quantify the unsteady aerodynamic response of a stationary NACA0012 wing subjected to controlled transverse (vertical) harmonic gusts across pre- and post-stall conditions, identify gust-induced dynamic stall, and establish analysis metrics that enable comparison with canonical pitch-induced dynamic stall.

2. **High-fidelity flow-physics support:** Use computational fluid dynamics (CFD) to interpret the measured unsteady loads and to isolate the effects of the imposed gust components, thereby providing evidence of flow structures to support the experimental trends.

3. **Externally forced aeroelastic response (transverse gusts):** Determine how harmonic transverse gust forcing interacts with self-excited one-degree-of-freedom (one-DOF) pitch stall-flutter oscillations by mapping the response.

4. **Parametric versus external excitation (longitudinal gusts):** Examine the one-DOF stall-flutter response under harmonic longitudinal (streamwise) gusts.

5. **Reduced-order interpretation and predictability:** Develop and assess minimal phenomenological ROMs capable of representing the dominant nonlinear response features observed in the experiments.

1.4 Main Contributions

This thesis delivers new experimental evidence, flow-physics interpretation, and validated low-order modeling for gust–airfoil coupling at $Re_c \approx 10^5$, with emphasis on the distinct roles of harmonic transverse/longitudinal gusts. The main contributions are:

- **Demonstration of gust-induced dynamic stall in harmonic transverse gusts:** The thesis documents a transition from linear-like pre-stall behavior to a deep post-stall regime with strong nonlinear load characteristics indicating gust-induced dynamic stall.

- **A unified kinematic interpretation via an effective angle of attack:** An effective-angle-of-attack framework for the gusty configuration is established, providing a clear physical bridge between gust-induced dynamic stall (upwash/downwash) and pitch-induced dynamic stall (upstroke/downstroke), and enabling qualitative regime comparison using common metrics.

- **Simulation-backed flow-physics clarification for unsteady load features:** High-fidelity simulations reveal that fully three-dimensional (3D) simulations are

required to capture specific secondary load-loop features, which are linked to vortex evolution and delayed shedding processes.

- **Identification of synchronization structure in transverse-gust-forced stall flutter:** A finite 1:1 lock-in (synchronization) band is observed in the one-DOF stall-flutter system under transverse gusts, while outside lock-in the response exhibits quasi-periodic beating accompanied by well-defined spectral sidebands.

- **Quantification of gust-driven stability-margin reduction:** The thesis reveals that transverse gust forcing can advance stall-flutter onset by producing a resonance-centered wedge-like trend in critical conditions, indicating substantially reduced stability margins in unsteady inflow.

- **Evidence for parametric excitation under longitudinal gusts:** In contrast to transverse gusts, longitudinal gusts are shown to produce a response consistent with parametric modulation, including a dominant 2:1 parametric lock-in band and a distinct spectral signature compared against direct forcing.

- **Validated minimal models for both excitation classes:** Two reduced-order models are developed and validated against experiments: a forced van der Pol oscillator capturing externally forced lock-in and modulation under transverse gusts, and a Mathieu-type van der Pol oscillator capturing parametric synchronization and sideband structure under longitudinal gusts.

1.5 Scope and Limitations

This research is conducted experimentally in a low-speed wind tunnel at Reynolds numbers of approximately 10^5. The gusting flowfield is generated using two upstream motor-driven vanes, limiting the scope to continuous, harmonic gusts rather than discrete gusts (such as sharp-edged or 1-cosine types) or random turbulence. The harmonic flow excitation is

characterized by its amplitude, frequency, and wavelength, with measurements acquired using Constant Temperature Anemometry. The study focuses on two rigid test wings: one stationary wing with an internal balance and the other mounted on an elastic support (one-DOF pitch). The former is used to investigate the aerodynamic response to transverse gusts; the latter is utilized to study the aeroelastic response to transverse and longitudinal gusts. Both wings have a NACA0012 profile, whose aerodynamic characteristics can be accessed from rich literature sources, installed with two end plates suppressing 3D tip effects.

1.6 Thesis Organization

This thesis is organized into eight chapters, structured as follows:

- **Chapter 1: Introduction.** This chapter outlines the motivation for the study, defines the scientific gap in the field, and clearly states the core research questions, objectives, and contributions.
- **Chapter 2: Background and Objective.** This chapter highlights previous attempts to study aerodynamic responses to external disturbances, reviews dynamic stall physics, and discusses nonlinear dynamics in the context of aeroelastic instability.
- **Chapter 3: Methodology.** This chapter outlines the experimental methodology, including the gust generator design, the constant-temperature anemometer with an X-hot-wire probe, the custom stationary wing developed for aerodynamic tests, the aeroelastic wing and mounting used for gust-driven stall-flutter experiments, and the instrumentation and data-acquisition procedures.
- **Chapter 4: Gusting Flow Survey.** This chapter demonstrates the flow survey for both transverse and longitudinal gusts in an empty test section, before mounting

test wings.

- **Chapter 5: Dynamic Stall Induced by Transverse Gusts.** This chapter presents and discusses the fundamental aerodynamic characteristics of the stationary wing subjected to transverse gusts, with a focus on gust-induced dynamic stall.

- **Chapter 6: Stall Flutter Under Transverse Gusts.** This chapter explores the aeroelastic response of a one-DOF pitching wing in stall flutter subjected to transverse gusts, examining gust-forced lock-in and synchronization phenomena through the external forcing mechanism.

- **Chapter 7: Stall Flutter Under Longitudinal Gusts.** This chapter illustrates the stall-flutter response excited by longitudinal gusts, highlighting the effects of parametric excitation and spectral sidebands, and providing a clear, side-by-side comparison with the response under transverse gusts.

- **Chapter 8: Conclusion.** The final chapter summarizes the scientific contributions of this research.

Chapter 2

BACKGROUND AND OBJECTIVE

2.1 Gust Generation Method

Firstly, a general definition of commonly-used terminology, *gusts*, should be provided. Corkery [5] defined a gust as "a flow velocity perturbation, relative to a quiescent fluid, which is caused by some mechanism external to a body of interest". He further noted that any gust is associated with free vorticity in the flow created externally to the body of interest. This definition is particularly natural for water-towing-tank configurations, where the undisturbed fluid is essentially quiescent. In wind tunnel experiments, however, gusts are typically superimposed on a steady mean flow; thus, a gust is more practically interpreted as a velocity perturbation relative to that mean flow rather than relative to a strictly quiescent fluid. Fig. 2.1 shows three types of idealized gusts, transverse, longitudinal, and vortical, encountered by an airfoil/wing. In Fig. 2.1(a), a continuous harmonic transverse/vertical gust is superposed onto a uniform freestream and encountered by an airfoil. Transverse gust responses are commonly investigated [6], [7], [8], [9], using analytical, experimental, numerical approaches, or a combination thereof. Longitudinal gusts shown in Fig. 2.1(b), i.e. flow variations in the streamwise direction, have also been investigated [10], [11], [12], but not to the same extent as transverse gusts. Vortical gust encounter, as shown in Fig. 2.1(c), is of importance in studies of modern air vehicle flights [13] as well. Vortical gust response was intensively studied by Barnes

and Visbal employing numerical simulations [14], [15]. The velocity field of a vortical gust isn't uniform; it varies depending on how far from the vortex core. To mitigate the undesired effects of gusts on flying vehicles, some control strategies have been proposed from multiple perspectives, such as the analytical model development [16], experimental [17], [18], and numerical [19] investigations.

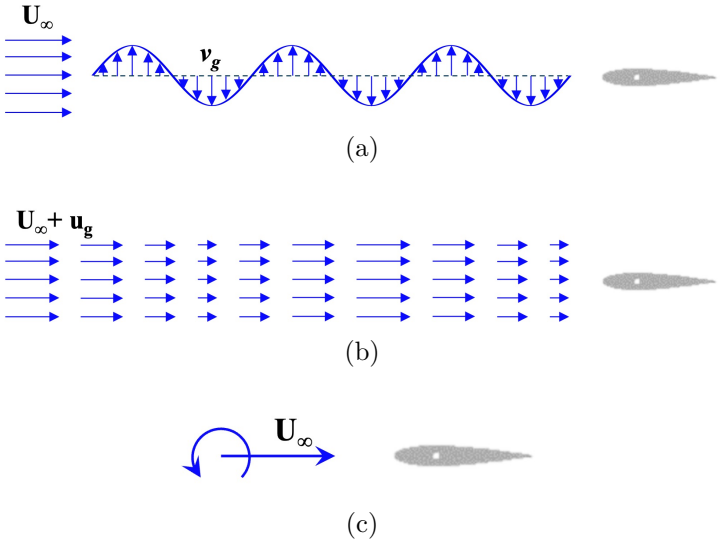

Figure 2.1: Schematic of (a) harmonic transverse gust and (b) longitudinal gust, and (c) vortical gust, traveling with freestream U_∞.

To investigate the aerodynamic and aeroelastic response of wings to gusts (i.e., externally imposed flow excitation) experimentally, a reliable capability for generating controlled gusts is essential. In practice, two approaches are most common: (i) a stationary model subjected to a prescribed unsteady gusting inflow, as typically implemented in wind/water tunnels, and (ii) a translating model moving through a spatially varying gust field, as commonly realized in water-towing-tank experiments. Each approach offers distinct advantages and limitations, which are discussed as follows.

2.1.1 Stationary model with incoming oscillating flow

One of the primary approaches to investigating the effects of gusts on structures involves oscillating the flow at a stationary model, which is a commonly used technique in wind

tunnel facilities [20], [21], [22], [23], [24], [25], [26], [27]. In Refs. [21], [22], [23], [24], [25], [26], oscillating upstream vanes were employed to turn the incoming airflow, while the number of vanes could differ. Two oscillating vanes were used in Refs. [22], [24], [25], which may be the most commonly seen. Moreover, one, four and six vanes were used in Refs. [21], [23], [26], respectively. There are also some other techniques to oscillate the flow. Tang *et al.* [20] utilized four stationary vanes and four rotating slotted cylinders located at their trailing edges (TEs). By adjusting the rotating parameters, different profiles of gust were obtained. Due to the blunt structure of cylinders and their interaction with the wake flow of vanes, the turbulence level of their test section might be significantly increased. Olson *et al.* [27] developed a novel approach for generating transverse gusts in wind tunnels without significantly increasing turbulence levels in the test section. This approach utilized a vortex-generator array (VGA) composed of small NACA0012 airfoils mounted on a test-section wall. By dynamically varying the vanes' angles of attack via a centralized motor, the system produced controllable tip vortices whose induced velocity field formed a nominally uniform transverse gust in the core flow. The resulting sinusoidal and step-like gusts demonstrated high uniformity in the central test region. However, there were limitations in the strength of the tip vortices, which prevented the amplitude of the gusts from reaching the desired high values.

Overall, the gust generation method by oscillating the flow for a stationary model in wind tunnels offers several advantages over other experimental methods, such as the ability to generate a wide range of gust profiles with varying amplitudes and frequencies, as well as providing precise control over the testing environment. Additionally, the use of a stationary model can facilitate the testing of larger structures, provided that the wind tunnel's test section is adequately sized. By using a stationary model, researchers can isolate the aerodynamic effects of gusts and study their impact on the airfoil's response, without interference from the structure's own elastic response. This is particularly useful for developing a better understanding of the complex aerodynamic-elastic interactions

that can occur in real-world scenarios, such as aircraft encountering turbulence.

This method is also preferred when planning aeroelastic studies, which involve the analysis of the interactions between aerodynamic, elastic, and dynamic forces acting on a structure. Overall, the oscillation of the flow is a valuable experimental technique for investigating the effects of gusts on structures. Its precise control and versatility make it a popular choice for researchers studying the aerodynamic and aeroelastic behavior of structures in a variety of applications, including aircraft, wind turbines, skyscrapers, and bridges.

2.1.2 Translating model in steady flow

The common approach involves creating a desired flow field for a translating model, which is commonly used in towing tanks [6], [7], [28]. This method involves creating a flow field that simulates the conditions that a moving structure would experience in the real world. By translating the model through this flow field, researchers can study the response of the structure to sudden and discrete gusts. The experimental rig of Perrotta and Jones (2017) [28] generated a "sine-squared" gust, which has a similar gust shape with more commonly-used 1-cosine gusts. Similarly, Corkery *et al.* (2018) [6] developed a "top-hat" gust. The main advantage of this method is that it can take advantage of Reynolds number scaling effects, as water is often used as the working fluid. In addition, the transverse gust ratio (i.e., the transverse velocity component normalized by the freestream velocity) can, in principle, be made arbitrarily large. However, this method requires more complex experimental setups and may be more challenging to control. In addition, it is difficult to change the type of discrete gust profile once the setup is fixed. It is also challenging to implement in a wind tunnel, considering a faster response in time.

2.1.3 Comparison of two methods

Granlund *et al.* (2014) [29] investigated the airfoil response in separated and attached flows to longitudinal gusts in both wind and water tunnels. They compared the results from the two configurations, i.e. the stationary model with incoming oscillating flow for the wind tunnel and the moving model in steady uniform flow for the water tunnel. To isolate the circulatory contribution of the streamwise oscillation or gust, researchers subtracted the apparent-mass contributions arising from the flow acceleration from the total measured force. The residual force component (lift and drag) obtained from this subtraction was found to represent the circulatory contribution of the gust. This approach was employed for both nominally attached flow and separated flow conditions, and a high degree of agreement was reached between wind and water tunnel experiments. Therefore, it can be concluded that aerodynamic gust response measurements can be conducted with static test articles in oscillating freestream facilities.

Considering the final research interest lies in investigating both the aerodynamic and aeroelastic response to gusts, a capability of generating controllable perturbed flow (transverse or longitudinal gusts) using motor-driven pitching vanes was developed for a low-speed wind tunnel of the RMC. The selection of the vane number, the airfoil profile, the chord length and other configurations will be discussed and determined in Chapter 3.

2.2 Unsteady Aerodynamic Response to External Disturbances

2.2.1 Analytical unsteady aerodynamics

Küssner's function describes the linear lift response of an airfoil to a spatially varying gust [3], [30]. The function provides a direct analytical solution for sharp-edged transverse

gusts. Küssner's formulation can be directly applied to continuous turbulence by making use of the superposition principle in the form of Duhamel's integral. A similar operation could be found with Wagner's function for the unsteady linear lift due to arbitrary motion, which was originally developed for step-change airfoil motions [2], [31]. At a constant streamwise velocity, Wagner's function numerically models the lift generated from an abruptly pitching wing by considering the diminishing influence of the starting shedding vortex due to motion.

Correspondingly, there are two unsteady aerodynamics theories predicting analytic solutions for small-amplitude sinusoidal transverse gusts and sinusoidal motions in pitch and heave, which are the Sears function [4] and the Theodorsen function [1], respectively. The former problem was initially introduced by von Kármán and Sears (1938) [32] and further elaborated by Sears (1941) [4]. The aerodynamic forces prediction for an airfoil encountering simple harmonic gusts was derived from the Theodorsen problem. The Theodorsen problem was stated from the point of view of a flat plate undergoing simple harmonic motion in pitching and heaving. Small perturbations and a flat wake behind the airfoil extending to infinity were assumed. By integrating the vortex sheet from the trailing edge to infinity, a solution in the form of Bessel functions was obtained, which showed that the lift due to circulation was a function of the reduced frequency, $k = \frac{\omega b}{U_\infty}$, where ω is the flow/motion variation frequency; b is the half chord length; U_∞ is the freestream velocity. Sears and Theodorsen functions are related to Küssner's and Wagner's functions via the Fourier transform, respectively [33].

In both Sears and Theodorsen problems, the reduced frequency, k, is an important parameter for aerodynamic prediction. Fig. 2.2 shows a vector diagram comparing the Sears function and Theodorsen function as variations of reduced frequency. From the diagram, it is seen that Theodorsen and Sears functions are very similar for a small reduced frequency [34]. This point of view can be more clearly understood from Fig. 2.3. The dimensionless wavelength of a gust is defined as the ratio of the gust travel length of one

period divided by the wing chord, $\lambda_g = \frac{2\pi U_\infty}{\omega c} = \frac{\pi}{k}$. Thus, the gust wavelength and reduced frequency are inversely constrained. With a smaller reduced frequency of gust, spatially- and temporally-varied gusts can be treated as temporally-varied but spatially uniform, resulting in similar aerodynamic behavior with the simple harmonic heaving wing. Otherwise, spatial variation across the chord becomes non-negligible: the transverse-gust–induced upwash/downwash changes appreciably from leading to trailing edge, and the aerodynamic response can differ substantially from that of a spatially uniform heaving configuration.

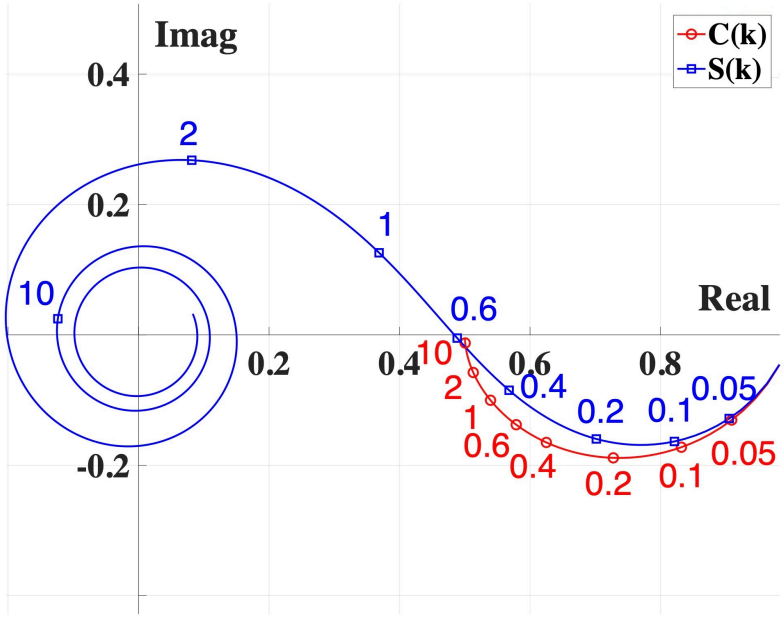

Figure 2.2: Vector diagram showing imaginary part versus real part of the Theodorsen function $C(k)$ and Sears function $S(k)$ with a reference point for gust data taken at the leading edge; representative k is depicted by the digits.

Beyond the classical treatment of transverse gusts, the unsteady response to longitudinal gusts, often idealized as a temporally varying freestream speed: $U(t) = U_\infty + u_{g,max}\sin(\omega_g t)$, was classically treated by Isaacs and Greenberg. Isaacs (1945) [35] derived an "exact" analytical solution for an airfoil at fixed angle of attack in a harmonically varying freestream; however, the solution is commonly written as nested Fourier-series summations involving repeated evaluation of Bessel functions, which can impose substan-

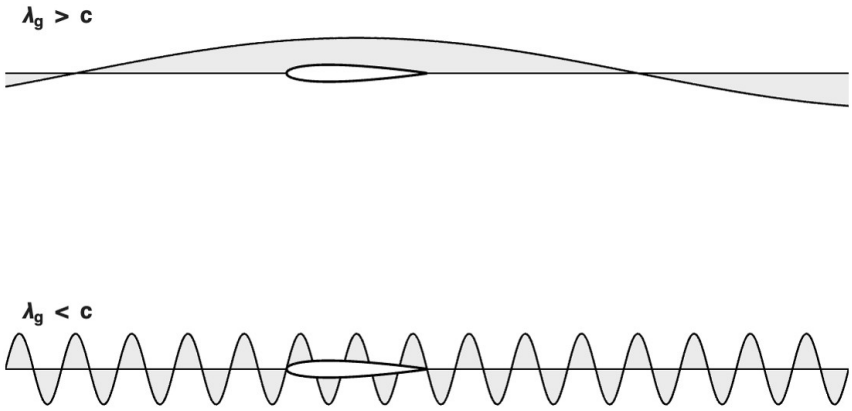

Figure 2.3: Effect of the gust wavelength related to the wing chord, redrawn based on Ref. [34].

tial computational effort in practical use. Greenberg (1947) [36] subsequently generalized Theodorsen's unsteady framework to accommodate an airfoil undergoing simultaneous small-amplitude kinematics (pitch and heave) within a pulsating stream characterized by longitudinal gusts, incorporating the assumption of sinusoidal wake vorticity. While Greenberg's theory has demonstrated superior predictive capability for lift history in pre-stall regimes—where flow remains attached—it typically deviates from experimental results at larger angles of attack or high gust amplitudes (the fluctuation exceeds 40% of the mean velocity [37]). Recent research, such as Wang *et al.* (2024) [38], suggested that the applicability of Greenberg's framework can be extended into post-stall regimes through quasi-steady refinements that account for real-world viscous effects and flow separation.

All preceding classical models are useful tools for predicting the behavior of airfoils in unsteady aerodynamics, but they have limitations and may not always accurately represent real-world scenarios. First, all four models assume thin-airfoil (flat plate) theory, which simplifies the problem by ignoring the geometry of wings. Secondly, on some level, they all rely on small perturbations for the derivation of their respective theories, which may break down for many realistic applications. Finally, these linear models describe the effect of a kinematic or flow field disturbance on bound circulation. When the flow is not attached and associated with large scales of separation, the aerodynamic forces

predicted by these analytical methods may not be reliable. Therefore, to understand unsteady aerodynamics with challenging configurations, experimental and high-fidelity computational studies are needed.

2.2.2 Experimental studies

Babinsky's group at the University of Cambridge has conducted extensive experimental research into the topics of gust encountering and pitching wing over recent years, combining experimental data with analytical developments in nonlinear unsteady aerodynamics. In Refs. [6], [39], a top-hat gust generation capability was developed for a water towing tank, and gust encountering response of a flat-plate wing with zero AOA was studied. Similarly, Stevens et al. [40], [41] investigated a translating flat-plate wing pitching from 0° to 45° at varying rates. For both research objectives, the group utilized a combination of dye flow visualization, particle image velocimetry (PIV), and force balance measurements.

To investigate the response of an airfoil entering a spatially varying gust, Corkery et al. [6] utilized a gust rig to generate a region with a high gust ratio (GR) and a two-chord width. To identify dominant flow topological differences between the conditions experienced by unmanned aerial vehicles (UAVs) in flight and the assumptions of the Küssner model, an extreme GR of 1 was chosen at Re (chord Reynolds number) = 40,000. Surprisingly, the lift coefficient predicted using the Küssner model fit measurements well during entry into the gust region. When the leading edge was approaching the exit edge of the gust region, significant discrepancies arose. In addition, the measured lift coefficient reached a steady state much sooner than the prediction by Küssner model. Using the same setup, Corkery *et al.* (2019a) [39] found an added mass (gust flow) attributed force when the plate traveled at a constant velocity through the transverse gust. According to Ref. [32], this force arose because of the formation of an attached non-circulatory distribution of vorticity to satisfy the no-penetration condition conventionally due to flow

body acceleration. A similar appearance was observed when the plate was fully submerged in the gust. Thus, it was argued that the observed added mass force was induced by the vorticity field in the gust region. To further study the added mass effects, Corkery *et al.* (2019b) [42] isolated the added-mass vorticity using PIV methodology with a translating and rotating flat plate. They provided the experimental evidence coupling added mass and the production of boundary layer vorticity, as well as confirmed that inviscid unsteady flow theory describes the added-mass effect correctly even in well-developed viscous flows.

Regarding abrupt wing motions, Stevens *et al.* (2013) [40] investigated a translating wing pitching about the mid-chord from zero to 45° at Re = 10,000. Their results indicated that the development of the suction surface flow and the leading edge vortex (LEV) was strongly correlated with the kinematics of the leading edge (LE), suggesting that the effective local angle of incidence (taken at LE) is of considerable significance in unsteady pitching motions. To remove the leading edge kinematics, the wing was pitched about the LE in Ref. [41], and the unsteady aerodynamic forces at two different pitch rates were analyzed and compared. The forces were enhanced with a fast pitch rate due to a large virtual mass contribution, especially for the lift. While with a slow pitch rate, the forces were dominantly distributed by the circulatory effects as expected. For both scenarios, steady-state conditions can be reached after 15 convective times ($t^* = \frac{U_\infty t}{c}$) since the start of the pitch motion. It was also found that the streamline re-attachment is an indication of higher lift coefficients, which might be owing to the maximal circulatory force contribution when the streamline bends towards the trailing edge.

Similar to the Cambridge studies, Perrotta and Jones (2017) [28] developed a gust rig at the University of Maryland capable of generating sine-squared (1-cosine) gust profiles. They investigated gusts with a maximum GR of 1.68 at $Re = 20,000$, and observed that at high GR combined with a large geometric AOA (45°), the Küssner model became unreliable, with a gust recovery time extending to approximately 35 convective times. Using the same facility, Biler *et al.* (2019) [7] studied a translating flat plate at $Re \approx$

40,000 across various AOAs (0° to 45°) and lower gust ratios ($GR \leq 0.32$). Their results indicated that increasing GR consistently elevated maximum lift and drag. However, while increasing the geometric AOA up to 15° enhanced lift, increases beyond this threshold resulted in a lift decrease, likely due to massive flow separation and the shedding of the LEV. In particular, both research groups used numerical simulations to support the experimental interpretation, which will not be covered here, to align with the experimental focus of this study.

2.3 Dynamic Stall

Transverse gusts can alter the effective angle of attack (AOA), which can induce dynamic stall. Dynamic stall is a highly nonlinear aerodynamic phenomenon characterized by enhanced lift and related hysteresis effects in both lift and moment due to the wing in and out of the static stall. It has been intensively studied in the past decades employing pitching wings, by experimental methods [43], [44], [45], [46], [47] and numerical simulations [48], [49].

2.3.1 Experimental research on pitch-induced dynamic stall

The hysteresis effects on an oscillating wing have been comprehensively studied. In the beginning, it had been commonly believed or assumed that the dynamic stall originated from the bursting of a laminar separation bubble near the leading edge and resulted in strong vortex shedding passing through the upper surface to the trailing edge. McCroskey *et al.* (1976) [43] identified a limitation in the assumption by conducting experiments that involved applying boundary-layer trips. This approach facilitated transition ahead of laminar separation, effectively eliminating the leading-edge bubble and highlighting the deficiency of the assumption. They created and observed three types of dynamic stall by modifying the leading edges of the geometry of standard NACA0012 wings. The three

dynamic stall types include: 1) trailing-edge stall developing from a relatively gradual progression of boundary-layer flow reversal and separation, from the trailing edge toward the leading edge; 2) leading-edge stall caused by an abrupt breakdown of the turbulent flow on the forward portion of the airfoil, following an initial progression of flow reversal from the trailing edge; and 3) another form of leading-edge stall due to the abrupt bursting of a leading-edge laminar separation bubble. By applying oil and smoke visualization, hot-wire flow reversal, surface-mounted pressure transducer, and its integrated instantaneous force and moment, all three types of dynamic stall were well characterized. They found that, for most cases, the stall process was induced by a breakdown of the turbulent boundary layer, and leading-edge bubble bursting is much more of a special case. In addition, the reduced frequency had significant effects on both the force/moment results and boundary-layer separation. Even with partial-stall cases, i.e. trailing edge stall, the force/moment results against incidence angle performed noticeable hysteresis.

In the same research group, McCroskey (1981) [45] focused more on the analysis of stall events of aerodynamic force behaviors, including lift, drag and aerodynamic moment. It should be noted that the hysteresis in the aerodynamic moment with increasing and decreasing incidence led to negative or positive aerodynamic damping, which was the key factor in aeroelastic instability. The effects of various parameters on the dynamic stall behavior were studied in this research, including airfoil geometry, reduced frequency, pitching amplitude and mean angle, Mach number, and various types of motion. Analytically modeling light and deep stall regimes with a few empirical correction techniques was proposed for engineering purposes, although all of them had limitations.

Carr (1988) [46] emphasized the roles of compressibility, Reynolds-number dependence, and three-dimensional effects on dynamic-stall loads, motivated in part by wind-turbine applications for electric power generation. That review also summarized several stall-control concepts aimed at alleviating, delaying, or suppressing dynamic stall by weakening or eliminating the associated leading-edge vortex. Carr and Chandrasekhara (1996) [47]

conducted a detailed review of research regarding compressibility on the dynamic stall. They concluded that compressibility can fundamentally alter the stall process relative to low-Mach-number conditions, implying that stall-control strategies developed at low speeds may not transfer directly and should be revisited in light of compressible stall physics. Some significant findings of their research are noteworthy for the current research, such as the freestream Mach number (M_∞) of 0.2 with the oscillating airfoil (instead of the commonly-believed $M_\infty \approx 0.3$ for steady scenarios) being the critical speed to take compressibility effects into account. They reported local supersonic flow was observed for this critical Mach number (0.2) in Fig. 3 of [47]. In addition, the overshooting of dynamic lift at incompressible flow speeds was significantly decreased by the compressibility effects.

2.3.2 Numerical simulations on pitch-induced dynamic stall

With the surging development of computing capabilities in recent years, more numerical simulation studies on dynamic stall and stall control were conducted. Using URANS simulations, Wu *et al.* (1998) [50] investigated post-stall flow control by applying periodic surface blowing-suction. The leading-edge shear layer and vortex shedding were two key control subjects to alleviate the stall effects. In the post-stall regime, the original massively separated and disordered flow evolved to much more organized flow patterns with resonance to the local forcing. Consequently, a stronger lifting vortex was formed to enhance the lift effects. This research may contribute to the stall control strategy using periodic external excitation in the present research.

Benton and Visbal (2019) [49] investigated the onset mechanism of dynamic stall at a relatively high transitional Reynolds number ($\sim 10^6$). Large-eddy simulations (LES) were conducted to investigate the ramp-type pitching NACA0012 airfoil. The development of LSB near the leading edge was the first stage. Following the breakdown of the LSB, turbulent separation occupied more than 95% of the upper surface. The generation and merging of a leading-edge vortex and turbulent separation vortex originating from

the trailing edge were displayed using instantaneous contours of entropy. Their final interaction formed an intensive dynamic stall vortex. This computational research provided a vivid demonstration of the dynamic stall process in Ref. [43]. Most recently, Miotto *et al.* (2022) [51] numerically studied the onset and evolution of a on a periodic plunging airfoil. This type of dynamic stall was marked by two major flow features: a train of Kelvin-Helmholtz instabilities and a breakdown of vortical structures along a shear layer formed at the leading edge. It is noteworthy from their research that the plunging motion may also induce dynamic stall effects.

2.4 Semi-Empirical Dynamic Stall Modeling

Beyond high-fidelity experiments and CFD, dynamic stall loads are frequently represented using semi-empirical engineering models. Among these, the Beddoes–Leishman (B–L) model remains the most widely adopted framework in rotorcraft and wind-energy applications [52]. The model decomposes the unsteady aerodynamic response into distinct contributions from attached-flow unsteadiness, trailing-edge separation development, and leading-edge vortex evolution, with parameters typically calibrated from canonical pitching-airfoil measurements. While computationally efficient, the original B–L formulation was primarily optimized for high-speed, high-Reynolds-number environments, leading to predictive discrepancies in the transitional regimes common to modern small-scale wind turbines and unmanned aerial vehicles.

Recent refinements have focused on adapting the B–L framework for lower Reynolds numbers and improving its integration into complex aeroelastic solvers. Boutet *et al.* (2020) [53] proposed significant modifications to the stall-onset criteria and vortex-shedding time constants to better capture the physics of low-speed dynamic stall, specifically validating these enhancements on the NACA0012 profile. Furthermore, the transition toward state-space representations, such as the IAG model evaluated by Bangga *et al.* (2023) [54],

has improved the model's ability to predict deep stall characteristics and its robustness in coupled aeroelastic stability analyses.

Most recently, the field has moved toward data-knowledge fusion methods to overcome the generalization limits of purely empirical frameworks. Shi *et al.* (2025) [55] introduced a hybrid Data-Knowledge-Driven (DKD) approach that integrates the state-space Beddoes–Leishman model with deep neural networks. By using the B–L model to provide a physical baseline, the neural network is able to more accurately map the nonlinear residuals associated with leading-edge vortex dynamics and trailing-edge separation across diverse Reynolds numbers and motion profiles. Specifically validated on the NACA0012 airfoil, this physics-informed machine learning approach effectively bridges the gap between computationally efficient semi-empirical modeling and high-fidelity numerical data.

2.4.1 Gust-induced dynamic stall

Based on the literature review, airfoils pitching in and out of stall regimes were extensively studied. However, oscillatory flows, like transverse gusts, can also induce dynamic stall, which has been less explored. The transverse gust response of a NACA0012 wing in a water tunnel at a lower transitional Reynolds number was experimentally studied [38], [56], but the main focus was on the lift behavior and the aerodynamic moment behavior was not discussed. The aerodynamic moment behavior during dynamic stall is crucial, especially for analyzing the similarity between pitch- and gust-induced dynamic stalls. In addition, the gust amplitude, which is an inflow angle amplitude induced by gusts of around 3° in Refs. [38], [56], was relatively small. Hence, it is of interest to investigate the gust response with larger amplitudes and conduct a cross-comparison between the gust-induced and pitch-induced dynamic stalls. Dos Santos *et al.* (2021) [57] presented an augmentation of the semi-empirical B–L dynamic stall model to include stochastic gust loads. The dynamic stall model was coupled with a classic two-DOF aeroelastic system to

characterize the stability boundary. It was found that the gusts could induce stall flutter, which highly depended on the gust intensity. Stall flutter is a self-sustained aeroelastic instability, which is discussed in the following section.

2.5 Aeroelastic Instability

The interaction between an elastic structure and an unsteady flow field gives rise to the complex domain of aeroelasticity. A defining characteristic of aeroelastic systems is their capacity for self-excited oscillations, which can manifest even in a uniform freestream without external forcing. To provide a rigorous foundation for investigating the aeroelastic response to gusts, it is essential to first characterize the fundamental dynamic instabilities prevalent in aeroelastic structures.

Flutter is a dynamic instability characterized by self-sustained vibrations resulting from the coupling between a structure's elastic deformation and the surrounding aerodynamic loads, which can lead to catastrophic structural failure [31]. In the context of lifting surfaces, these instabilities are generally classified into two distinct categories: classical coupled/coalescence flutter (CF) and stall flutter (SF). While CF involves the merging of aeroelastic modes, SF is a nonlinear phenomenon driven by flow separation.

2.5.1 Studies on large amplitude oscillation

The essential feature of coupled flutter is the coupling between two DOFs, often bending and torsion. It is also called classical flutter, coalescence flutter, binary flutter, two-DOF flutter, and two-mode flutter. The motion of the two DOFs couples in such a way that there is a net positive transfer of energy from the airflow to the oscillating structure. As the airspeed approaches the critical speed, the so-called flutter speed, the frequencies of two DOFs start to converge gradually but do not necessarily coalesce at the flutter condition [34].

Stall flutter occurs when an airfoil stalls due to high AOAs, and the resulting flow separation causes the wing to vibrate in a flutter-like manner. Stall flutter is induced due to dynamic stall effects illustrated in Fig. 2.4. The loops represent the aerodynamic loading due to a periodic motion of the airfoil about an initial AOA. The marked "$+W$" and "$-W$" are the net work done by the airflow, featuring clockwise and counterclockwise directions, respectively. Positive total work denotes energy transfer to the oscillating motion. Contrary to the classical flutter, which needs two DOFs to occur in attached flow conditions, stall flutter can happen with motion in one DOF only. It requires a separate flow and leads to negative aerodynamic damping due to dynamic stall effects. Although in practice both bending and torsion motions are present during stall flutter, the mechanism can be analyzed separately. The vibration of the wing due to stall flutter can excite flutter in other parts of the aircraft's structure, leading to a cascade of vibrations that can quickly escalate into a catastrophic failure.

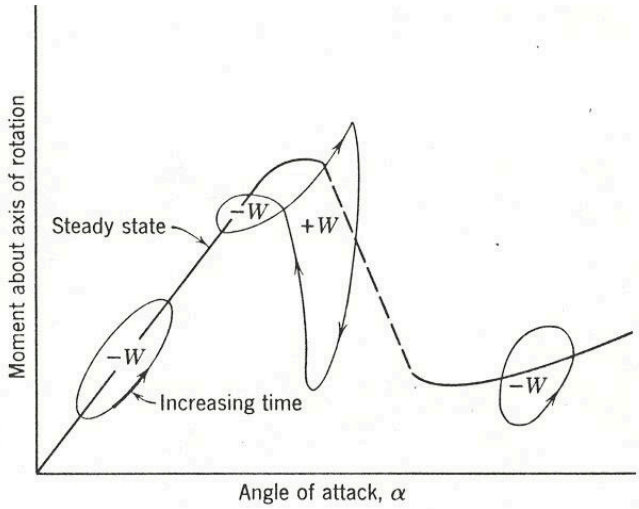

Figure 2.4: Demonstration of aerodynamic hysteresis, adopted from NACA report by Halfman, Johnson, and Hayley [58] (public domain).

Large amplitude oscillations (LAOs) were observed in Ref. [59] by the researchers in our lab. The LAOs originated from a two-DOF, coalescence-type flutter instability, as predicted by inviscid unsteady thin-airfoil theory. But note that the analytical theory could only predict the occurrence of flutter and its flutter airspeed, not the amplitude

of the oscillation. Even for the same flow conditions, different initial conditions would induce different types of flutter, which suggested the effects of nonlinear aerodynamics, especially for the aerodynamic moments. It could be analogized to the mechanism of "basin of attraction". These multiple attractors were also reported in Ref. [60] from the same group, but the elastic rotation axis, or EA, was shifted from 27% to 35% of the chord length from the LE. By analyzing the aeroelastic response, the measured results from the latter configuration were more prone to stall flutter and associated limit cycle oscillations (LCOs). In addition to LAOs, small amplitude oscillations (SAOs) and a nonzero equilibrium were also observed for the same flow conditions by applying different initial perturbations of the wing deflection. The mechanism of SAOs will be discussed in the next section. A frequency lock-in mechanism was observed by analyzing the dominant frequencies of LCOs [61]. The frequency ratio of two DOFs has a significant effect on the mechanism. It also has a significant impact on the amplitude and LCO frequency of heave, whereas the pitch response is not greatly influenced by the frequency ratio.

2.5.2 Studies on small amplitude oscillation

For a lifting body, nonlinear aerodynamic effects can manifest even at low angles of attack (AOA) well below the static stall threshold. In Refs. [62], [63], laminar separation bubbles (LSBs) were reported from 2° to 6° for a NACA0012 cantilever wing at a transitional Reynolds number (in the order of 10^4). Lutz *et al.* also reported LSB effects in the lift coefficient using NACA0009 airfoil at Re = 50,000 [64]. Due to the instability of the bubbles, the nonlinear aerodynamics may rise, and the aerodynamic moments can trigger instability in an aeroelastic system. Poirel *et al.* (2008) [65] observed self-sustained SAOs with a rigid NACA0012 wing moving only in rotation (pitch) in the RMC's closed-loop wind tunnel. These instability phenomena were attributed to the behavior of laminar separation. Induced by positive energy exacted from the airflow, the resulting aeroelastic LCO is physically related to the trailing-edge laminar separation with negative aerody-

namic damping. While the characteristics of this LCO are reminiscent of stall flutter, it occurs at small, pre-stall angles and exhibits a strong dependency on the Reynolds number, specifically within the transitional regime. To distinguish it from stall flutter, it was named *laminar separation flutter* (LSF). Both SF and LSF represent nonlinear phenomena characterized by negative aerodynamic damping.

Poirel and Yuan (2010) further confirmed the conclusion by analyzing the aerodynamic moments measured from the experiments [66]. From the spectral plots of both pitch response and aerodynamic moments, super-harmonic components were obtained, despite the dominance of simple harmonic frequency. To further understand the mechanism, 3D LES simulations were conducted with a prescribed simple harmonic motion which had the same amplitude and simple harmonic frequency as the SAOs observed in the experiments. The unstable laminar separation of flow, laminar–turbulent transition, and re-attachment were captured. From the predicted aerodynamic moment coefficient, the odd super-harmonic content was also confirmed, despite simple harmonic motion as input. The nearly equal positive work done by the flow to the structure was confirmed in both numerical simulations and experiments.

By releasing the translation DOF (heave) in their experimental rig, two-DOF in pitch-heave SAOs were observed [59]. Since the instability mechanism was still owing to the laminar separation bubbles when pitching, the behaviors of SAO flutter, including the oscillation frequency, amplitude, and critical number range, were not affected significantly by the heave. To improve the simulation methods in Ref. [66], Yuan *et al.* (2013) [67] developed their in-house CFD code INSflow with an implemented two-DOF structural model. Compared to the traditional analytical aeroelastic equations, the aerodynamic inputs were obtained from the high-fidelity CFD results, which were updated based on the aeroelastic response. The computed results were well validated by the experimental results. The numerical results also confirmed that the added heave DOF did not have many effects on this type of flutter. Thus, it was concluded that the laminar separation

flutter is a pitch-driven phenomenon. To study the effects of freestream turbulence on this negative aerodynamic-damping type instability, 2D URANS simulations with $\gamma - Re_{\theta t}$ model were conducted [68], considering the 3D LES simulations were too expensive, using the correlation-based transition model, $\gamma - Re_{\theta t}$ developed in Ref. [69], which is proved to be good in predicting transition. After validation using experimental results, the numerical results showed that SAOs disappeared when the freestream turbulence level reached 1.25%.

2.6 Nonlinear Dynamics and Reduced-Order Modeling

2.6.1 Phenomenological modeling of stall flutter

Under uniform freestream conditions, the self-sustained nature of stall flutter oscillations can be phenomenologically represented by a van der Pol (VdP) oscillator [70]. As noted by Dowell [71], pitch-only stall flutter is a one-DOF self-excited instability driven by negative aerodynamic damping, wherein the fluid flow performs net positive work on the structure over a complete cycle. From an energetic perspective, if the cycle-integrated aerodynamic work is positive, the oscillation amplitude grows until a nonlinear mechanism limits the motion. Physically, two essential components are required: (i) a loss of equilibrium stability due to net negative aerodynamic damping that overcomes the inherent structural damping, and (ii) a nonlinear saturation mechanism that stabilizes the motion into an LCO rather than allowing for divergent oscillations. These elements are compactly captured by the VdP oscillator, which serves as a minimal phenomenological model for stall-flutter dynamics [70]. In this framework, a "minimal model" refers to a reduced-order governing equation designed to capture the fundamental features of the instability, specifically the competition between energy extraction and nonlinear saturation,

without the computational overhead of resolving the underlying flow field.

The canonical form of the unforced van der Pol oscillator is given by

$$\ddot{x} - \mu(1 - x^2)\dot{x} + \omega_0^2 x = 0, \tag{2.1}$$

where ω_0 is the natural frequency and μ is a positive parameter governing the strength of the damping nonlinearity. The term $-\mu(1 - x^2)\dot{x}$ acts as a nonlinear damping function: for small amplitudes ($|x| < 1$), the damping is negative, promoting exponential growth of the oscillation from rest. Conversely, for large amplitudes ($|x| > 1$), the damping becomes positive, dissipating energy and limiting the motion. The balance between this small-amplitude amplification and large-amplitude dissipation results in a stable periodic solution known as a limit cycle, the shape and period of which are strictly determined by the system parameters rather than the initial conditions.

Although originally developed for electrical circuits, the VdP oscillator has found widespread application in modeling fluid-structure interactions, particularly for vortex-induced vibrations (VIV) and wake oscillators [72]. In the context of stall flutter, its utility lies in its ability to capture the self-sustained LCO. Unlike linear models that predict unbounded growth beyond the flutter speed, the VdP model inherently accounts for the amplitude saturation caused by massive flow separation and dynamic stall vortex shedding. This makes the VdP oscillator an ideal candidate for investigating forced response scenarios under external perturbations, enabling the analysis of frequency synchronization phenomena [73]. Furthermore, the reduced-order nature of the model facilitates the use of standard perturbation techniques, such as the method of averaging or the method of multiple scales, to derive analytical insights into the system's nonlinear behavior [74].

2.6.2 Lock-in

When the self-excited oscillator described above is subjected to an external perturbation, such as a periodic gust, the system enters a regime of forced nonlinear dynamics. In this state, nonlinear aeroelastic responses can deviate markedly from linear predictions, exhibiting complex phenomena such as lock-in (also termed synchronization or frequency entrainment) and amplitude modulation (beating) arising from multi-frequency interactions. From the perspective of the self-excited oscillator, lock-in occurs when its LCO frequency synchronizes with an external or parametric excitation over a finite detuning interval; within this synchronization band, the response frequency follows the input frequency, phase slips vanish, and response amplitudes typically increase [70], [73]. Outside the lock-in band, unmatched frequency coupling produces amplitude modulation, also known as beating, observable as distinct envelopes in the time-history data [74]. The underlying mechanisms of these synchronization states depend on the excitation type: 1:1 lock-in is classically associated with external forcing, whereas parametric modulation results in 2:1 synchronization tongues, often referred to as Arnold tongues [73].

Lock-in has been extensively studied within the framework of fluid mechanics. In fluid-structure interaction, lock-in typically arises when an intrinsic oscillator (such as a structural or self-excited aeroelastic mode) adjusts its frequency and phase to an external or internal excitation over a finite detuning interval, leading to frequency entrainment, suppressed phase slips, and often enhanced oscillation amplitudes. Canonical examples include vortex-induced vibrations of bluff bodies [75], [76], [77]. In that canonical system, outside lock-in, the elastically mounted cylinder oscillates at the vortex-shedding frequency; as the shedding and structure's natural frequencies become sufficiently close, two-way fluid-structure coupling synchronizes shedding and motion to a common frequency near the natural frequency, with a marked increase in the oscillation amplitude.

Similar synchronization has also been observed in aeroelastic systems. In particular,

a previous work, conducted by the RMC research group, reported a coupled lock-in in pitch-heave stall flutter [61], i.e., away from lock-in, the pitch LCO primarily drove a modest heave response at the pitch-dominated modal frequency, whereas near a unity ratio of the uncoupled natural frequencies, the heave motion fed back onto pitch, the primary LCO frequency shifted and locked to the heave-dominated modal frequency, and a pronounced amplitude exchange occurred (heave amplification with a concurrent reduction in pitch). This pitch-heave lock-in mirrored the canonical cylinder-wake lock-in, where wake shedding and structural motion mutually adjust until they synchronize via feedback.

It is important to distinguish the coupled lock-in from the somewhat related case that is the focus of the present study: synchronization between a nonlinear self-sustained oscillator (stall flutter) and a harmonic input (transverse or longitudinal gust) without feedback from the oscillator to the input. Such externally forced synchronization has been investigated within the aeroelasticity frame. For instance, Tregidgo *et al.* (2012) demonstrated that free-to-roll rectangular wings subjected to forced (prescribed) periodic pitching underwent frequency lock-in of their self-sustained roll oscillations with the imposed excitation [78]. Together, these studies highlighted the universality of lock-in across nonlinear systems and emphasized that aeroelastic oscillations are highly susceptible to synchronization under external perturbations.

2.7 Aeroelastic Response to External Flow Excitation

By applying linear analytical methods of unsteady aerodynamics—specifically the superposition of Wagner and Küssner functions—extensive research has been conducted on the influence of external flow excitation on aeroelastic instability. Poirel and Price (1997) [10] extended the linear methods and investigated a structurally nonlinear airfoil encountering

longitudinal turbulence, utilizing an analytico-numerical method to model a hardening-type, cubic structural nonlinearity in pitch. Their findings indicated that flutter occurred at a lower flow velocity for the excited case compared to the so-called non-excited one, whereas the onset of LCO occurred at a higher velocity. Subsequent studies incorporated vertical turbulence components to further investigate these effects [11]. It was observed that because longitudinal turbulence primarily modulates the aerodynamic damping, resulting in instances of near-zero transient damping, the system response becomes significantly more sensitive to vertical perturbations, particularly at airspeeds below the nominal instability threshold.

More recently, Zhang *et al.* (2020) [8] studied the gust response of aeroelastic systems with two types of structural nonlinearities: free-play and hysteresis. The examined vertical gust profiles were discrete 1-cosine and sharp-edged, as shown in Fig. 2.5. In their study, the basin of attraction involving the initial conditions and gust strength was obtained for the onset of instability. It was found that a sufficiently strong gust may trigger an advanced LCO in the subcritical flow regime due to the presence of structural nonlinearities. Furthermore, larger oscillation amplitudes were observed in the presence of gusts. To alleviate the gust response and suppress flutter, a control surface was introduced in the system with a free-play flap hinge and an uncertain Nth-order polynomial stiffness nonlinearity in pitch [9]. An adaptive controller based on the partial feedback linearized system and estimation update law was developed, and it succeeded in suppressing the gust disturbance.

Although the analytical methods can help the understanding of the effects of unsteady aerodynamics, they have many non-negligible limitations when nonlinear effects cannot be neglected. To improve their reliability, validation and correction from experiments or high-fidelity CFD simulations are needed. To the best of the author's knowledge, experimental studies are underexplored regarding the effects of external flow excitation on aeroelastic response, be it transverse or horizontal. A few relevant studies were as follows. Mai *et*

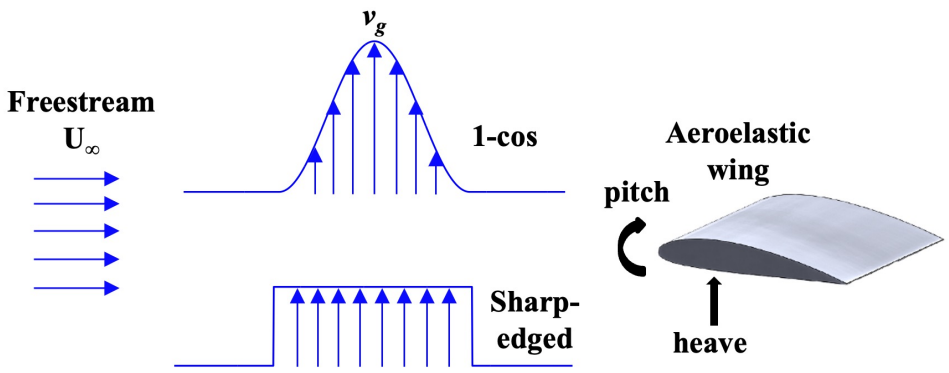

Figure 2.5: Schematic of an aeroelastic wing encountering vertical gusts with discrete 1-cosine and sharp-edged profiles.

al. (2011) [21] experimentally studied the gust response of a cantilever wing to a 2D oscillating wing upstream using PIV as the measurement system in the transonic wind tunnel. Similarly, but at a lower airspeed condition, Dowell *et al.* (2019) used a rotating slotted cylinder as a gust generator to excite an aeroelastic cantilevered wing [79]. They showed that the gusts have significant effects on the amplitudes of LCOs of the wing when the rotating frequency of the slotted cylinder was close to the flutter frequency of the wing. When the forced frequency was much higher than the LCO frequency, there was an apparent suppression effect on the amplitude of LCO. Since the tested wings were just right behind the gust generators, the generated flow perturbation contained a complex structure in the two aforementioned experimental studies. The complexity of the wake flow of oscillating wings will be demonstrated in Chapter 4. To gain a more comprehensive understanding of the complex aeroelastic response to external flow excitation, it would be better to start the investigation with simple harmonic gusts.

2.8 Summary of Knowledge Gaps and Research Questions

2.8.1 Aerodynamic response to transverse gusts

Based on the literature survey in Sections 2.2–2.3, the response of a static airfoil approaching or immersed in the post-stall regime when subjected to external flow excitation remains less understood. Specifically, the interaction with harmonic transverse gusts of significant intensity alters the effective angle of attack, potentially triggering dynamic stall phenomena distinct from those observed in steady flow with a pitching wing. To the best of the author's knowledge, the gust-induced dynamic stall has been rarely investigated, particularly through experimental methods at transitional Reynolds numbers.

Consequently, this thesis proposes to address the following key research questions regarding the aerodynamic response to harmonic transverse gusts:

- **Aerodynamic response regimes:** How does a stationary wing respond to harmonic transverse gusts as the effective angle of attack crosses from the pre-stall regime to the post-stall regime? Specifically, can linear theories (such as Küssner's and Sears functions) accurately predict the response at transitional Reynolds numbers, or do nonlinearities emerge even before static stall?

- **The dynamic stall analogy:** Is there a physical reciprocity or analogy between the classical harmonically pitching airfoil problem and the harmonic transverse gust problem? Do the hysteresis loops in lift and moment generated by alternating gust upwash/downwash mirror those generated by the upstroke/downstroke of a pitching wing?

- **Flow transition effects:** How does the state of the boundary layer (laminar vs. turbulent) affect the gust response? Specifically, does advancing the transition mit-

igate the severity of gust-induced dynamic stall or alter the hysteresis loop pattern?

- **Parametric sensitivity:** How do variations in gust amplitude and Reynolds number influence the onset and severity of the nonlinear aerodynamic response?

2.8.2 Aeroelastic response: stall flutter under gusts

Based on the literature survey in Sections 2.5 - 2.7, moving beyond the static aerodynamic response, the coupling between unsteady gust loads and the structural dynamics of a fluttering wing remains a largely open frontier. To the best of the author's knowledge, the nonlinear aeroelastic response to harmonic gusts, specifically in the context of stall flutter, has not been intensively investigated experimentally. While the VdP oscillator serves as a robust phenomenological model for stall flutter in uniform flow, its applicability to gust-excited systems requires rigorous validation.

Consequently, the following core questions are posed regarding the aeroelastic interaction:

- **Gust-flutter interaction regimes:** How do harmonic transverse and longitudinal gusts affect the post-onset behavior of self-excited stall flutter? Specifically, under what conditions do nonlinear synchronization phenomena, such as frequency lock-in and quasi-periodic amplitude modulation, emerge in the experimental response?

- **Gust effects on the flutter boundary:** How do harmonic gusts modify the stall-flutter instability boundary? Specifically, do these gusts shift the onset condition (e.g., the critical freestream speed), and if so, in what direction and by how much?

- **External vs. parametric forcing mechanisms:** In the linear regime, a transverse gust acts as an external forcing driver, while a longitudinal gust acts as a parametric modulator. A critical question addressed in this thesis is whether these distinct mechanisms persist in the nonlinear regime of stall flutter. Specifically, what

are the fundamental differences in the excitation mechanism between transverse and longitudinal gusts, and how do these differences dictate the synchronization behavior (e.g., the emergence of 1:1 versus 2:1 lock-in bands)?

- **Reduced-order modeling:** Can minimal phenomenological models, specifically the externally-forced and the Mathieu-type VdP oscillators, manage to interpret and predict those complex aeroelastic behaviors? Can these reduced-order models capture the distinct spectral signatures and synchronization bands observed in the experiments?

Chapter 3

METHODOLOGY

3.1 Gust Generator Design and Manufacture

The experimental setup for this research was designed by the author and built specifically for the low-speed wind tunnel in the Department of Mechanical and Aerospace Engineering of RMC. The test section has cross-sectional dimensions of 0.76 m $\times$ 1.08 m. This tunnel provides a low-turbulence airflow, with a turbulence intensity level of the primary flow direction lower than 0.2%. To generate controllable gusts in a wind tunnel, motor-actuated vanes mounted upstream are commonly used to turn the incoming airflow [22], [25]. The number of vanes was determined considering flow uniformity. Two vanes have better uniformity when compared with one, while further increasing the number of vanes causes too high blockage [25]. The schematic in Fig. 3.1 depicts the gust generation concept, which includes two independently controllable vanes. The survey of the generated flow is conducted by a sweeping hot-wire probe with data acquisition.

Based on the aforementioned concept, a gust generator is designed using SOLIDWORKS, as shown in Fig. 3.2, which is composed of one mounting frame, two 3D-printed vanes, and two independent AC servo motors with corresponding servo drives. The model of the AC motors is APM-SC08ADK-52. It has a rated power of 825 W with a rated torque of 2.55 Nm and a peak torque of 6.88 Nm. The independence of the motors enables the generation of multiple types of flow. Gust vanes with in-phase pitching motions and

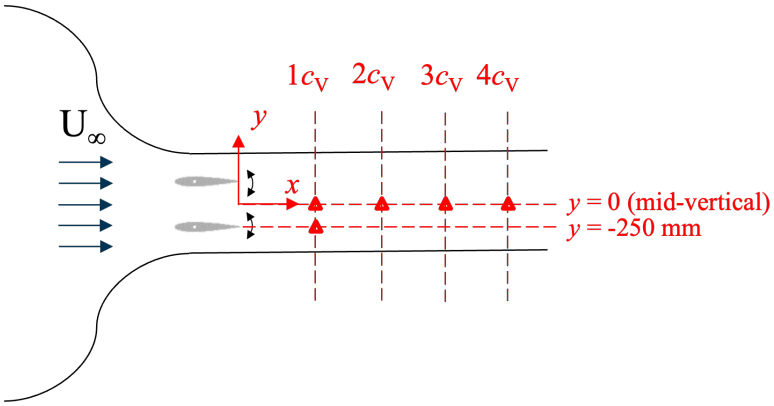

Figure 3.1: Schematic of the experimental setup and probe sweep for wake flow survey at different locations downstream.

anti-phase motions like "clapping", with the same amplitude, generate transverse and longitudinal gusts, respectively. A gust pattern with a continuous sinusoidal profile is the first focus at this stage. Discrete gusts with other profiles, such as 1-cosine, can also be generated.

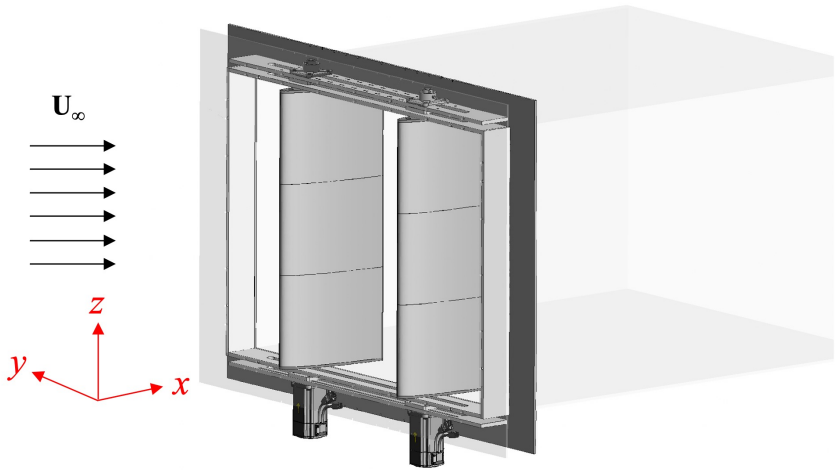

Figure 3.2: SOLIDWORKS design of the gust generator, composed of two NACA0015 vanes with a chord length of 0.3 m and a spacing of 0.5 m from each other.

The setup has the following flexibility: adjustable transverse positions of two vanes, relocation of the rotation center, and alteration of the chord length and airfoil profile. For the current setup, the two vanes are positioned symmetrically about the middle in the y-direction, separated from each other by 0.5 m. This spacing can be adjusted according to

the flow survey results of the dynamic scenarios. The profile of the vanes is the NACA0015 airfoil, which has a higher stall angle than the commonly-used NACA0012 airfoil [80]. The chord length is 0.3 m with the rotation center at $0.3c_V$ from the leading edge. Fig. 3.3 shows the completed experimental setup mounted to the inlet of the test section. To minimize the 3D effects, the vanes have a full span in the z-direction, with only 2 mm gaps between their ends and the frame. The angular placement of two vanes was recorded by two potentiometers, which can convert the rotational motion to electric voltage signals.

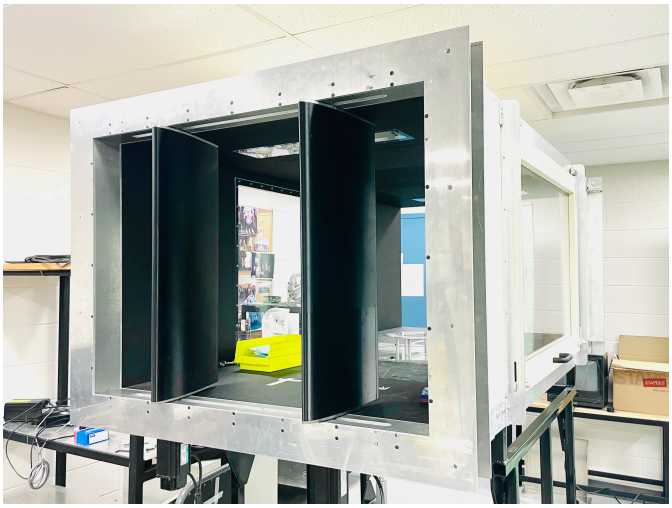

Figure 3.3: Two motor-actuated vanes mounted on the test section inlet.

3.2 Flow Measurement Using Hot-Wire Anemometer

The two components of the airflow velocity are measured simultaneously using a constant-temperature anemometer (CTA) with an X-hot-wire as the probe. A CTA measures flow velocity by maintaining one or more thin hot-wires at a nearly constant temperature using electronic feedback. The typical wire temperature is between 200 °C and 300 °C. This measurement technique relies on the principle of convective heat transfer, assuming the ambient flow temperature remains sufficiently below the wire's set point to ensure a net heat loss from the sensor. As the passing flow cools the wire, its electrical resistance fluctuates; the CTA immediately adjusts the heating current (or voltage) to restore the

target temperature. The resulting electrical power consumption is then correlated to the local flow velocity. Distinguished by its ability to respond to velocity fluctuations within microseconds, the CTA remains a superior instrument for capturing high-frequency turbulence characteristics and unsteady flow phenomena [81]. The CTA used in this study is capable of acquiring data up to 500 kHz.

As displayed in the schematic in Fig. 3.4, the probe employed in this study is composed of two single inclined hot-wires mounted to prongs on two parallel planes. The wires are made of platinum-plated tungsten with a diameter of 5 μm. Before the flow measurement, the X-hot-wire probe (connected to the CTA) requires two calibrations: (i) Angular calibration, performed with a motor-driven rotary table, determines the two wire yaw angles relative to the probe axis and is performed once, remaining valid unless the probe is damaged or remounted; (ii) Velocity calibration maps CTA voltages to flow speed and is performed prior to each measurement to remove CTA offsets, with the reference speed obtained from a pitot tube with a PX154-001DI pressure transducer. All calibrations are carried out in situ at the measurement location, so no mounting-angle correction is needed. As shown in Fig. 3.5, the velocity and angular fits overlay the data (R, coefficient of determination, ≈ 1) closely, exhibiting negligible uncertainty from calibrations. As shown in Fig. 3.6, the probe is mounted on the slide positioner for flow survey, which will be detailed in Chapter 4.

3.3 Test Wing Design with Balance

After completion of the flow survey, the test wing with a balance is mounted in the test section. It is common to mount the balance at the root [6], [38], [82] due to adequate operability and ease of construction. However, this design introduces an undesired large-scale bending moment from the lift, which can strain the balance cell. Increasing the sensing range to accommodate this load typically results in a reduction in resolution.

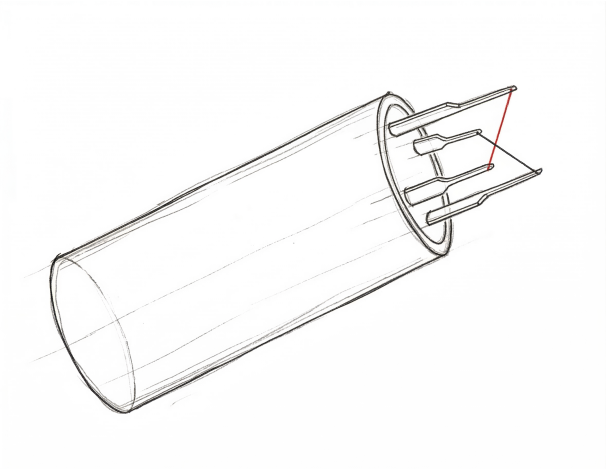

Figure 3.4: Enlarged sketch of an X-hot-wire probe.

Therefore, an improved design for the stationary test wing is achieved by mounting the balance inside the wing at mid-span to eliminate the bending moment. The internal balance also maintains the flow field intact, compared with mounting the balance midspan but externally as used in Refs. [7], [29]. The test wing has a chord length c_W of 0.18 m and a span of 0.6 m. The center of the balance is located at $0.3c_W$ from the leading edge, where the thickness of the wing is at a maximum of 21.6 mm.

The selected balance cell is an ATI Nano17, with a diameter of 17 mm. The balance has a sensing range of 25 N for planar forces, 35 N for the normal force, and 250 Nmm for the torque (moment). Its resolutions are 1/160 N for the force and 1/32 Nmm for the torque. To contain the cell inside, the balance cell is designed to be located at $0.3c_W$, which has the maximum thickness. With maximum freestream velocity being 15 m/s, the maximum lift is around 17 N, and its corresponding aerodynamic moment about $0.3c_W$ from LE is around 155 Nmm by estimation using the linear aerodynamic estimation, both of which are within the sensing ranges.

The test section design, shown in Fig. 3.7, includes a stationary wing with two end plates to minimize the 3D effects. The enlarged test wing depicted in Fig. 3.8 shows the balance positioned inside the wing at mid-span between the lower and upper rods. Notably, the lower rod is completely decoupled from the wing's internal structure. In

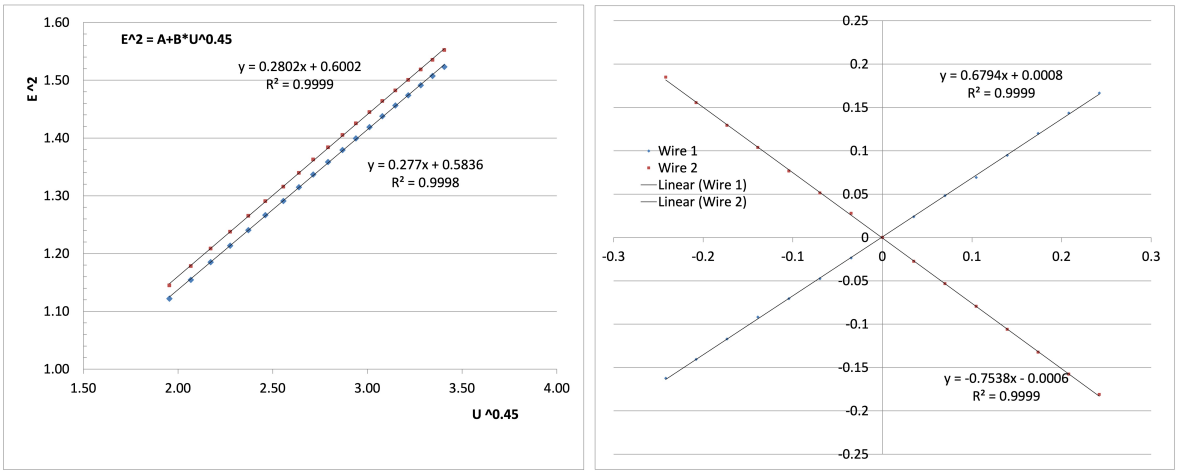

(a) (b)

Figure 3.5: Calibration diagrams for the X-hot-wire probe: (a) velocity calibration relating the squared bridge voltage (E_i^2) to the reference velocity ($U_\infty^{0.45}$) via King's Law; (b) yaw angle calibration used to determine the effective angles $\phi_1 = 50.82°$ and $\phi_2 = -58.43°$. The deviation from the nominal $\pm 45°$ symmetry is attributed to the geometric characteristics of the in-house repaired sensors. Detailed methodology is provided in Ref. [81].

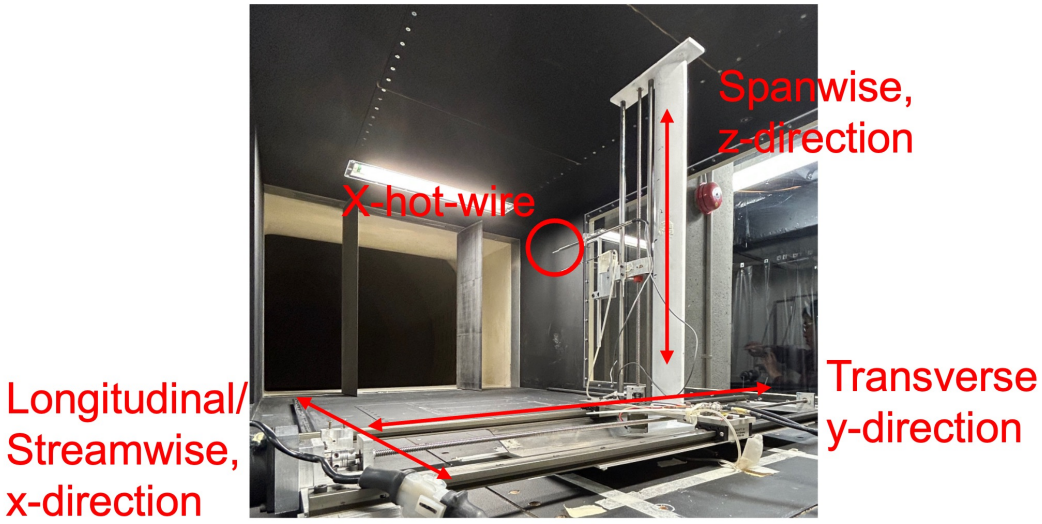

Figure 3.6: Gust generator is composed of two motor-actuated vanes mounted upstream of the test section. An X-hot-wire probe is installed on a traverse mechanism with motion possible in three directions.

contrast, the upper rod is rigidly fixed to the wing and supported exclusively by the balance cell. A plastic interface plate is situated between the balance cell and the upper rod to simplify assembly. This plastic plate is found to reduce the stiffness of the entire

test wing apparatus, which will be discussed using spectral plots in Section 5.2.2. Finally, small clearances of approximately 2 mm are maintained between the wing tips and the end plates to ensure mechanical isolation.

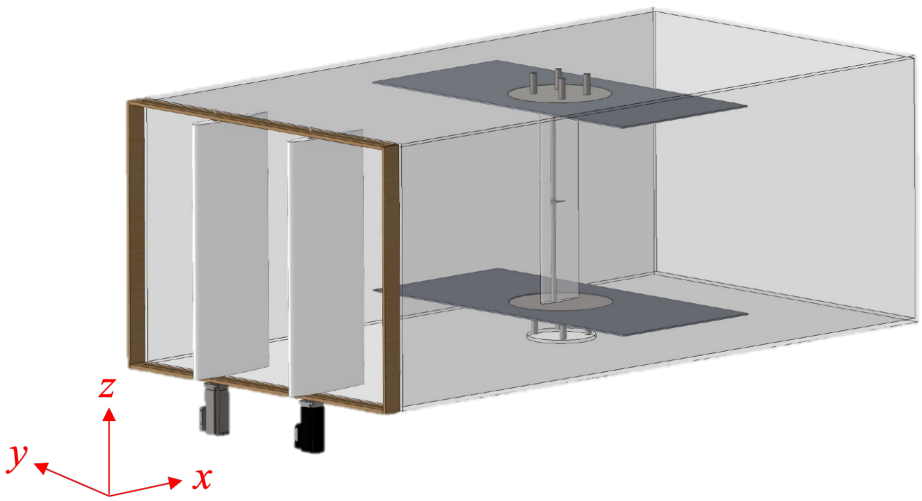

Figure 3.7: SOLIDWORKS design of the test section, including the gust generator and the stationary wing.

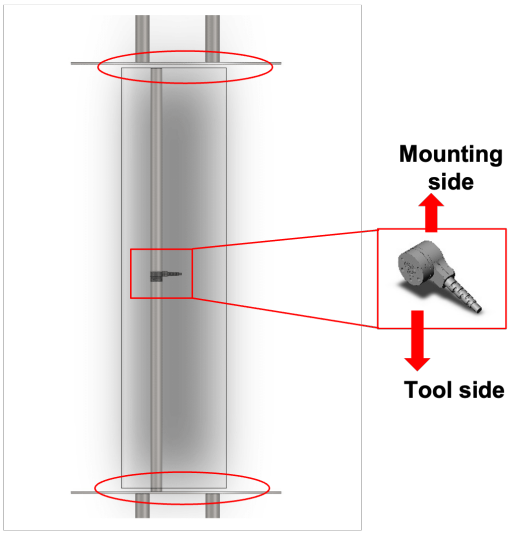

Figure 3.8: Enlarged test wing with balance cell, ATI Nano17, located internally at the mid-span; no contact between wing and end plates.

The lower steel rod acts as a cantilever beam, employing a high-stiffness steel material to minimize static bending deflection caused by aerodynamic loading (estimated mid-span

deflection $\sim 10^{-4}$ m). Resonance effects were considered by comparing the primary frequency content of the unsteady aerodynamics with the natural frequency of the structure. The first natural frequency of the beam structure is $f_{n1} = \frac{K_{n1}}{2\pi}\sqrt{\frac{EI}{\rho A H^4}}$, where K_{n1} is the first root of the characteristic equation for a cantilever beam, E is the Young's modulus of the material, I is the second moment of area (area moment of inertia) of the beam's cross-section, ρ is the density of the material, A is the cross-sectional area of the beam, and H is the length of the beam; see Ref. [83]. The estimated f_{n1} of the rod is 170 Hz, much higher than the maximum harmonic gust frequency, which is designed to be not higher than 5 Hz. The other primary frequency content is the shear layer roll-up vortices of the test wing. Based on the findings in Fig. 10 of Ref. [84], the Strouhal number for the chord Reynolds number of interest ranges from around 1.5 to 5, depending on the test AOA and freestream velocity. The shedding frequency is estimated to range from around 270 to 2400 Hz. Thus, both lower and higher frequency contents of unsteady aerodynamics are not close to the first natural frequency of the steel rod.

To examine the effects of flow transition on the aerodynamic behavior, a transition strip, made of a sand paper with 80 grit P-grade, is mounted at the leading edge of the test wing, as shown in Fig. 3.9. Both the clean wing (no strip) and tripped wing are employed to test their response to uniform flow and gusty flow. It should be noted that all measurements, including angular displacements of the vanes, mean velocity from the pitot tube, two components of airflow fluctuation, and six components of the balance cell, are recorded using a Data Acquisition (DAQ) module NI-9202 from National Instruments (NI). This 16-channel voltage input module allows simultaneous sampling, so that time/space correlation analysis can be conducted. The sampling frequency is varied from 1000 to 4000 Hz to ensure that each vane motion period has 1000 sampling points.

Figure 3.9: Test wing with a transition strip mounted at the leading edge.

3.4 Flutter Rig

To investigate the aeroelastic response to gusts, an aeroelastic apparatus is combined with the gust generator. The aeroelastic apparatus, hereafter referred to as the "flutter rig", features a rigid NACA0012 wing but flexibly mounted to permit two DOFs: pitch (θ) and heave (h), as shown in Fig. 3.10. The end plates on both spanwise sides promote quasi-2D flow. The wing has a chord length of 0.156 m and a span of 0.61 m. A key feature of the rig is the adjustable elastic axis, which enables the exploration of various flutter dynamics, as discussed in the subsequent paragraph. Comprehensive details regarding the wind tunnel facility and the mechanical design of the apparatus are provided by Poirel et al. [65].

The apparatus has been successfully used in recent aeroelasticity studies [59], [60], [85], [86] under uniform flow conditions, demonstrating the capability to exhibit fundamental aeroelastic phenomena, both linear and nonlinear. The previous studies involved lam-

inar separation flutter (LSF) featuring small-amplitude oscillation, coupled/coalescence flutter (CF) and stall flutter (SF) featuring large-amplitude oscillation. The well-known CF arises when two or more aeroelastic modes of a structure interact strongly, often approaching or merging in frequency, at a certain critical airspeed, resulting in dynamic instability. By contrast, SF is a self-excited limit cycle sustained by separated-flow aerodynamics (negative aerodynamic damping once dynamic stall develops), and, likewise, LSF originates from laminar flow separation but in the pre-stall regime in either the form of open laminar separation at the trailing edge or the presence of a laminar separation bubble at transitional Reynolds numbers. Thus, SF and LSF can develop in one or more DOFs.

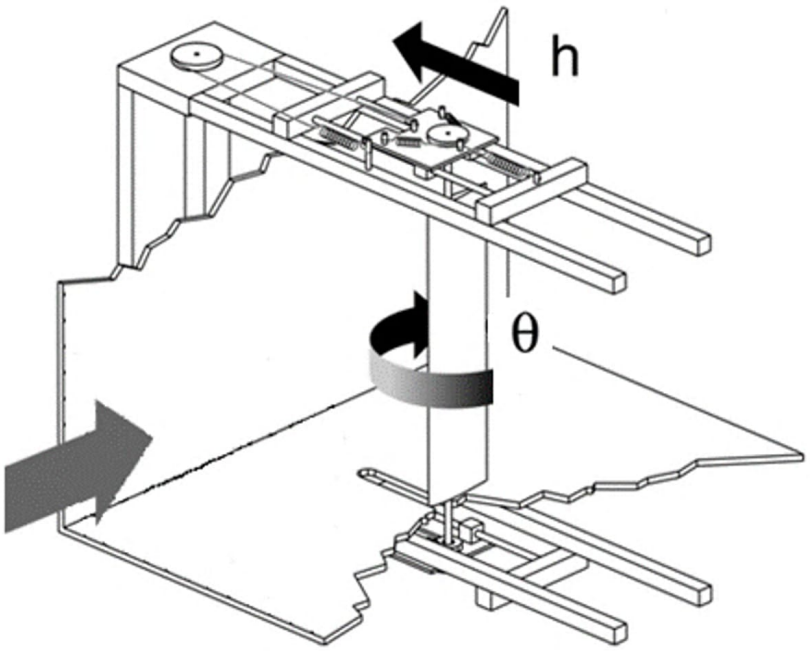

Figure 3.10: Sketch of the flutter rig composed of a rigid but flexibly mounted NACA0012 wing with two DOFs: pitch θ and heave h; adopted from Ref. [59].

Chapter 4

GUSTING FLOW SURVEY

As discussed in Section 3.2, the two components of the airflow velocity are acquired using a CTA equipped with an X-hot-wire probe. To ensure measurement accuracy, both velocity and angular calibrations are performed. The velocity calibration is conducted using a pitot tube connected to a digital pressure transducer, while the angular calibration is performed with a rotary table actuated by a stepper motor. To eliminate remounting-induced measurement error, the dominant error source for the X-hot-wire measurement, the probe is calibrated *in situ* within the test section.

Because the relative orientation of the two sensing wires is fixed, angular calibration is performed only once for a given probe. In contrast, velocity calibration is repeated prior to each measurement session to account for environmental/instrumental drifts. The uncertainty of the flow measurement is around 1.62% at $U_\infty = 10$ m/s and 6.24% for $U_\infty = 5$ m/s. The uncertainty arises primarily from the reference velocity inferred from the PX154-001DI pressure transducer. Detailed calibration procedures can be found in Refs. [81], [87]. The integration of gust vane actuation, angular displacement sensing, hot-wire calibration, and data acquisition is managed within a National Instruments (NI) LabVIEW environment.

4.1 Flow Survey Downstream of Static Vanes

Following calibration of the X-hot-wire probe, the streamwise (u) and transverse (v) velocity components are measured with the probe positioned at the transverse midpoint, $y = 0$, between the two vanes at zero AOA. The measurements are taken at $1c_V$, $2c_V$, $3c_V$ and $4c_V$ downstream of the trailing edge, as shown in Fig. 3.1. To study the relative effects of two vanes on the airflow in the test section, the vanes are removed, and airflow measurements are also conducted at the same locations. Fig. 4.1 shows the turbulence intensity for the two scenarios. For both scenarios, the presence of two zero-AOA vanes does not have a significant effect on the turbulence intensity despite modest increases for both directions.

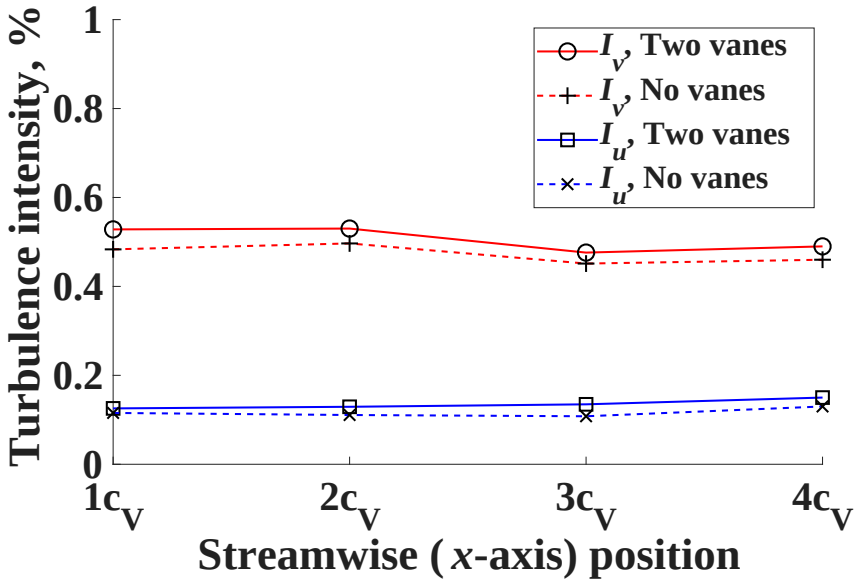

Figure 4.1: Comparison of turbulence intensity of airflow with and without vanes at $U_\infty = 10$ m/s. $I_v = \frac{\sigma_v}{U_\infty}$ and $I_u = \frac{\sigma_u}{U_\infty}$, where σ_v and σ_u are the standard deviations of v and u, respectively.

The transverse translation of the probe in the y-direction is controlled by a motor-driven slide positioner with a 700 mm range. With the vanes installed back, the X-hot-wire sensor is swept along the transverse direction on the selected cross-sections. The AOAs of the two vanes are still zero degrees. Figs. 4.2(a) and (b) show the distribution of the

mean values of u component ($\bar{u}$) and turbulence intensities of the two airflow components, respectively. The distribution is basically symmetrical about the mid-transverse position. The wake of the two vanes causes a mean velocity deficit and an increase in turbulence. The flat distribution of $\bar{u}$ between the two wake areas is around 10.08 m/s, as marked in Fig. 4.2(a), without a notable change from $1c_V$ to $4c_V$. The "troughs" of $\bar{u}$ distribution are 9.3 m/s, 9.45 m/s, 9.52 m/s, and 9.59 m/s at $1c_V$, $2c_V$, $3c_V$, and $4c_V$ downstream, respectively. It can be seen that the blockage effects of vanes weaken downstream, while the wake area slightly widens, as expected. The turbulence intensities of the flat region between the two wake areas correspond to the values shown in Fig. 4.1 for both components. A slight increase of I_v in the middle of the test section is observed for all four sweeps, increasing from around 0.4% to 0.5%. As the wake area widens downstream, the peak values drop from 3.1% and 3.1% at $1c_V$ to 1.7% and 1.4% at $4c_V$ for I_u and I_v, respectively. In addition, two peaks on each side of the I_u distribution indicate the shear layers of the wake areas, while there is only one peak on each side of the I_v distribution, located right behind each vane.

To study the vortex shedding of vanes, spectral plots of both components were obtained for various locations behind one vane, as shown in Fig. 4.3. Initial measurements, conducted using a support system with blunt geometries behind the probe, exhibited prominent low-frequency peaks. Upon implementing streamlined structures, as illustrated in the probe sweep assembly in Fig. 3.6, these low-frequency artifacts were eliminated. This confirms that the initial measurement hardware induced significant flow interference. Furthermore, it highlights the potential for the generated gust flow to interact with downstream test section infrastructure, a factor that was strictly accounted for in all subsequent experimental analyses.

In Fig. 4.3, the amplitude of each successive spectrum was stepped down by one order of magnitude for higher clarity, with the spectrum at $1c_V$ holding the correct magnitude. It can be seen that near the trailing edge, a high-frequency peak, around 290 Hz, was

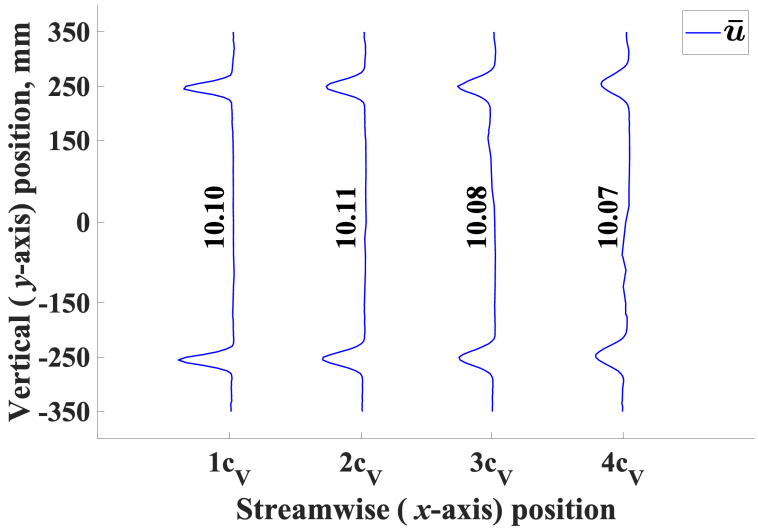

(a)

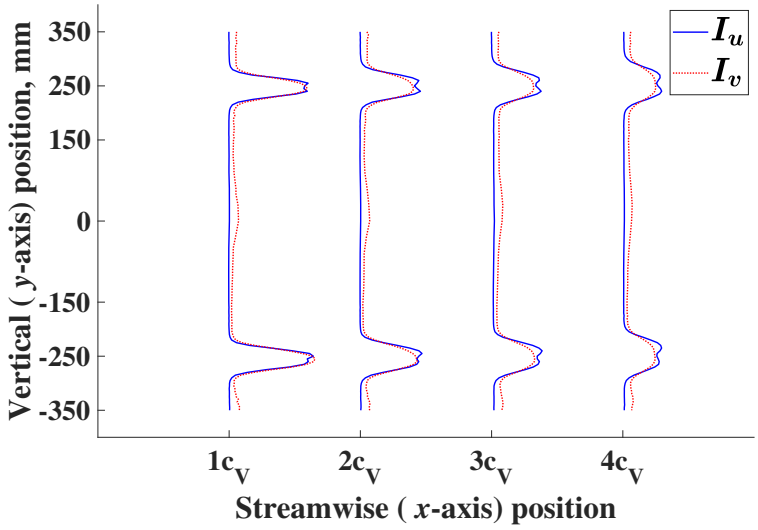

(b)

Figure 4.2: (a) Distribution of $\bar{u}$ along transverse and streamwise directions; (b) turbulence intensity of two airflow components at $U_\infty = 10$ m/s.

observed for both components. A super-harmonic peak of the dominant frequency was observed in the $1c_V$ power spectral density (PSD) curve. It may denote von Kármán vortex shedding with a corresponding Strouhal number, $Str = \frac{f_s d}{U_\infty} = 1.3$, where d is the length of the airfoil projection on a cross-stream plane and f_s is the vortex shedding frequency. This result agreed well with the findings from [84], where $Str \approx 1.1$ at a close Reynolds number. Note that although they used the same definition of the Strouhal number as here, a NACA0025 airfoil was used for their study. When placing the sensor downstream to $4c$, the vortex-shedding effects were no longer intense.

The spectral analysis at the wake centerline ($y = -250$ mm) reveals a distinct suppression of the vortex shedding frequency in the u component, despite its dominance in the v spectrum (Fig. 4.3). This behavior correlates directly with the turbulence intensity profiles shown in Fig. 4.2(b), where the I_u distribution exhibits a local minimum or "valley" between two shear layer peaks, whereas the I_v distribution peaks centrally. This phenomenon is consistent with the geometric properties of a Kármán vortex street, where transverse velocity fluctuations are maximized on the wake centerline, while streamwise fluctuations at the fundamental shedding frequency are minimized in this region due to symmetry. Consequently, the wake centerline acts as a localized "blind spot" for detecting shedding via the streamwise component.

To verify that this suppression is spatially dependent rather than an inherent limitation of the streamwise component, the probe is traversed across the wake shear layers at $1c_V$ downstream. As displayed in Fig. 4.4, the spectral energy of the shedding frequency in the u component recovers significantly as the measurement point shifts away from the centerline (e.g., -240 mm or -260 mm). The PSD curves exhibiting lower peaks in Fig. 4.4 correspond to the probe positions within the I_u valleys noted in Fig. 4.2(b), while the stronger spectra correspond to the high-turbulence shear layers. This confirms that the streamwise velocity signal is highly sensitive to probe positioning relative to the wake shear layers.

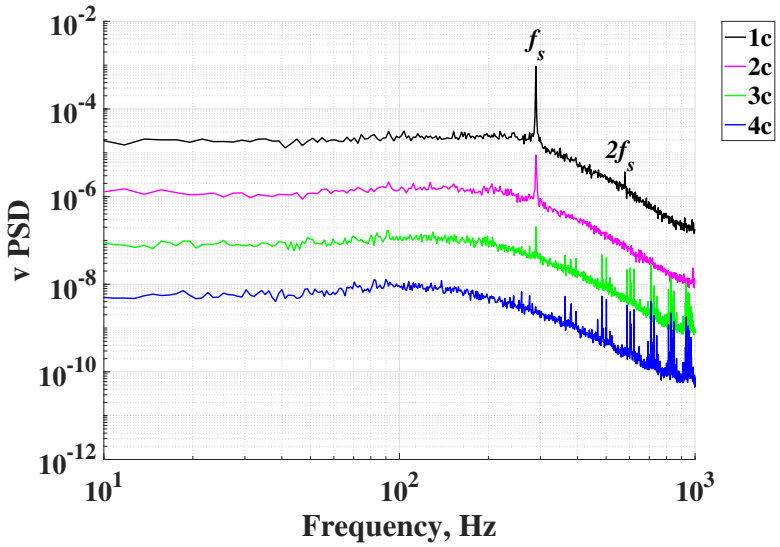

(a)

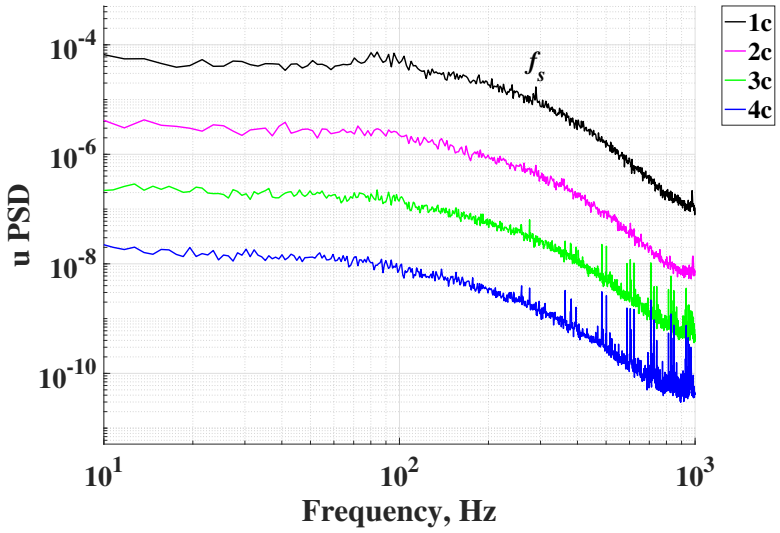

(b)

Figure 4.3: Spectra of (a) v component and (b) u component, at various positions along streamwise direction at 250 mm from mid-transverse position (right behind one static vane) for $U_\infty = 10$ m/s. The amplitude of each successive spectrum was stepped down by one order of magnitude for higher clarity, with the spectrum at $1c_V$ retaining the correct magnitude.

This finding offers a critical refinement to previous experimental conclusions regarding vortex shedding detection. Yarusevych *et al.* [84] reported that wake vortex shedding could not be detected in streamwise velocity spectra and was only revealed in the transverse component. This discrepancy was used to explain the non-detection of shedding

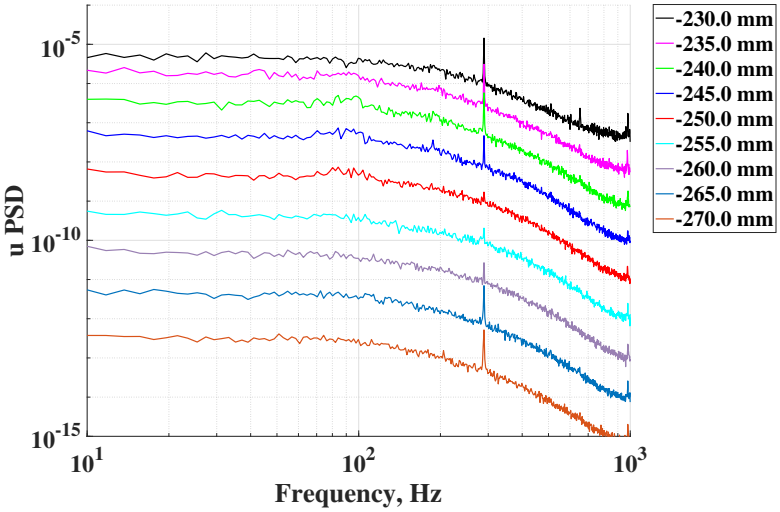

Figure 4.4: Spectra of u component between the two wake shear layers, at various positions along the transverse direction, $1c_V$ downstream for $U_\infty = 10$ m/s.

in the earlier work of Huang and Lin [62], who utilized one-component normal hot-wires sensitive only to u velocity magnitude rather than direction. However, the present results suggest that the inability to detect shedding in the u component reported in these studies likely stems from positioning the probe near the wake centerline (the point of maximum velocity deficit) rather than in the shear layer. While the v-component is indeed a more robust metric at the centerline, the u component is equally capable of capturing vortex shedding if the sensor is correctly positioned within the regions of high shear.

4.2 Flow Survey Downstream of Dynamic Vanes

Following the flow survey downstream of the two static vanes, dynamic scenarios are investigated. The fundamental in-phase vane motion is studied employing a sinusoidal profile with 10° amplitude ($\bar{\theta}_V$) and 1 Hz frequency. The freestream velocity is 10 m/s at first and then adjusted to 5 m/s to obtain a larger GR.

Figure 4.5 shows the results measured at the mid-transverse position ($y = 0$ mm) at $1c_V$ downstream. In Fig. 4.5(a), the time histories of the angles of the two vanes nearly

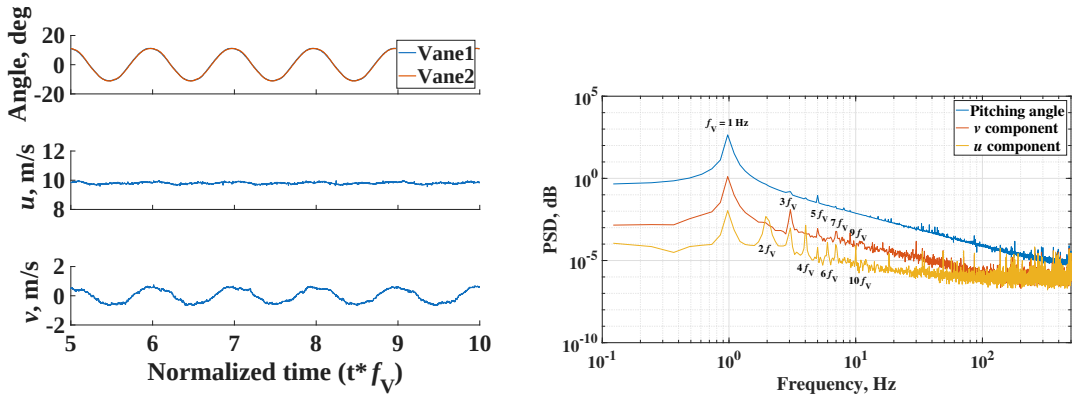

(a) (b)

Figure 4.5: Time histories (a) and spectra (b) of vane angles and two airflow components at $y = 0$ (mid-transverse), $1c_V$ downstream of vanes for $U_\infty = 10$ m/s, $f_V = 1$ Hz, $\bar{\theta}_V = 10°$.

coincide, confirming the in-phase motions. Thus, only one vane's motion spectrum is plotted in Fig. 4.5(b). At the mid-transverse position, peaks at $(2n-1)f_V$ are observed from the v spectrum, where f_V is the motion frequency of the vanes, denoting its dominant oscillation frequency. For the u spectrum, even harmonics $2nf_V$ appear, which is due to two cycles of the u variation corresponding to one cycle of the v variation when the vanes perform symmetric sinusoidal motion. Compared with the static scenarios, the mean value of the u component decreases from 10 m/s to 9.8 m/s in spite of the same operational RPM of the wind tunnel fan. The streamwise velocity decreases (losses in total pressure) are caused by the larger blockage of the oscillating vanes for the dynamic scenario.

With the probe located right behind one oscillating vane at $1c_V$ downstream ($y = -250$ mm), Fig. 4.6 shows the time history and spectra of vane angle, v, and u components. Compared with Fig. 4.5, the flow structure is more complex with some significant spikes appearing periodically in the time history. At a specific freestream velocity with a harmonic pitching oscillation, the shedding frequency changes continuously with the dynamic incidence angle of the vane. There could be a relatively intensive shedding frequency when the oscillation angle reaches the amplitude (10°). It is confirmed from the PSD plot that a broadband peak is observed in the high-frequency region when the vane oscillates at the defined amplitude, denoting the vortex shedding from the oscillating

vane. The relatively intensive peak of the broad band is $f_s = 216$ Hz with a corresponding Strouhal number $Str = 0.97$ (still using vane thickness as the characteristic length), lower than 290 Hz observed in the static scenario at 0° in Section 4.1. For cross-comparison, the Strouhal number was $Str \approx 0.95$ for the static case with AOA = 10° at a close Reynolds number in Fig. 19 of Ref. [84]. This agreement suggests that the dominant shedding frequency is linked to portions of the cycle near the oscillation extrema (where $\dot{\alpha} \approx 0$), indicating a stronger dependence on the oscillation amplitude (10°) than on the mean oscillation angle (0°).

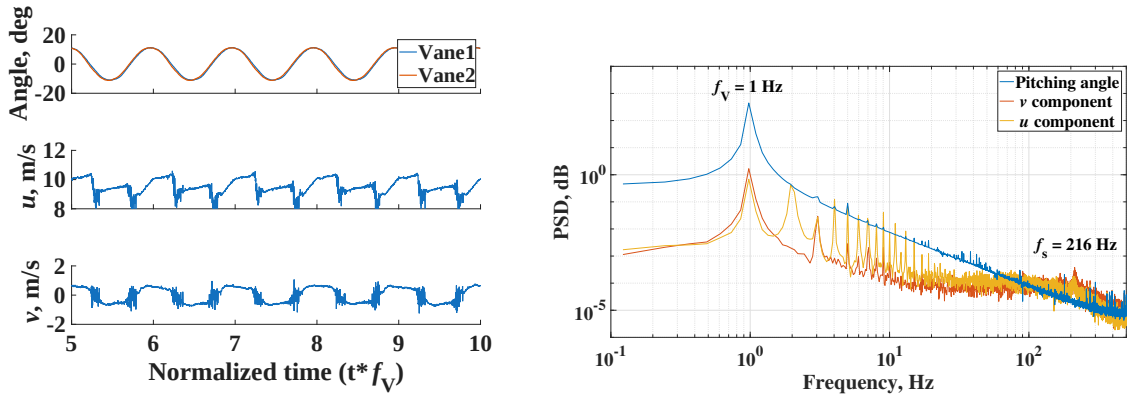

(a) (b)

Figure 4.6: Time histories (a) and spectra (b) of vane angles and two flow components measured at $y = -250$ mm (right behind one vane), $1c_V$ downstream the vane for $U_\infty = 10$ m/s, $f_V = 1$ Hz, $\bar{\theta}_V = 10°$.

The complexity of the wake flow is a primary consideration for selecting two vanes instead of a greater number, as discussed when introducing the concept of gust generation. To avoid the impact of the high-frequency flow structure, the test wing is mounted at the mid-transverse position. The flow between the shear layers of two oscillating vanes behaves as harmonic transverse-dominant gusts, similar to the flow shown in Fig. 4.5. The transverse width of this region is around 200 mm at this location, narrower than that of the static scenario shown in Fig. 4.2.

To ensure the wing is mounted in a region of stable gust characteristics, the streamwise location where the transverse gust amplitude exhibits uniform behavior was identified.

The phase-averaged (60 gust cycles) time history of the v component at four streamwise locations is shown in Fig. 4.7(a). The amplitude of v variation becomes smaller downstream from $1c_V$ to $3c_V$, while the change is marginal when comparing $4c_V$ with $3c_V$. This trend is corroborated by the spectral plots in Fig. 4.7(b), which show a notable drop in the dominant frequency peak from $1c_V$ to $3c_V$, followed by nearly identical levels at $4c_V$ to $3c_V$. Both the time-history and spectral analyses suggest that the transverse gust amplitude becomes quasi-uniform along the streamwise direction between $3c_V$ and $4c_V$, indicating an optimal location for wing placement. The point of view is further supported by the phase-averaged time histories at $U_\infty = 5$ m/s (Fig. 4.8), where the traces for $3c_V$ and $4c_V$ nearly coincide. Consequently, the test wing is mounted with its LE positioned $3c_V$ downstream of the gust vanes. The flow characteristics at this specific location are then subjected to further detailed examination.

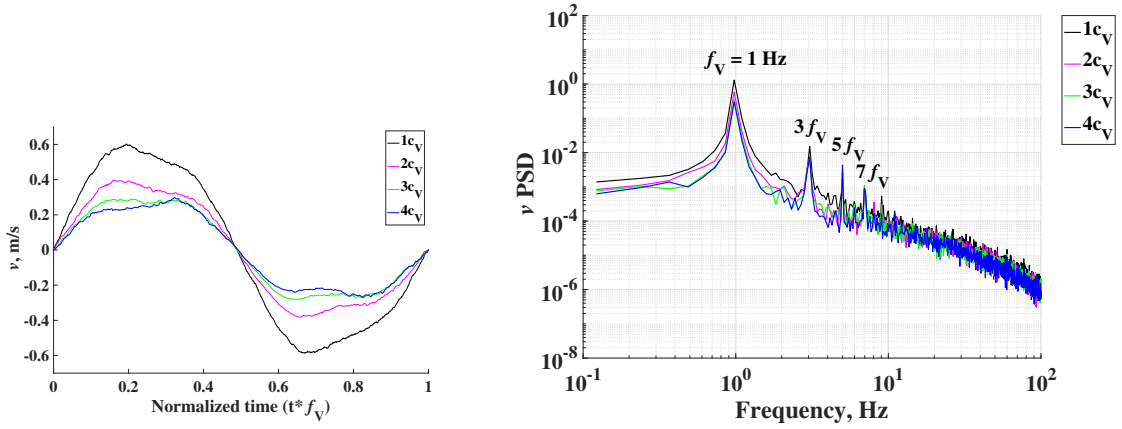

(a) (b)

Figure 4.7: Phase-averaged time histories (a) and spectra (b) of v component at four selected locations downstream at $U_\infty = 10$ m/s, $f_V = 1$ Hz, $\bar{\theta}_V = 10°$.

4.3 Transverse Gust Characteristics

To generate gusts with various amplitudes and reduced frequencies, different vane frequencies ranging from 1 Hz to 4 Hz, with the same vane pitching amplitude of 12°, are

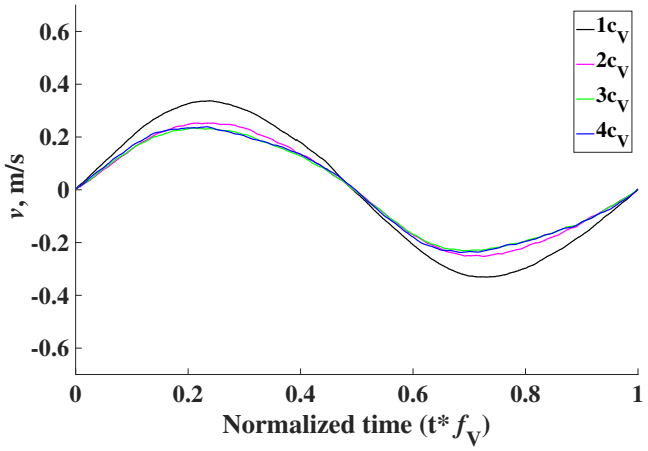

Figure 4.8: Phase-averaged time histories v component at four selected downstream locations at $U_\infty = 5$ m/s, $f_V = 1$ Hz, $\bar{\theta}_V = 10°$.

tested, and the phase-averaged results at $3c_V$ are shown in Figs. 4.9 and 4.10 for U_∞ = 10 m/s and 5 m/s, respectively. With $\bar{\theta}_V > 12°$, not shown here, the measured flow is no longer harmonic. With $\bar{\theta}_V = 12°$, the measured flow pattern is similar to that shown in Fig. 4.5 ($\bar{\theta}_V = 10°$). Hence, it is inferred that no large-scale flow separation occurs at this condition. Most of the generated transverse gusts, as shown in Figs. 4.9(a) and 4.10(a), performed harmonic-like behaviors, except that the vane frequency of 1 Hz at $U_\infty = 10$ m/s has "crater-like" shapes around their peaks. The abnormal crater-like shapes are due to the dissipation of v variation along the streamwise direction, which was also clearly observed in Fig. 4.7(a). Figures 4.9(b) and 4.10(b) show the phase-averaged results of u components at various frequencies for $U_\infty = 10$ m/s and 5 m/s, respectively. Some negligible deviations from the mean velocity are observed, as expected.

To characterize the generated flow field more precisely, the reduced frequency k, the reduced wavelength λ_g, the gust ratio GR, and the maximum gust angle $\alpha_{g,max}$ are defined

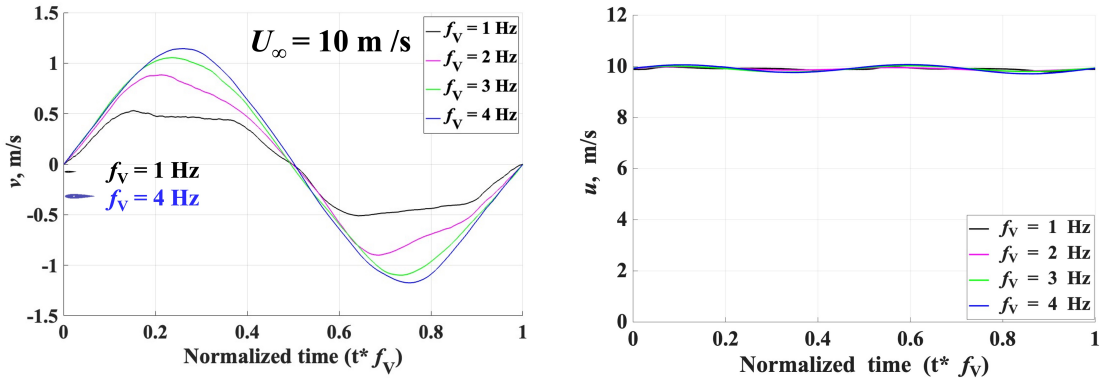

(a) (b)

Figure 4.9: Phase-averaged v (a) and u (b) components at $3c_V$ under various gust frequencies with vane pitching amplitude of 12° at $U_\infty = 10$ m/s. Two illustrated airfoils marked with corresponding gust profiles in (a) help visualize the comparison between wing chord and gust wavelength at various frequencies.

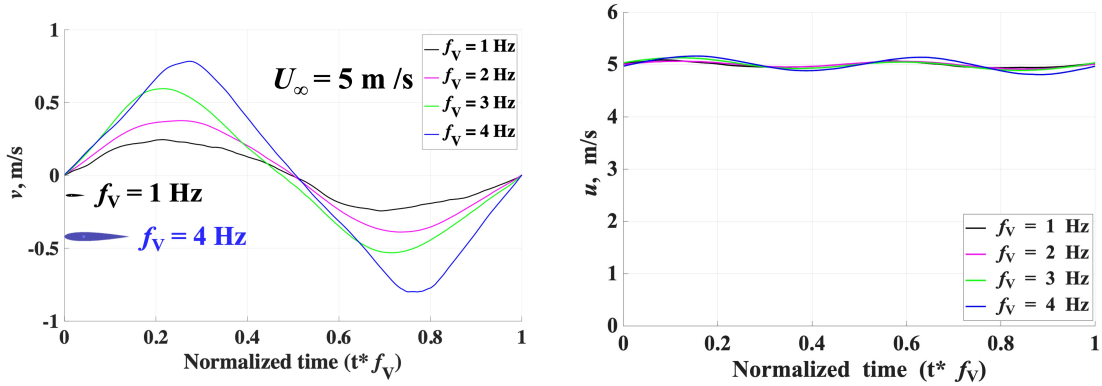

(a) (b)

Figure 4.10: Phase-averaged v (a) and u (b) components at $3c_V$ under various gust frequencies with vane pitching amplitude of 12° at $U_\infty = 5$ m/s. Two illustrated airfoils marked with corresponding gust profiles in (a) help visualize the comparison between wing chord and gust wavelength at various frequencies.

Table 4.1: Summary of transverse gust characteristics at $U_\infty = 10$ m/s and vane pitching amplitude of 12° with phase-averaged results plotted in Fig. 4.9.

f_V (Hz)	k	λ_g	GR	$\alpha_{g,max}$ (°)
1	0.057	55.6	0.052	3
2	0.11	27.8	0.089	5.1
3	0.17	18.5	0.107	6.1
4	0.23	13.9	0.12	7

Table 4.2: Summary of transverse gust characteristics at $U_\infty = 5$ m/s and vane pitching amplitude of 12° with phase-averaged results plotted in Fig. 4.10.

f_V (Hz)	k	λ_g	GR	$\alpha_{g,max}$ (°)
1	0.11	27.8	0.048	3
2	0.23	13.9	0.077	4.9
3	0.34	9.26	0.11	7
4	0.45	6.94	0.16	10

as:

$$
\begin{aligned}
k &= \frac{\omega c_W}{2U_\infty} = \frac{\pi f_V c_W}{U_\infty}, \\
\lambda_g &= \frac{U_\infty}{c_W f_V} = \frac{\pi}{k}, \\
GR &= \frac{|v_{g,max}|}{U_\infty}, \\
\alpha_{g,max} &= \tan^{-1}(GR).
\end{aligned} \tag{4.1}
$$

As defined, k is constrained with λ_g. Their values are summarized in Tables 4.1–4.2. With the same vane motion at a defined pitching amplitude, a larger gust angle can be obtained for a lower freestream velocity, as expected. It should be noted that the value of $\alpha_{g,max}$ directly depends on the selection of k at a specific airspeed. Consequently, $\alpha_{g,max}$ cannot be independently adjusted for a given k and U_∞ combination.

Among all the tests with vane frequencies at $U_\infty = 10$ m/s, $\alpha_{g,max}$ reached 7°. At

$U_\infty = 5$ m/s, as shown in Fig. 4.10, $\alpha_{g,max}$ could reach 10°. The RMC low-speed wind tunnel is designed for 4–60 m/s. Note that the gust ratios reported here are relatively modest compared with those explored in Ref. [88]. In contrast to experiments conducted in water towing tanks, where gust ratios can approach or even exceed unity, there are inherent constraints in generating strong gusts in wind or water tunnels using oscillating vanes. Specifically, the amplitude of the transverse velocity component is limited by the stall angle of the upstream vanes, and the freestream velocity cannot be reduced excessively without compromising flow quality. Despite these limitations, the peak gust amplitude achieved in this study surpasses those employed in Refs. [38], [56]. Moreover, the maximum gust-induced angle of attack, $\alpha_{g,\max} = 7°$, is sufficiently large to drive the airfoil with non-zero AOA in the pre-stal regime, e.g. 5 deg, beyond its static stall angle, thereby enabling it to enter and exit the stall regime and trigger dynamic stall phenomena, which is one of the main objectives of this study.

Figures 4.9(a) and 4.10(a) also provide a visualization of the wing–gust size for $U_\infty = 10$ m/s and $U_\infty = 5$ m/s. As shown in these visualization plots, for $U_\infty = 10$ m/s, the 1 Hz gust has a wavelength of 56 chord lengths of the black-colored wing, while the 4 Hz gust's wavelength is 14 times the chord, as shown using the lower blue wing. With a lower k (larger λ_g), the transverse gust encountering problem can be treated as only time-varying for the wing loading, which is equivalent to an oscillating airfoil problem in pure plunge. For higher k (smaller λ_g), the chordwise distribution of the time-varying gusts also needs to be considered, apart from the oscillation in plunge of the wing in a flow without gust. This inference is supported by the comparison between vector diagrams of Theodorsen's and Sears' functions [1], [4], as shown in Fig. 2.2. The former is the complex-valued function that characterizes the unsteady aerodynamic forces on an oscillating airfoil in incompressible uniform flow, and the latter is the one describing the unsteady aerodynamic response of an airfoil to a sinusoidal gust in incompressible flow. Both of them are complex functions of k. In Fig. 2.2, with k lower than 0.1 (at the right end), the two curves almost

coincide. While with k higher than 0.1, a notable deviation of the two curves gradually emerges, denoting that the gust variation along the chord cannot be neglected. From Table 4.1, some of the reduced frequencies of interest are higher than 0.1. Therefore, the chordwise distribution will be considered for the discussions regarding aerodynamic response to gusts in Chapter 5.

4.4 Longitudinal Gust Characteristics

In-phase vane motion generates transverse gusts; anti-phase motion generates longitudinal gusts. With the anti-phase vane motion, the longitudinal gusts generated are depicted in figure 4.11, behaving in a nearly harmonic pattern as desired, $u(t) = U_\infty + u_{g,max}\sin(2\pi f_g t)$. The v component variation is negligible compared with the u component. Limiting the vane oscillation to 12° (to avoid vane stall), the streamwise gust ratio, $GR_u = \frac{u_{g,max}}{U_\infty}$, depends on factors such as U_∞ and the vane rotating frequency, which is the same as the gust frequency, f_g. At $U_\infty = 10$ m/s for the current facility, $GR_u \approx$ 0.05, 0.09, 0.12, and 0.14 for $f_V = 1$, 2, 3, and 4 Hz, respectively, see Table 4.3. The longitudinal gusts are employed to excite the flutter rig to investigate the gust response of stall flutter, as demonstrated in Chapter 7.

Table 4.3: Summary of longitudinal gust characteristics at $U_\infty = 10$ m/s and vane pitching amplitude of 12° with phase-averaged results plotted in Fig. 4.11.

f_V (Hz)	k	λ_g	GR_u
1	0.057	55.6	0.05
2	0.11	27.8	0.09
3	0.17	18.5	0.12
4	0.23	13.9	0.14

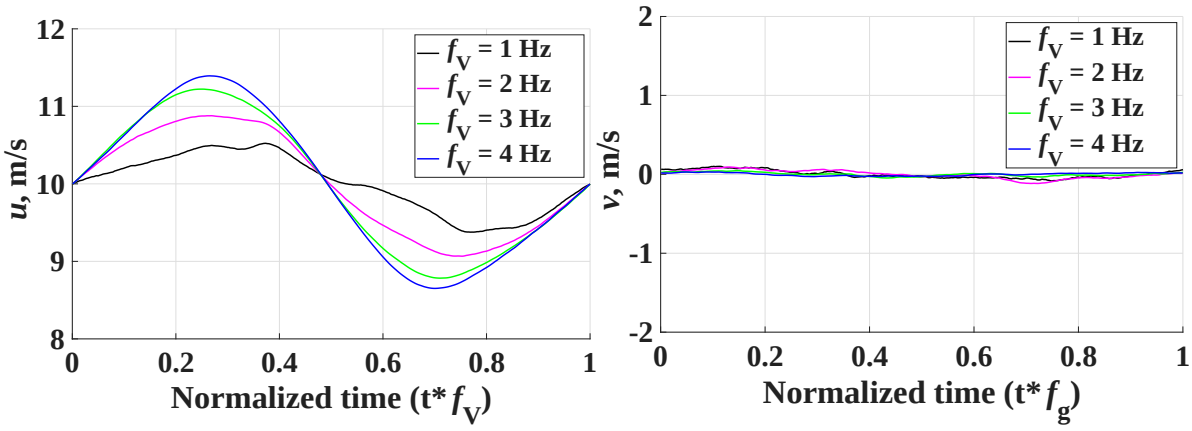

(a) (b)

Figure 4.11: Phase averaging of (a) u component; and (b) v component, at $U_\infty = 10$ m/s $3c_V$ downstream of the anti-phase oscillating vanes with various frequencies, $\bar{\theta}_V = 12°$.

Chapter 5

DYNAMIC STALL INDUCED BY TRANSVERSE GUSTS

5.1 Aerodynamic Response Under Uniform Flow

Before investigating the gust interaction, aerodynamic characteristics of the NACA0012 wing are examined under uniform flow (removing the upstream vanes) for both clean and tripped configurations, as displayed in Fig. 5.1. Three airspeeds are considered: U_∞ = 5, 10, and 15 m/s, corresponding to chord Reynolds numbers of 6.3×10^4, 1.2×10^5, and 1.9×10^5, respectively. Since the wing AOA is adjusted manually in this study, any hysteresis-loop phenomena around the static stall angle cannot be captured. At very small angles for the pre-stall range, it is observed that the C_L curves are not linear for the clean wing at all three airspeeds. The measured lift coefficient slopes at low angles are higher than 2π—the benchmark for a two-dimensional airfoil in inviscid, incompressible flow derived from Thin-Airfoil Theory. The discrepancy is due to the nonlinear low-Reynolds-number aerodynamic effects originating from laminar separation.

Introducing the transition strip at the leading edge linearized the lift behavior, altering the slope to nearly 2π at the two higher airspeeds in the pre-stall range. When comparing the pitching moment of the tripped wing with that of the clean wing in Fig. 5.1(c), the linearization effects are also remarkable. All the C_M curves tend to behave more linearly

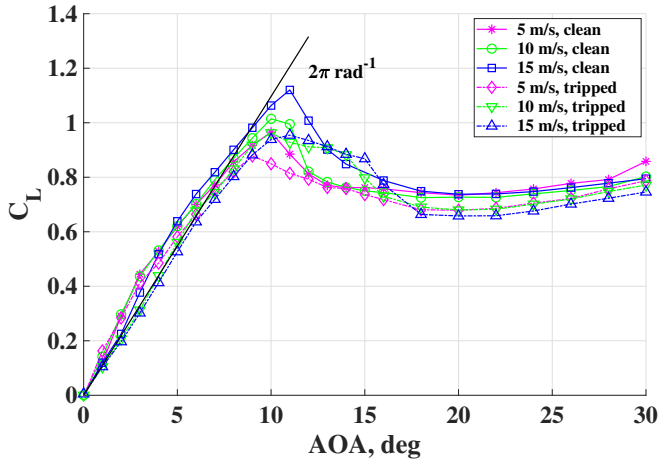

(a)

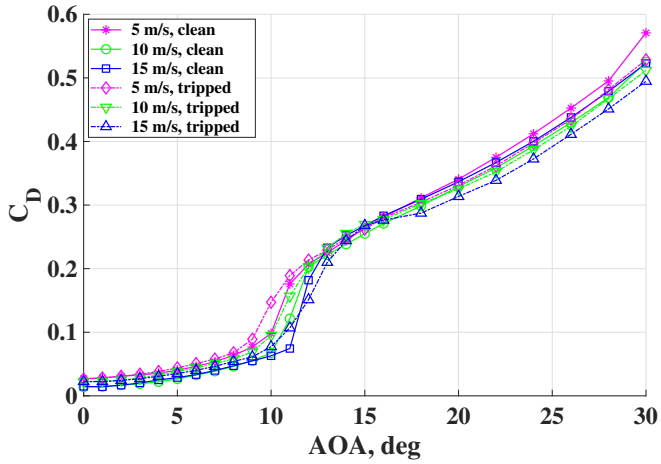

(b)

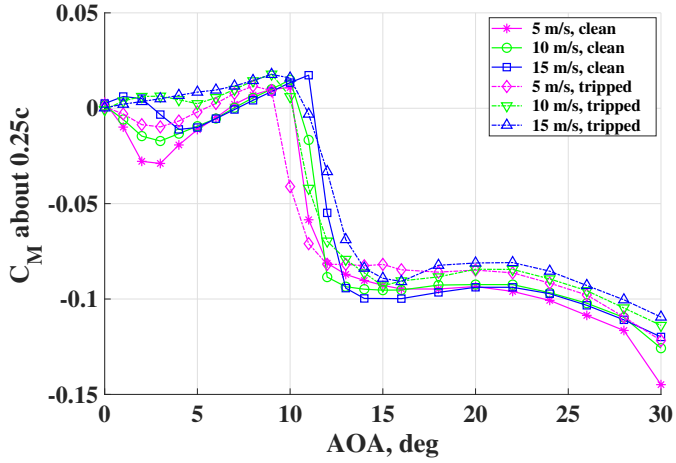

(c)

Figure 5.1: Aerodynamic coefficients under uniform flow for clean and tripped wings: (a) C_L; (b) C_D; (c) C_M about $0.25c$.

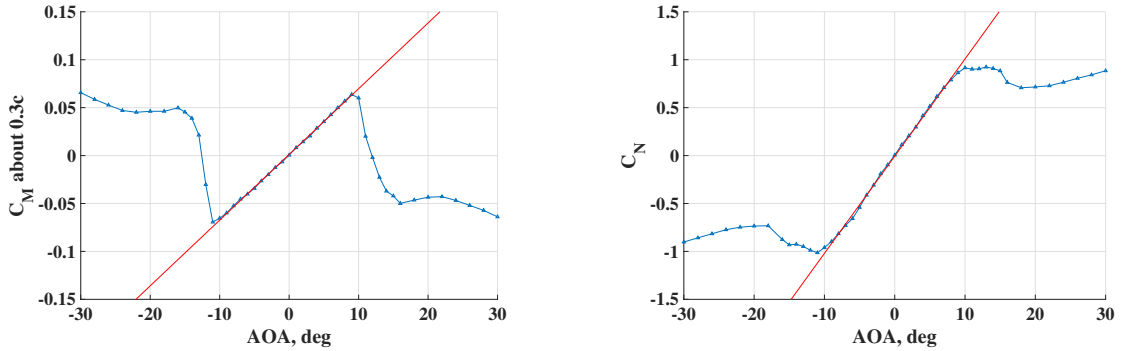

(a) (b)

Figure 5.2: Aerodynamic coefficients under uniform flow for the tripped wing at $U_\infty = 15$ m/s ($Re_c = 1.9 \times 10^5$): (a) C_M about $0.3c$; (b) C_N. Fitting slopes are used to calculate the aerodynamic center of the tripped wing.

before stall for the tripped wing. At $U_\infty = 15$ m/s, the C_M curve of the wing with the transition strip is nearly linear below 9°. The aerodynamic center is determined to be $0.232c_W$ by fitting the aerodynamic moment about $0.3c_W$ and the normal force coefficients (C_N) as linear functions of AOA in Fig. 5.2. It slightly deviates from the well-known $0.25c_W$ derived from thin-airfoil theory. This magnitude and direction of shift are consistent with roughness tests on a NACA0012 wing, which show that $C_M - \alpha$ slopes are slightly positive with roughness in Fig. 12 of Ref. [89], implying a forward shift of the aerodynamic center. The shift magnitude from quarter-chord is estimated to be $0.015c$ to $0.02c$, similar to the present finding.

Fig. 5.3 shows the standard deviation of measurements at $U_\infty = 10$ m/s for the clean wing. As expected, the standard deviation is relatively small until the static stall angle, while its sudden increase at the static stall angle is quite remarkable, especially for C_M, which shows the sensitivity of the aerodynamic moment to flow separation. Error bars of both coefficients decrease beyond deep stall angles. Similar phenomena are observed at other airspeeds and also for the tripped wing (not shown here). This gradual decrease in the standard deviation might be due to the flow being more turbulent with a different scale of eddies in the deep-stall regime.

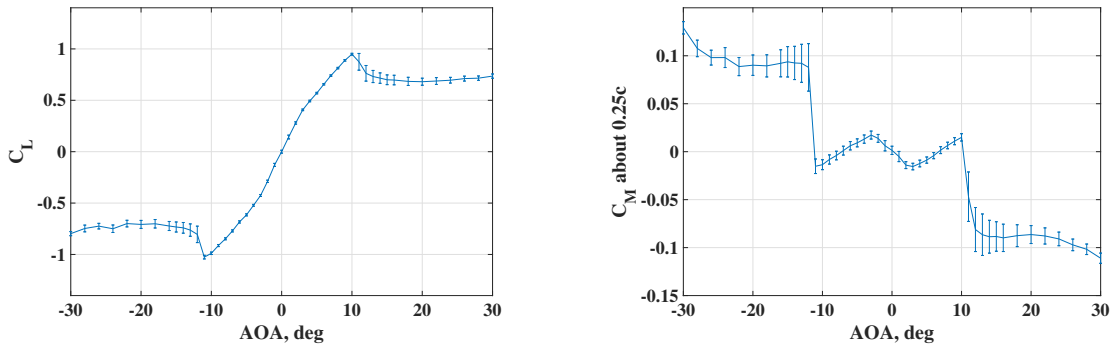

(a) (b)

Figure 5.3: Lift (a) and moment (b) coefficients under uniform flow for the clean wing at 10 m/s ($Re_c = 1.2 \times 10^5$). Standard deviation of raw data is marked as the error bar.

5.2 Aerodynamic Response to Transverse Gusts

As shown in Figure 5.4, the traversing mechanism for flow measurement is relocated whereby the X-hot-wire probe is set in the proximity of the leading edge ($\frac{1}{2}c_W$ upstream and x = -50 mm). The location of the probe is selected based on numerical results with the same configurations as experiments, which showed that the airflow velocity at this location closely represented the freestream flow field [90]. With a closer location, the flow field was disrupted by the downstream wing, especially for large AOA. Further aside ($|x| > 100$ mm), the measured flow is affected by the wake shear layers with vane motion.

To conduct a phase lag study on the gust response, simultaneous measurements of both gusty flow and the aerodynamic forces are required. In the present setup, the measurement of the vane angles, the two flow velocities, and the six balance components are sampled synchronously. Taylor's "frozen turbulence" hypothesis posits that under certain conditions, the turbulent structures in a flow are advected past a fixed point without significant evolution at a constant speed, allowing for the conversion of temporal wind speed data (measured at a fixed point) into spatial information [91]. By assuming the gusts travel along the local streamwise flow, the gust wave in both time and space

Figure 5.4: Clean wing mounted in the test section and an X-hot-wire probe mounted on a traverse mechanism.

in the proximity of the wing can be determined. Thereby, the phase difference between transverse gusts and the resulting aerodynamic response of the test wing can be studied. Section 4.3 characterizes the gusting flow before encountered by the test wing. Following that, the gust response for the clean wing is discussed in Sections 5.2.1 to 5.2.4. Flow transition effects are discussed in Section 5.2.5 by comparing the gust response of the tripped wing with that of the clean wing.

5.2.1 Benchmark comparison with analytical theories

To improve the confidence of the experimental measurements, the simple but extensively-validated Küssner's linear model is utilized to predict the analytical gust response in the pre-stall regime. Küssner's unsteady aerodynamic model captures the linear lift response of a wing subjected to a sharp-edged, semi-infinite transverse gust [3]. In this formulation, the encounter with a semi-infinite gust is treated as a canonical problem in which the wing experiences a sudden and permanent change in transverse velocity as the gust front convects across it. The associated time-dependent lift development is characterized by

the Küssner's function, an indicial response function. For an arbitrary gust profile, the unsteady lift can then be determined by convolving the gust velocity history with this indicial function, thereby extending the model beyond the idealized step input to general, time-varying gusts:

$$C_{l,g}(\tau) = 2\pi \int_0^\tau \frac{d(v_g(\tau)/U_\infty)}{d\sigma} \psi(\tau - \sigma) d\sigma, \tag{5.1}$$

where $\psi(\tau)$ is the Küssner's function, $\tau = \frac{U_\infty t}{b}$ is the nondimensional time with $b = \frac{c}{2}$, and v_g is the time-varying gust data converting from the measurement point to the leading edge according to the "frozen turbulence" hypothesis. The frozen turbulence (or frozen gust) hypothesis assumes that turbulent structures or gusts are advected downstream at the mean flow velocity, allowing their temporal evolution to be interpreted as a spatial distribution when viewed in a moving reference frame. By substituting v_g into Eq. (5.1), the phase-averaged linear prediction is obtained for the transverse gust encountering with $k = 0.23$ and $\alpha_{g,max} = 7°$ at $U_\infty = 10$ m/s. It is then compared with the experimental balance outputs in Fig. 5.5. Note that, for the experimental phase-averaged results in the remainder of the study, phase alignment and uniform phase binning are applied. An initial spin-up segment is discarded, and statistics are computed from 60 consecutive cycles per condition.

Since the gust performs a nearly simple harmonic pattern, the analytical prediction employing Sears function with the same reduced frequency and amplitude as experimental ones is also included in the comparison. In general, the Sears function describes the unsteady aerodynamic lift response of an airfoil to sinusoidal transverse gusts [4]. The matching of the experimental result and analytical predictions is reasonable. It is believed that the slight curve deviation is due to two main aspects: i) phase difference: the slight variations in the u component, as depicted in Fig. 4.9(b), are not considered in the analytical model; ii) mismatch in amplitude/shape: Küssner's function is based on linear lift

aerodynamics, but nonlinearity exists for small angles well below stall due to transitional Reynolds number effects (laminar separation, resulting in nonlinear lift-curve slope) as shown in Fig. 5.1.

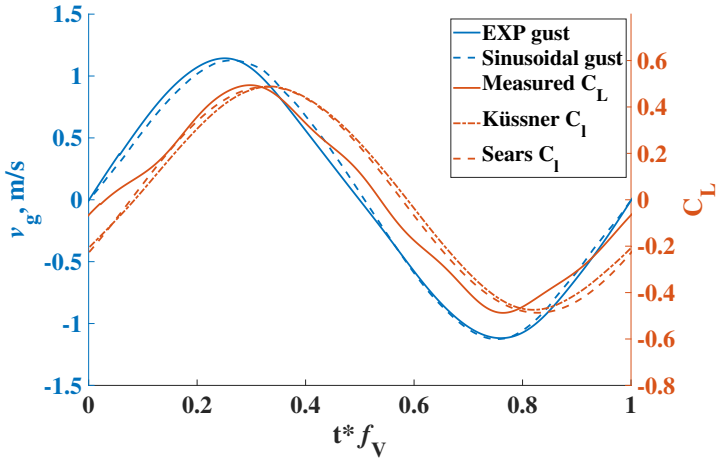

Figure 5.5: Experimental and pure sinusoidal gust profiles (left Y-axis); measured C_L and predicted C_l by Küssner's and Sears functions (right Y-axis), at $k = 0.23$, $\alpha_{g,max} = 7°$, and $U_\infty = 10$ m/s. The phase difference between the gust profiles and lift coefficients represents the response lag.

It is straightforward to define the point (local) gust angle as the incidence angle induced by the transverse component of the flow:

$$(\alpha_g)_{point} = \tan^{-1}(\frac{v_g(x,t)}{U_\infty}). \tag{5.2}$$

According to the discussions about Table 4.1 and Fig. 4.9, the transverse gusts can be considered uniform along the chord at an instant for lower k, or larger λ_g ($k < 0.1$ in Fig. 2.2). However, for transverse gusts with higher k, the definition of the gust angle of the entire wing, α_g, is ambiguous. As discussed in Ref. [17], gust effects were analogous to camber effects with the transverse gust acting as a downwash. The gust angle calculated

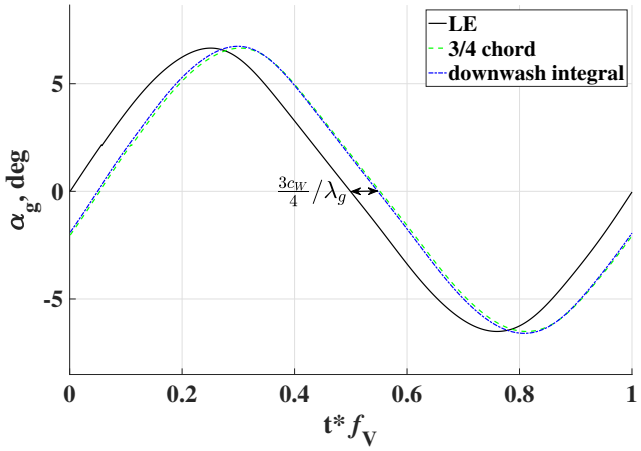

Figure 5.6: Phase-averaged α_g for different definitions, with $\alpha_0 = 0°$, transverse gust ($\alpha_{g,max} = 7°$ and $k = 0.23$) at $U_\infty = 10$ m/s. The difference between the LE curve and the other two represents $3c_W/4$ normalized by the physical gust wavelength.

through the downwash integral is defined as

$$\alpha_g(t) = \frac{1}{\pi}\int_0^\pi \frac{dY}{dX}(\cos\theta - 1)\, d\theta$$

$$= -\frac{1}{\pi}\int_0^\pi \frac{v_g(\theta,t)}{U_\infty}(\cos\theta - 1)\, d\theta, \tag{5.3}$$

where $\frac{dY}{dX}$ represents the local slope of the effective camber line induced by the gust. By assuming that the gust travels along the local streamwise flow (as per Taylor's "frozen turbulence" hypothesis) and has no pronounced amplitude dissipation along the chord of the test wing [92], the point gust angles at the leading edge and the 3/4 chord point are obtained and compared with the gust angle calculated using Eq. (5.3) in Fig. 5.6. It is observed that $(\alpha_g)_{3c/4}$ coincides with the downwash integrated gust angle, which is expected since the effective camber is derived based on thin-airfoil theory. Within the same assumption, the lift of a pitching airfoil "sees" an effective AOA as defined by the 3/4 chord point [31]. The downwash-integrated gust angle will be used for the remainder of this chapter. Considering the geometric angle of attack, α_0, the effective angle of attack of the test wing can be defined as $\boldsymbol{\alpha_e = \alpha_0 + \alpha_g}$.

5.2.2 Gust-induced dynamic stall

By adjusting α_0, the phase-averaged lift responses to the gust in pre- and post-stall regimes are compared in Fig. 5.7. As denoted by the static curve in Fig. 5.1(a), the static stall angle is around 10°. The input gust profiles for four scenarios, the phase-averaged α_g, are almost the same: nearly harmonic variation with $\alpha_{g,max} = 7°$. In Fig. 5.7(a) with $\alpha_0 = 0°$, the output lift appears to be also harmonic. It should be noted that there is a negligible phase lag between the input α_e and output C_L. Given that the phase highly depends on the conversion from temporal measurements to spatial structures utilizing the frozen gust hypothesis, a two-dimensional (2D) Large Eddy Simulations (LES) from Ref. [90] is used to examine the validity of the frozen gust hypothesis in the present setup. Although LES is inherently three-dimensional, a two-dimensional version was employed in this study, using only two grid points in the spanwise direction, for a quick cross-check with experimental results.

The numerical methods and in-house codes were validated against available experimental data in Ref. [19]. The prescribed model of the transverse gust, v_g, is a pure continuous sinusoidal profile with the same frequency and amplitude as in Fig. 5.7. In the numerical setup, the gust travels along the constant freestream velocity to conform to the frozen gust hypothesis. The computed results in Fig. 5.8 show that there is no noteworthy lag between the computed C_l response and measured C_L, which supports the validity of the frozen gust hypothesis with our setup. Given that the gust generation method inherently introduces streamwise u velocity fluctuations, which complicate the interpretation of the analysis between input gust and output response, 2D LES simulations also serve as a qualitative reference to isolate the contributions of the v component without the influence of u component fluctuations inherent in the experimental setup.

Figure 5.9 presents the spectral plots of the raw flow measurements and corresponding aerodynamic responses for $\alpha_0 = 0°$. For visual clarity, the spectral magnitudes have been

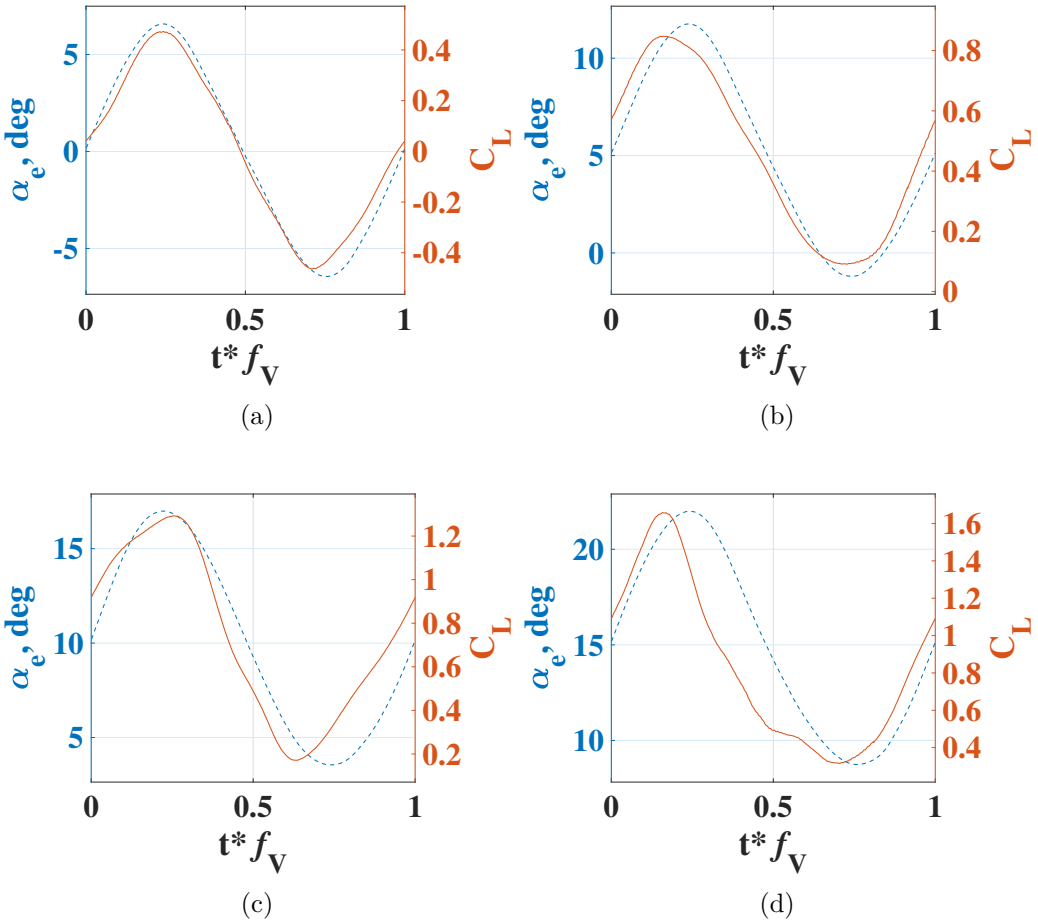

Figure 5.7: Phase-averaged lift responses of the clean wing to gust with $\alpha_{g,max} = 7°$ and $k = 0.23$ at $U_\infty = 10$ m/s in different regimes: (a) $\alpha_0 = 0°$; (b) $\alpha_0 = 5°$; (c) $\alpha_0 = 10°$; (d) $\alpha_0 = 15°$.

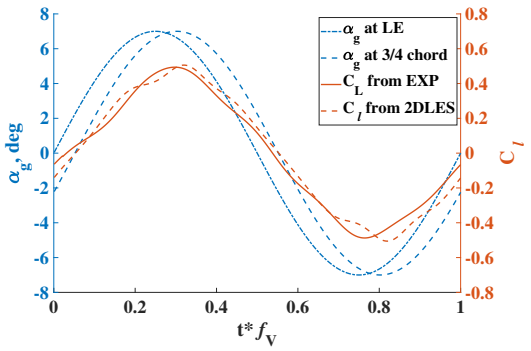

Figure 5.8: Phase-averaged time histories of gust, measured C_L, and 2D LES computed C_l (setup see Ref. [90]) for $\alpha_0 = 0°$, $\alpha_{g,max} = 7°$ and $k = 0.23$ at $U_\infty = 10$ m/s [case (a) in Fig. 5.7].

vertically offset in this and all subsequent spectral figures within this chapter. Beyond the fundamental peaks of interest (nf_V), two prominent broadband peaks centered near 28 Hz for C_D and 56 Hz for C_M are observed. These features persist across various geometric angles of attack and are present even in the absence of gust excitation. These low-frequency components are attributed to the reduced structural stiffness of the apparatus, likely stemming from the plastic interface between the load cell and the upper rod (see Section 3.3). To isolate the aerodynamic gust response from these structural artifacts, a low-pass filter with a cutoff frequency of 20 Hz has been applied to the raw data for all subsequent analysis in this chapter.

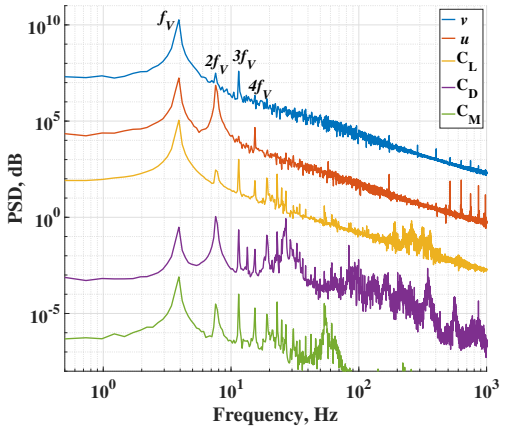

Figure 5.9: Spectra of gust and aerodynamic coefficients (raw data) for $\alpha_0 = 0°$, $\alpha_{g,max} = 7°$ and $k = 0.23$ at $U_\infty = 10$ m/s, corresponding to phase-averaged response shown in Fig. 5.7(a) for the clean wing.

Figure 5.10 compares the filtered experimental spectra with the 2D LES numerical results. Note that the low-pass filter is not applied to the numerical results; thus, the comparison indicates the filtering process successfully preserves the fundamental gust-induced harmonics (nf_V) up to $n = 5$ while removing the broadband structural noise. Note that both experimental and numerical moment coefficients (C_M and C_m, respectively) are taken about the quarter chord, and this convention is maintained throughout the remainder of the chapter. Consistent with the time-domain results in Fig. 4.5(b), the experimental u-velocity component exhibits spectral activity. In particular, the $2f_V$

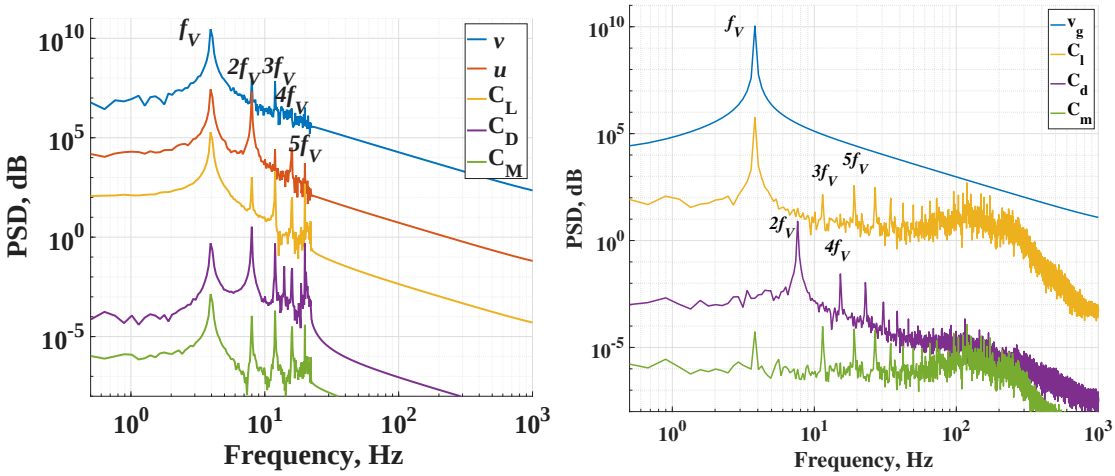

(a) (b)

Figure 5.10: Spectra of gust and aerodynamic coefficients for $\alpha_0 = 0°$, $\alpha_{g,max} = 7°$ and $k = 0.23$ at $U_\infty = 10$ m/s: (a) current experiment shown in Fig. 5.7(a), the clean wing (filtered); (b) 2D LES, setup see Ref. [90].

peak is associated with a similar peak in the drag and moment, but its effect on the lift is marginal as depicted in Fig. 5.10(a). In the CFD results, u is simply constant, and v performs a simple harmonic pattern. Due to the pure sinusoidal profile, only one primary peak is contained for v. Since the constant freestream leads to no spectral peak for the u component in the 2D LES, its spectrum is not shown in Fig. 5.10(b). Only super harmonics of odd f_V appear in the computed lift and moment spectra. The numerical simulation confirms that $2f_V$ super harmonics of measured lift and moment are owing to the variation of the u component, supporting the analysis of experiments. For drag, even f_V ($2nf_V$) peaks are observed in both the computed and experimental spectra, while odd f_V peaks are only observed in the experimental spectrum. Thus, the odd f_V peaks in the measured drag spectrum are attributed to the f_V content in the experimental u variation.

When increasing α_0 to 5° with the same gust input, the maximum α_e rises over the static stall angle, leading to an apparent phase difference between the input and output. With the test wing in the post-stall regime, Figs. 5.7(c) and (d) show an increasing phase lag between the C_L and α_e as well as a more pronounced distortion from a simple

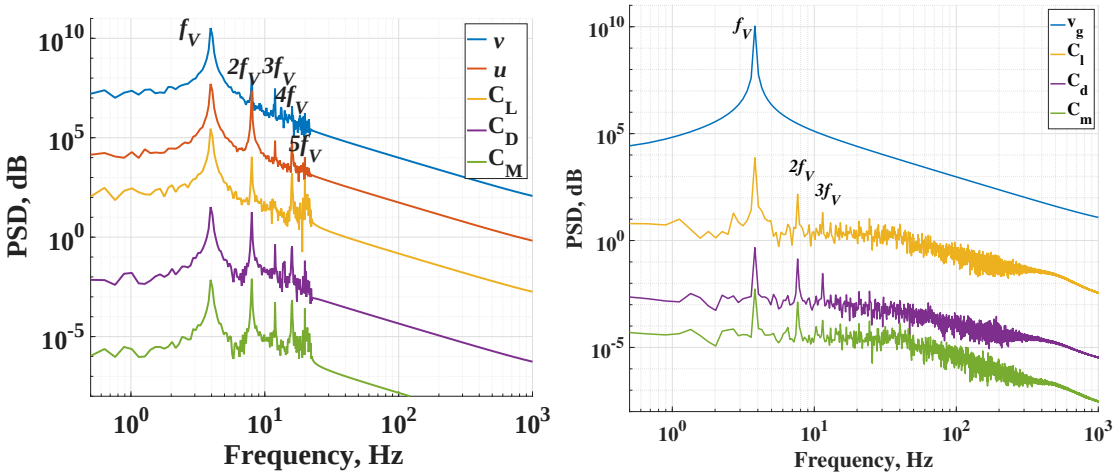

(a) (b)

Figure 5.11: Spectra of gust and aerodynamic coefficients for $\alpha_0 = 10°$, $\alpha_{g,max} = 7°$ and $k = 0.23$ at $U_\infty = 10$ m/s: (a) current experiment shown in Fig. 5.7(c), the clean wing (filtered); (b) 2D LES, setup see Ref. [90].

harmonic response. To further examine the nonlinear system, spectral densities of gust response, with $\alpha_0 = 10°$, are shown in Fig. 5.11(a). It can be seen that both u and v components hold primary peaks of f_V, while a $2f_V$ peak is comparable to the primary one for the u spectrum. In the condition with a non-zero geometric angle of attack, α_0, the experimentally observed $2f_V$ peak in the response shown in Fig. 5.11(a) might be attributed to the longitudinal component of the gust input, u, or the asymmetry of the flow caused by α_0.

To further examine whether the $2f_V$ peaks of the measured aerodynamic outputs in Fig. 5.11(a) are due to asymmetry caused by α_0 or the u variation, the 2D LES is conducted by setting α_0 to 10°, and the computed spectra are plotted in Fig. 5.11(b). As seen from the spectra for all computed aerodynamic outputs, the $2f_V$ peaks are still observed despite constant u. Especially for C_D and C_M, the powers of the $2f_V$ peaks are comparable to the primary ones. Hence, the $2f_V$ component and more generally the even harmonics in the aerodynamic response are mainly attributed to the asymmetry in the flow created by the non-zero geometric angle of attack.

Focusing back on the experiments, the gust response in the post-stall regime is compared with the static curves of the clean wing at $U_\infty = 10$ m/s by plotting the phase-averaged aerodynamic coefficients against α_e in Figs. 5.12 and 5.13 for $\alpha_0 = 10°$ and 15°, respectively. Lift enhancement and nonlinear hysteresis in both lift and moment are observed for both configurations, which are the primary characteristics of dynamic stall [44]. A steep drop in C_M occurs in Fig. 5.12(b) along with the secondary lift loop in Fig. 5.12(a). Recovery to static values is observed when α_e approaches its minimum. Increasing α_0 to 15°, as shown in Fig. 5.13, recovery to the static values does not occur for both coefficients, which suggests that full flow reattachment does not occur. In addition, a striking drop in C_L and a steep leap in C_M are noticed near the maximum α_e.

The error bars, defined using the standard deviation of all raw data at the corresponding phase point, are also marked in the phase-averaged loops in Figs. 5.12 and 5.13. At each phase point, the error bar denotes the phase-binned standard deviation across the retained cycles (variability). For reference, an approximate 95% confidence interval on the phase-binned mean is $t_{0.975,n_{\text{eff}}-1}\, SD/\sqrt{n_{\text{eff}}} \approx 0.258\, SD$, where SD is the phase-binned standard deviation and $n_{\text{eff}} = 60$ [93]. Overall, the C_L and C_M loops exhibit a smaller scale of uncertainties before lift and moment stalls ($\dot{\alpha_e} > 0$), and larger uncertainties afterwards ($\dot{\alpha_e} < 0$). These behaviors denote that there are more important nonlinearities for downwash branches ($\dot{\alpha_e} < 0$) than for the upwash branches ($\dot{\alpha_e} > 0$), which agrees with the observation in a pitch-induced dynamic stall research [94]. In Fig. 10 of Ref. [94], error bars of downstroke branches are noticeably larger than those of upstroke ones, especially for the deep stall configuration. The lower repeatability is believed to be attributed to the greater complexity of the reattachment process in the downstroke branch.

5.2.3 Effects of gust amplitude

Figs. 5.14, 5.15 and 5.16 exhibit the effects of the gust amplitude for $\alpha_0 = 5°$, 10°, 15°, respectively. Figure 5.14 shows that with α_0 in the pre-stall regime and a smaller gust

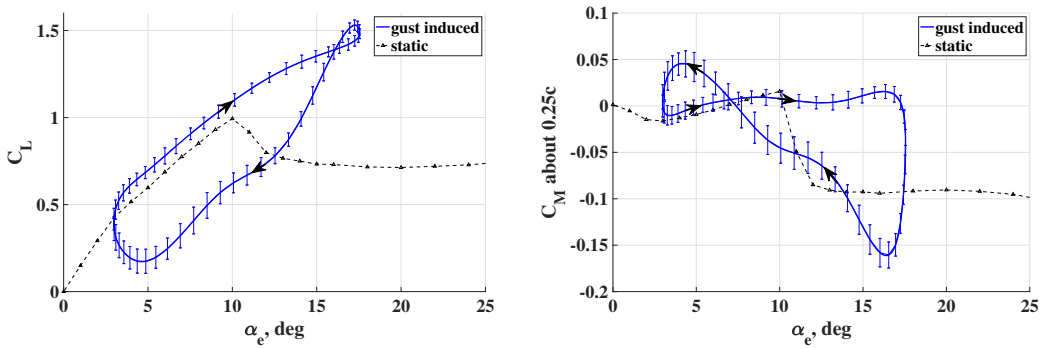

(a) (b)

Figure 5.12: Lift (a) and moment (b) coefficients against α_e of the clean wing at $\alpha_0 = 10°$, with transverse gusts ($\alpha_{g,max} = 7°$ and $k = 0.23$) at $U_\infty = 10$ m/s. Error bars are defined using the standard deviation of all raw data at the corresponding phase point.

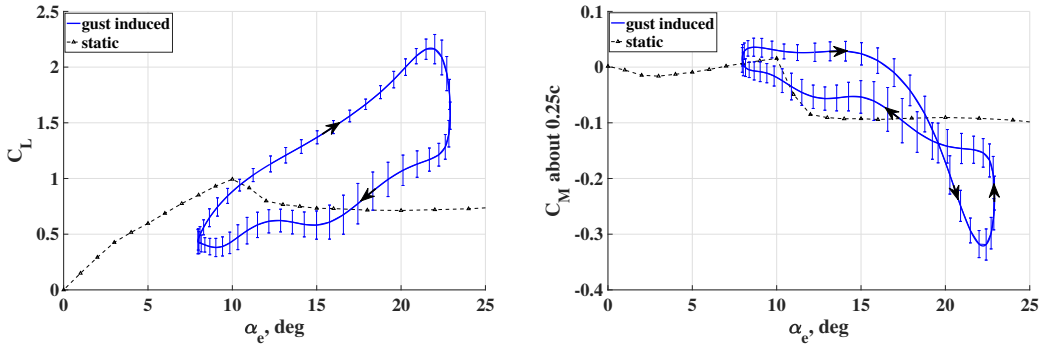

(a) (b)

Figure 5.13: Lift (a) and moment (b) coefficients against α_e of the clean wing at $\alpha_0 = 15°$, with transverse gust ($\alpha_{g,max} = 7°$ and $k = 0.23$) at $U_\infty = 10$ m/s. Error bars are defined using the standard deviation of all raw data at the corresponding phase point.

amplitude of no more than 5°, the lift loops are elliptical, denoting a linear relationship. While with $\alpha_{g,max} = 7°$, the loop is no longer elliptical due to α_e penetrating into the post-stall regime. The difference for C_M loops is more notable. For $\alpha_0 = 10°$, which is the static stall angle, the smallest gust amplitude ($\alpha_{g,max} = 1.5°$) results in an elliptical lift loop in Fig. 5.15. With increasing $\alpha_{g,max}$ to 5° and 7°, more nonlinear behaviors appear with secondary lift loops in the post-stall regime. It can be seen that the C_M loops are generally much more disturbed (non-elliptic) than the C_L loops. This has been a conclusive observation in the RMC's previous aerodynamic and aeroelastic studies [60].

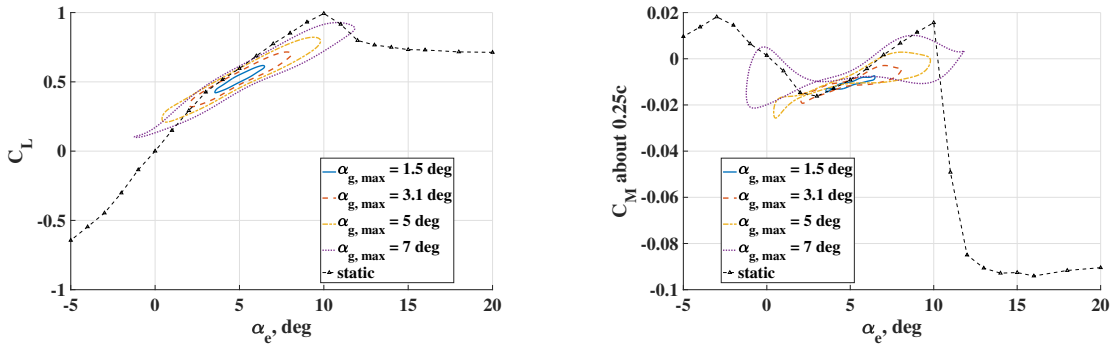

(a) (b)

Figure 5.14: Lift (a) and moment (b) coefficients against α_e of the clean wing at $\alpha_0 = 5°$, with transverse gusts of $k = 0.23$ at $U_\infty = 10$ m/s.

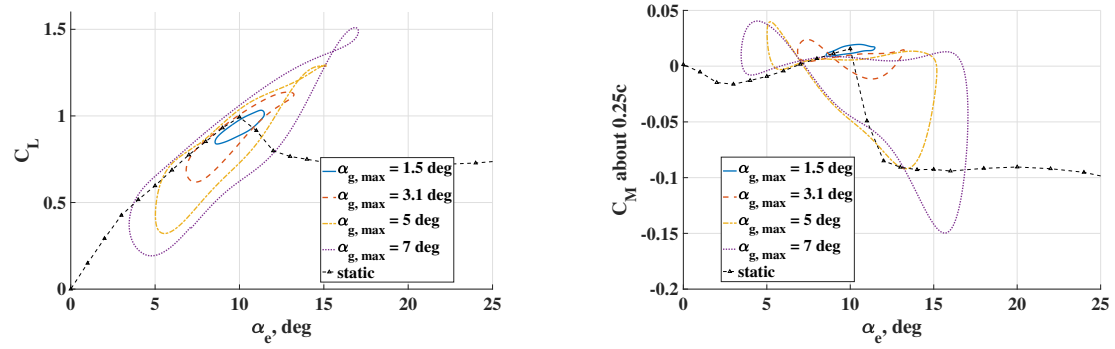

(a) (b)

Figure 5.15: Lift (a) and moment (b) coefficients against α_e of the clean wing at $\alpha_0 = 10°$, with transverse gusts of $k = 0.23$ at $U_\infty = 10$ m/s.

In the post-stall regime with $\alpha_0 = 15°$ in Fig. 5.16, the aerodynamic system also unexpectedly behaves nearly linearly with smaller gust amplitudes: the loop patterns for

both C_L and C_M are roughly elliptical. While with larger $\alpha_{g,max}$, especially with those driving α_e penetrating into the pre-stall regime, the loops lose symmetry: the differences in loop patterns between $\alpha_{g,max} = 7°$ and $\alpha_{g,max} = 5°$ are pronounced, indicating significant variations in aerodynamic response.

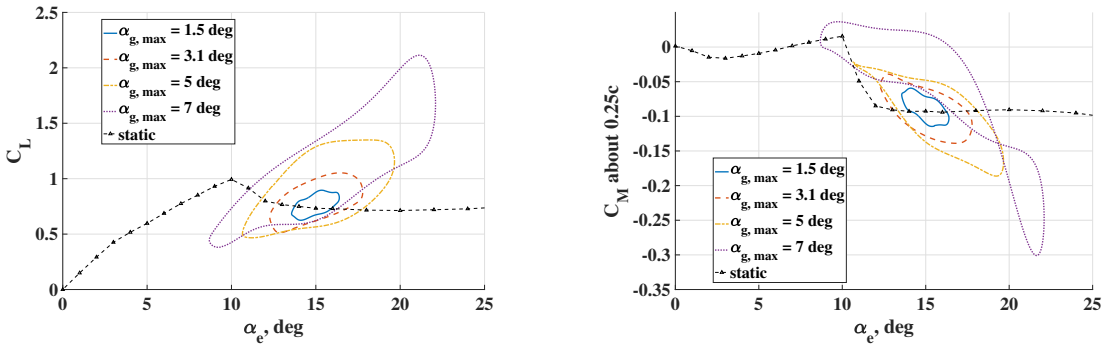

(a) (b)

Figure 5.16: Lift (a) and moment (b) coefficients against α_e of the clean wing at $\alpha_0 = 15°$, with transverse gusts of $k = 0.23$ at $U_\infty = 10$ m/s.

A brief comparison is made to situate the present loops relative to a similar study conducted by Wang *et al.* [38], who investigated a harmonic transverse gust with an amplitude of 3° in a water tunnel. In the pre-stall regime with $\alpha_g = 3.1°$ in Fig. 5.14 of the present study, the magnitude of the C_L-loop values (around 0.4) is similar to their pre-stall case (green curve in Fig. 23 of Ref. [38]). In the deep-stall regime with $\alpha_g = 3.1°$ in Fig. 5.16 of the present study, the loop magnitude (around 0.6) also resembles their high-α_0 case (blue curve in Fig. 23 of Ref. [38]). Differences in the loop shape are expected since α_g is not identically defined: a local leading-edge gust angle, represented by Eq. (5.2) of the present work, was employed in their research. The different definitions of α_g directly affect the phase and thereby alter the loop shape.

5.2.4 Effects of Reynolds numbers

Figure 5.17 shows the Reynolds number effects on the gust-induced dynamic stall. The three Reynolds numbers correspond to $U_\infty = 5$, 10, and 15 m/s. To ensure the same

reduced frequency for the three scenarios, 1 Hz, 2 Hz, and 3 Hz f_V are employed, respectively, resulting in $k = 0.12$. By adjusting the vane amplitude, the three scenarios have a similar gust amplitude of around 4.5° and thus a close α_e range. In general, the three scenarios exhibit similar loops for both lift and moment. Relative to Re_c = 63,000 and 190,000, the Re_c = 126,000 loop shows a reduced magnitude of variation in C_M, which is due to its gust amplitude being smaller than the other two. It is inferred that the Reynolds number effects on the loop patterns of both coefficients are not significant. This observation agrees well with the finding for the pitch-induced dynamic stall in Ref. [44], where "the Reynolds number effect is the least dramatic of all parameters studied" was described.

Note that the preceding inference applies to Reynolds numbers of comparable order. Large changes in Re can indirectly influence gust-induced dynamic stall by altering the baseline (no-gust) aerodynamics, e.g., lift/moment slopes and the static stall angle, which, in turn, reshape the loops. In addition, within the Reynolds numbers tested, the freestream Mach number is low ($M_\infty \approx 0.015$–0.044) and compressibility effects are negligible. However, at sufficiently high Mach numbers where compressibility becomes significant (e.g., $M_\infty \gtrsim 0.2$), modifications to the dynamic-stall behavior are expected, as documented for pitch-induced dynamic stall by Carr *et al.* [47]. This regime lies beyond the scope of the present study.

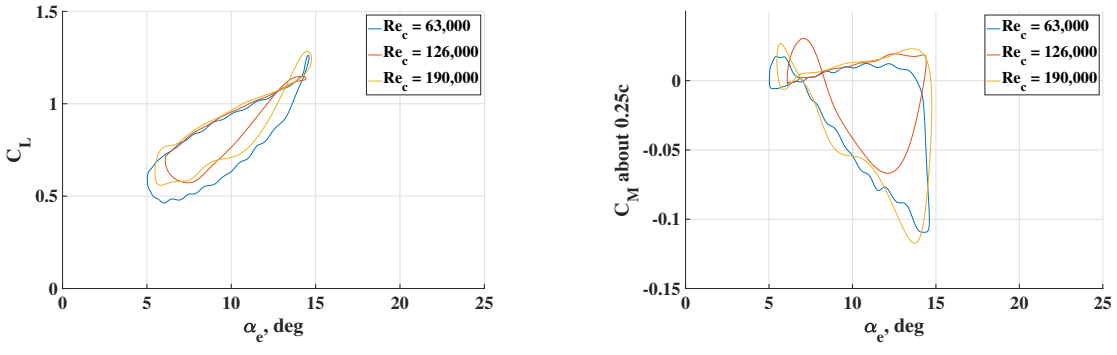

(a) (b)

Figure 5.17: Lift (a) and moment (b) coefficients against α_e of the clean wing at $\alpha_0 = 10°$, with $k = 0.12$ and $\alpha_{g,max}$ around 4.5° at various Reynolds numbers.

5.2.5 Effects of flow transition

As discussed in Section 5.1, the flow transition has some effects on the aerodynamic behavior under uniform flow. The effects of transition tripping on gust response are discussed in this section. Two geometric AOAs are considered: $\alpha_0 = 10°$ and 15°. Figure 5.18 shows the gust response comparison between the clean wing and tripped wing for a smaller gust amplitude, $\alpha_{g,max} = 3.5°$. It can be seen that the flow transition does not show significant effects for $\alpha_0 = 15°$. This is believed to be attributed to α_e varying only within the post-stall regime with the smaller gust amplitude. For $\alpha_0 = 10°$, the transverse gust causes α_e to oscillate between the pre- and post-stall regimes. The distinction is more apparent for C_M loops between the tripped and clean wings.

Increasing $\alpha_{g,max}$ to 7° as shown in Fig. 5.19, the secondary lift loop disappears with the tripped wing for $\alpha_0 = 10°$. In addition, the C_M drop is less steep for α_e near its maximum, and the recovery process to the static value also behaves more gently for α_e near its minimum, compared with the clean wing. For $\alpha_0 = 15°$ with the clean wing, $\alpha_{g,max}$ = 7° drives α_e in penetrating into the pre-stall regime, thus causing the loop patterns to differ from those of smaller $\alpha_{g,max}$, as shown in Fig. 5.16. After applying the transition strip, the transverse gust with $\alpha_{g,max} = 7°$ maintains similar elliptical-like loop patterns for both coefficients with those of smaller $\alpha_{g,max}$ in Fig. 5.16 for the clean wing, indicating an extended local linearity. For both $\alpha_0 = 10°$ and 15°, it is suggested that the transition strip changes the vortex shedding and boundary reattachment process, particularly when the gust drives the flow crossing the pre- and post-stall regimes. When the α_e variation remains within the post-stall regime, the tripping effects are not remarkable.

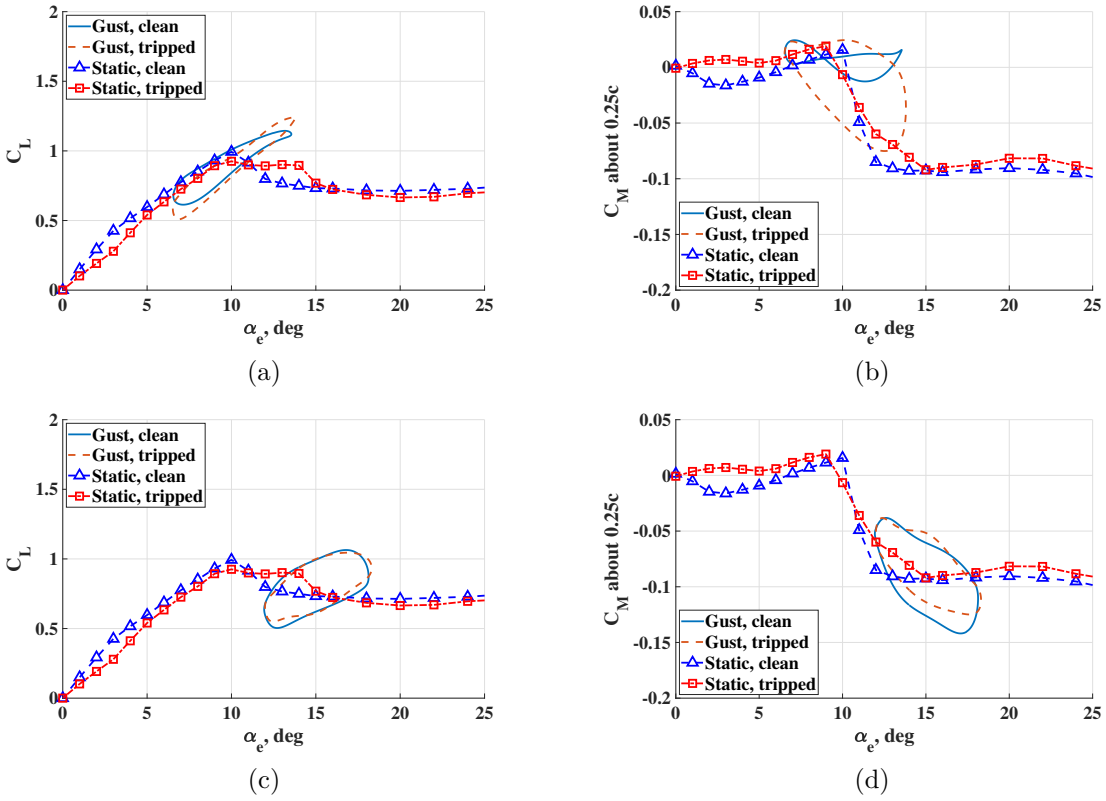

Figure 5.18: Lift and moment coefficients against α_e, $\alpha_0 = 10°$ (a-b); $\alpha_0 = 15°$ (c-d), with transverse gusts ($\alpha_{g,max} = 3.5°$ and $k = 0.23$) at $U_\infty = 10$ m/s.

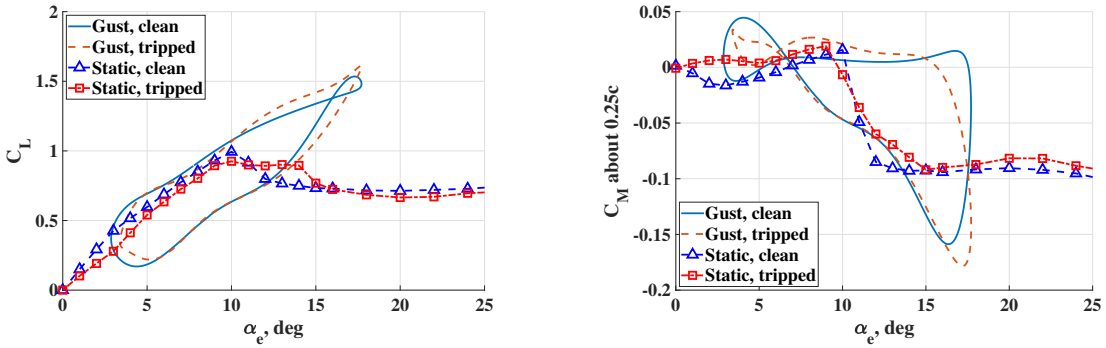

(a) (b)

(c) (d)

Figure 5.19: Lift and moment coefficients against α_e, $\alpha_0 = 10°$ (a-b); $\alpha_0 = 15°$ (c-d), with transverse gusts ($\alpha_{g,max} = 7°$ and $k = 0.23$) at $U_\infty = 10$ m/s.

5.3 Analogy Between Gust- and Pitch-Induced Dynamic Stalls

In light of the classical pitch-induced dynamic stall problem, theoretical considerations can be expressed. In several aspects, pitch- and gust-induced stalls are analogous. In Refs. [43], [44], dynamic stall phenomena were investigated by employing a pitching wing with varying reduced frequencies. Due to the lack of calibration for the operational amplifier system, the absolute values of aerodynamic coefficients were not assigned [43], as shown in Fig. 5.20. Therefore, only relative comparisons are possible. With reduced frequencies varying from $k = 0.15$ to 0.25, delayed shedding of the primary vortex resulted in the formation of a secondary lift loop [44].

In the present study, at $\alpha_0 = 10°$ (Fig. 5.12) with $k = 0.23$, the aerodynamic hysteresis loops are similar to those reported for the pitch-induced dynamic stall in Ref. [44], as shown in Fig. 5.20 with $k = 0.25$. Both their and our cases are dynamic stalls induced by α_e varying around the corresponding static stall angles, crossing the pre- and post-stall regimes. These similar aerodynamic responses suggest an analogy between gust- and pitch-induced dynamic stalls. Moreover, compared with another study of pitch-induced dynamic stall [94], the branch-wise distribution of uncertainties also exhibits an analogous trend: in both cases, the upstroke (pitch-induced) or upwash (gust-induced) branch exhibits comparatively low uncertainty, whereas the downstroke (pitch-induced) or downwash (gust-induced) branch shows significantly higher uncertainty. This parallel behavior in the uncertainty characteristics supports the proposed analogy, namely that the upwash and downwash phases of gust-induced stall are closely related to the upstroke and downstroke phases of pitch-induced stall, respectively.

Revisiting the previously discussed results from the perspective of an analogy between the two types of dynamic stalls, some speculations can be made. A secondary lift loop is observed in Fig. 5.12(a). The presence of the secondary loop suggests delayed shedding

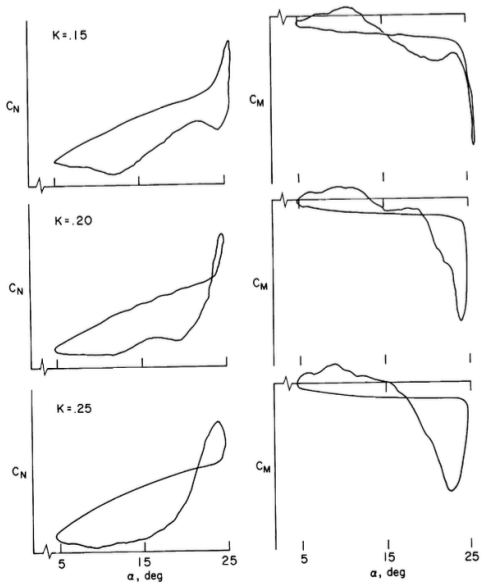

Figure 5.20: Normal force and pitching moment with pitch profile $\alpha = 15° + 10°\sin\omega t$, $Re_c = 2.5 \times 10^6$, k varied from 0.15 to 0.25, adopted from Ref. [44] (NASA report in public domain).

of a primary vortex near the maximum α_e. Figure 5.15(a) demonstrates the gradual emergence of secondary lift loops as α_g increases. This implies that there exists a critical gust amplitude to induce the vortex shedding delay at this reduced frequency.

For a given airfoil geometry, the Reynolds number plays a secondary role in both gust- and pitch-induced dynamic stalls, while the reduced frequency was identified as the most significant parameter affecting dynamic stall behavior [44]. However, in the present experimental configuration, gust amplitude is inherently coupled with reduced frequency at a fixed airspeed. Consequently, varying k simultaneously affects $\alpha_{g,max}$ at a constant U_∞, making it experimentally challenging to isolate the effects of reduced frequency. These effects on gust-induced dynamic stall can be investigated through ongoing numerical simulations. Furthermore, beyond the qualitative comparison presented in this study, a quantitative comparison of the two dynamic stall mechanisms will be conducted using numerical simulations. These simulations employ matched configurations differing only in the forcing mechanism, transverse gusts versus pitching motion, enabling more detailed discussions of the underlying flow physics.

5.4 Analogy Analysis Using Numerical Simulations

5.4.1 Two-dimensional simulations

In the absence of flow visualization in the present experiments, the flowfield of gust-induced dynamic stall cannot be directly observed. Consequently, the 2D LES results, previously used to isolate the effects of the fluctuating u component, were employed to provide physical insight into the observed phenomena. The numerical study utilized INSflow, an in-house solver developed by the National Research Council Canada. The computational domain replicates the dimensions of the wind tunnel test section used in this study. The 2D mesh comprises two blocks, each containing 385×97 grid points (Fig. 5.21), with a first-cell wall distance of 3×10^{-5} to ensure an estimated $y^+ \approx 1$. Comprehensive details regarding the numerical setup and gust modeling are provided in Refs. [19] and [90]. The grid sensitivity study has been conducted and will be reported in a future study focusing on the numerical study of the gust-induced dynamic stall.

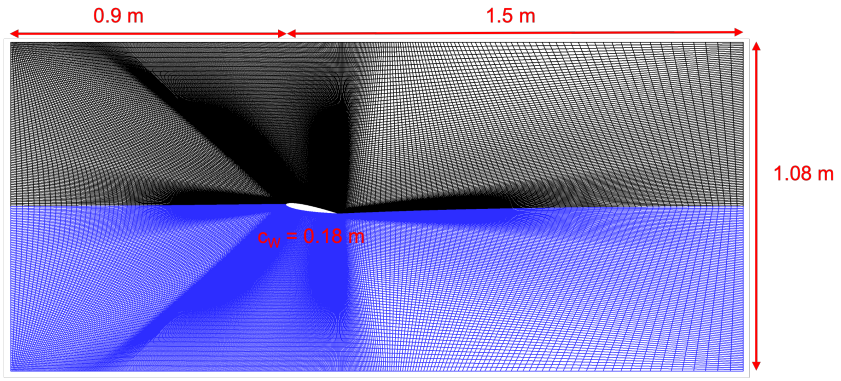

Figure 5.21: Two-dimensional cross-section of the computational mesh for the NACA0012 test wing.

Validation of the numerical results was performed by comparing them with experimental data, as shown in Fig. 5.22. The magnitude of computed lift and moment coefficients is in agreement with the measurements, capturing the fundamental processes of dynamic stall, including lift enhancement and hysteresis in both C_L and C_M. However, the 2D

simulations do not exhibit the secondary lift loop and predict an earlier moment stall followed by a secondary moment loop.

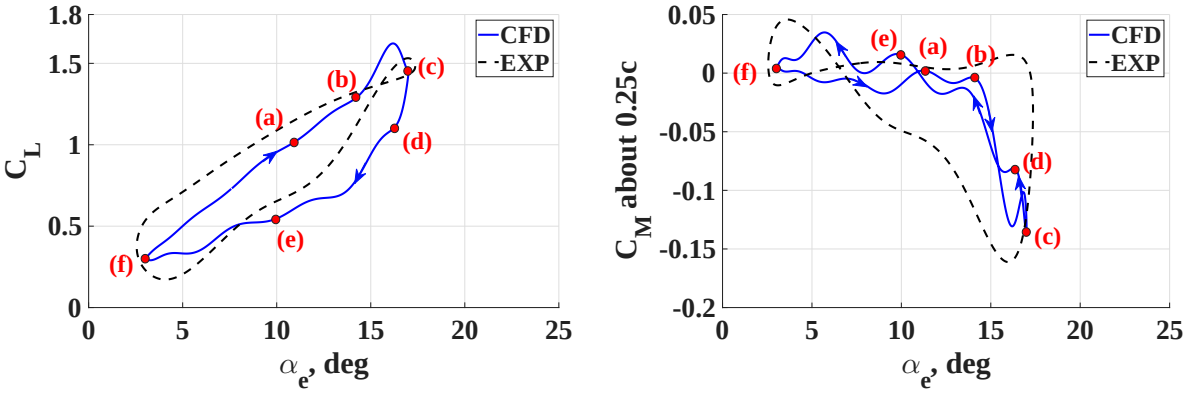

Figure 5.22: 2D LES computed (a) lift and (b) moment coefficients against α_e at $\alpha_0 = 10°$, with transverse gusts ($\alpha_{g,max} = 7°$, $k = 0.23$) at $U_\infty = 10$ m/s. The vorticity structures for marked events are displayed in Fig. 5.23.

Compared with the loop patterns documented in Carr *et al.*'s study on pitch-induced dynamic stall [44], the computed gust-induced loop pattern ($k = 0.23$) is remarkably similar to the results for a pitching NACA0012 wing at a lower reduced frequency of $k = 0.15$ (see top plots of Fig. 5.20). This similarity suggests that the gust-induced dynamic stall may be governed by a similar vortex-dominated process as that observed in pitching motions, despite the difference in nominal reduced frequencies. Consequently, the 2D LES framework provides a valuable platform for investigating the general analogy between these two stall mechanisms by facilitating a direct comparison of the underlying flow structures and their temporal evolution.

The computed results exhibit representative events of the dynamic stall process that align closely with those observed in pitch-induced stall at $k = 0.15$ (top plots of Fig. 5.20). Figure 5.23 summarizes the phase-averaged (over eight periods) normalized vorticity (ω_z) fields during the gust encounter. Streamlines upstream of the airfoil visualize the instantaneous gust angle. These are compared with the experimental sketches for pitch-induced stall presented in Ref. [44]. By correlating the measured loop trends in Fig. 5.22 with the

computed flowfield in Fig. 5.23, the following sequence of events is identified:

a) **Stall inception:** The effective angle of attack exceeds the static stall angle; boundary layer eddies begin to form.

b) **Vortex initiation:** The primary vortex begins to shed, coinciding with the onset of moment stall.

c) **Lift peak and shedding:** The vortex detaches from the upper surface, resulting in lift stall and the minimum pitching moment.

d) **Full stall:** Deep stall is reached as the lift drop slope flattens.

e) **Recovery:** The boundary layer begins re-attaching from the leading edge toward the trailing edge.

f) **Return to attached flow:** Reattachment is completed, and aerodynamic coefficients return to their unstalled values.

The high degree of similarity between the phenomena observed for a pitching wing in uniform flow and a stationary wing in a transverse gust strongly supports the proposed analogy. It should be noted that while the numerical simulations use $k = 0.23$ (matching the current experiment), the 2D loop behavior resembles the lower-frequency $k = 0.15$ pitch case from literature. This discrepancy is mainly attributed to the inability of the 2D LES to fully capture the 3D mechanisms responsible for the delayed shedding of the primary vortex. In addition, this regime appears sensitive to subtle differences in the setup—for example, the computational simulations impose a strictly constant streamwise component u, whereas the experiments exhibit slight fluctuations in u.

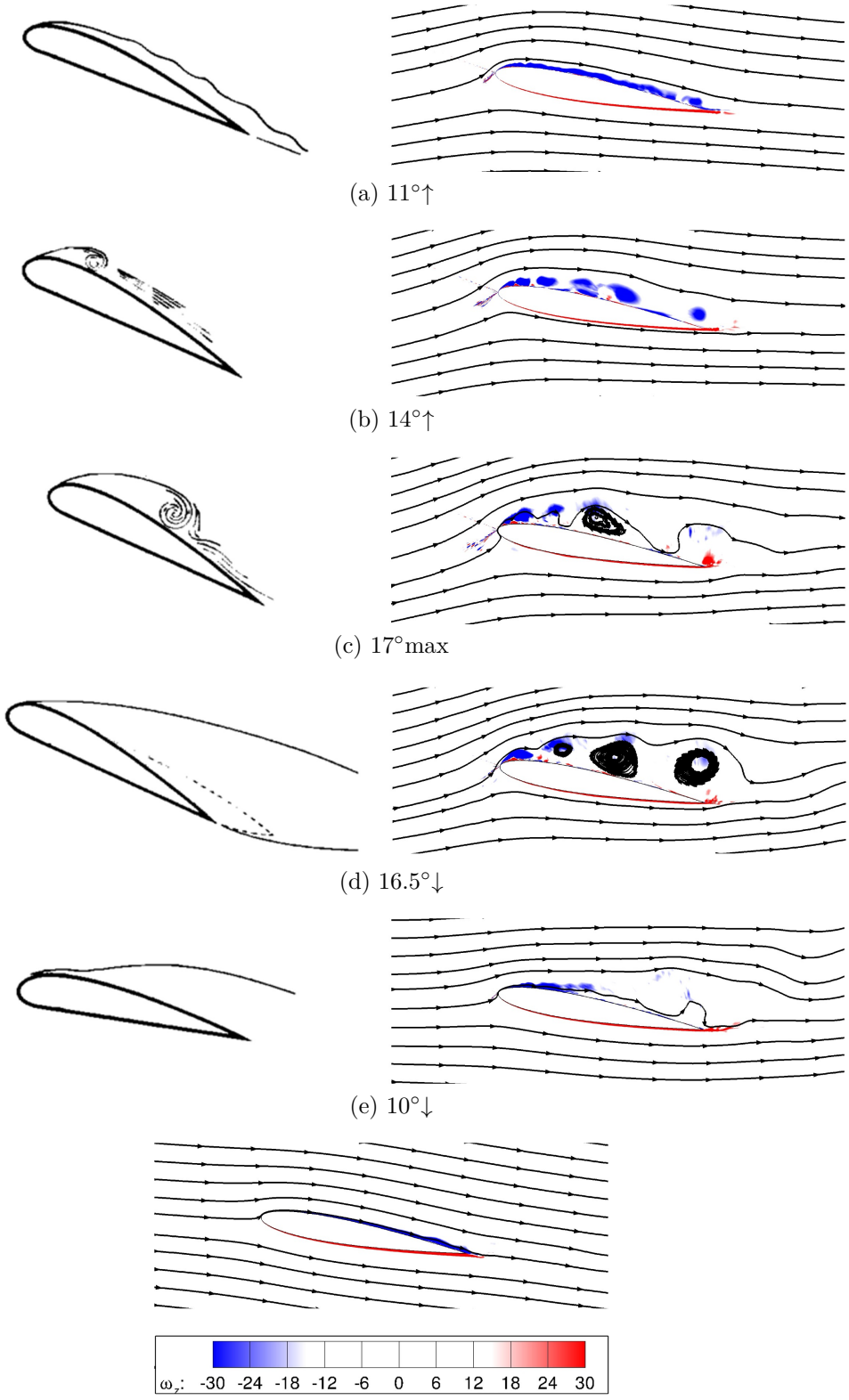

(a) 11°↑

(b) 14°↑

(c) 17°max

(d) 16.5°↓

(e) 10°↓

(f) 3°min

Figure 5.23: Flow structure comparison between left: experimental pitch-induced dynamic stall ($k = 0.15$) from Ref. [44] (public domain)) and right: 2D LES computed gust-induced dynamic stall ($k = 0.23$). The evolution of the upstream streamlines from (a) to (f) visualizes the gust traveling through the airfoil.

5.4.2 Three-dimensional simulations

To improve the fidelity of the numerical results, 3D LES were conducted by uniformly extending the computational domain in the spanwise direction by 1/6 of the chord length. Previous work by Visbal *et al.* (2017) [48] indicated that span-to-chord ratios from 0.1 to 1.0 yield marginal differences in dynamic stall characteristics. Spanwise extent of s/c = 0.1 and 0.05 were used for pitch-induced dynamic stall studies in Ref. [48] and their follow-up work [49], respectively. The 3D domain consists of two blocks with $513 \times 129 \times 49$ nodes for each block. The 49 nodes are distributed uniformly in the spanwise direction. Crucially, the 3D LES successfully captures the secondary lift loop, as shown in Fig. 5.24, yielding peak values and loop patterns that closely match the experimental data. The corresponding phase-averaged spanwise vorticity contours are displayed in Fig. 5.25.

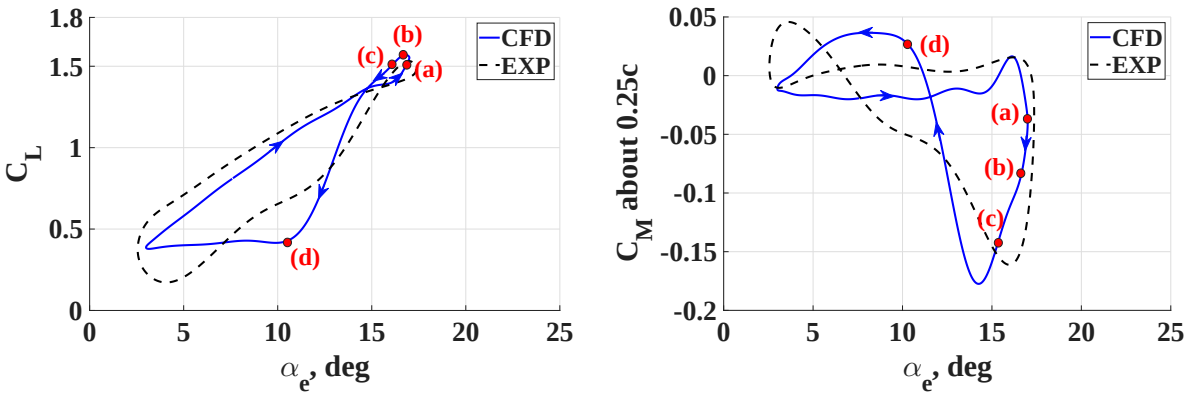

Figure 5.24: 3D LES computed (a) lift and (b) moment coefficients against α_e at $\alpha_0 = 10°$, with transverse gusts ($\alpha_{g,max} = 7°$, $k = 0.23$) at $U_\infty = 10$ m/s.

Figure 5.25(a) illustrates the ω_z field at maximum α_e. A LEV forms and continues to grow even as after α_e reaches its turning point (local maximum) and enters the descending branch in Fig. 5.25(b). The LEV remains attached to the upper surface around this phase point, driving the lift to its peak value while simultaneously causing a sharp drop in the pitching moment. As α_e continues to decrease to around 16°, the LEV sheds from the surface in Fig. 5.25(c). When α_e decreases to 10°, a clockwise roll-up near the trailing

edge induces a trailing-edge vortex (TEV) in the opposite direction. The flattening of the lift slope in Fig. 5.25(d) indicates that the airfoil has entered full stall, with a flow structure resembling a static stall condition.

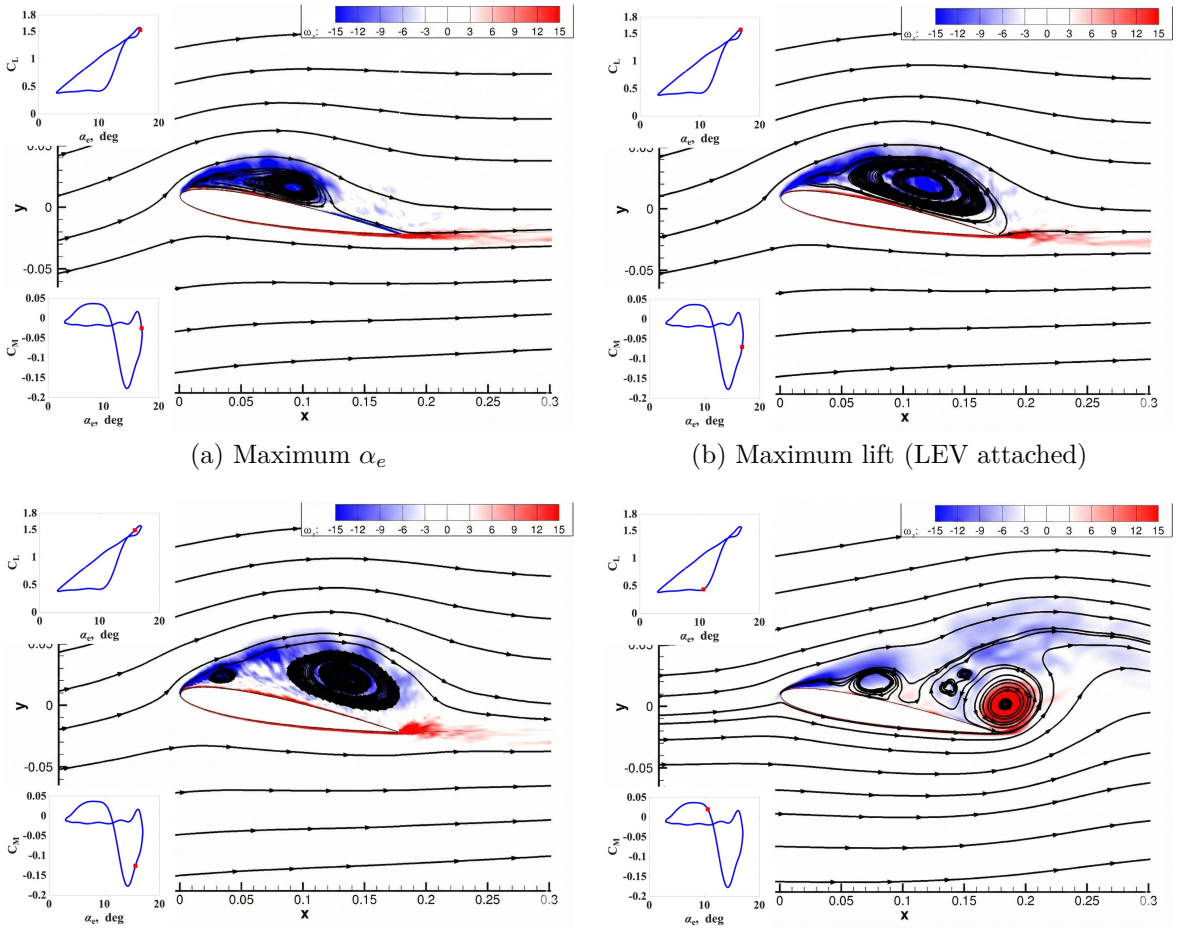

(a) Maximum α_e (b) Maximum lift (LEV attached)

(c) LEV detached (d) Full stall

Figure 5.25: 3D LES phase-averaged vorticity fields ($\alpha_0 = 10°$, $\alpha_{g,max} = 7°$, $k = 0.23$). Phase points correspond to the markers in Fig. 5.24.

To validate the simulated flow field, the contours were compared with PIV data from Refs. [38] and [56]. These studies investigated stationary NACA0012 wings encountering periodic transverse gusts in water tunnels at $Re = 2 \times 10^4$ and reduced frequencies of 0.2 and 0.3 for Refs. [38] and [56], respectively. The computed vorticity field matches the measured spanwise vorticity at the phase of maximum lift in Fig. 21(b) from Ref. [38]. Similarly, the computed full stall state (Fig. 5.25(d)) aligns with the experimental mea-

surements in Fig. 16(b.iv) from Ref. [56], both featuring the formation of counterclockwise TEV. These comparisons validate the 3D LES approach and confirm the reliability of the numerical interpretation.

Ongoing work focuses on a rigorous quantitative comparison between two numerical configurations: (i) a stationary airfoil in a harmonic transverse gust and (ii) a harmonically pitching airfoil in uniform flow. Equivalence is enforced by matching the effective AOA history, $\alpha_{e,\mathrm{gust}}(t) = \alpha_0 + \alpha_g(t)$, with the pitching law, $\alpha_{\mathrm{pitch}}(t) = \alpha_{e,\mathrm{gust}}(t)$, while keeping geometry, Re, and k identical. This quantitative analysis will further elucidate the underlying flow physics and will be the subject of a forthcoming publication.

Chapter 6

STALL FLUTTER FORCED BY TRANSVERSE GUSTS

Stall flutter is widely understood to arise from dynamic stall physics during free pitch oscillations that traverse pre- and post-stall regimes. The preceding chapter demonstrated that transverse gusts can also induce dynamic stall. These observations motivated a focused investigation of how transverse gusts interact with stall flutter. In addition, since self-sustained stall flutter provides a repeatable LCO, it provides a convenient testbed for probing how gust excitation affects dynamic-stall dynamics associated with pitching oscillations. In this setting, a "competition" between two frequencies emerges: the intrinsic frequency of the stall flutter LCO and the extrinsic frequency of the harmonic gust. The following sections detail the experimental and analytical exploration of this interaction.

6.1 Aeroelastic Findings Under Uniform Flow

The flutter rig used to study aeroelastic response to gusts is shown in Fig. 3.10. The elastic axis (EA) is located at 35% chord from the leading edge. The chord Reynolds number is in the range of (6.2–10.3)$\times 10^4$ in the present and the next chapters. The structural stiffness in pitch (k_θ) is 0.3 Nm/rad. The mass moment of inertia (I_θ) of the wing about its EA (i.e. all the rotating parts) is 0.0011 kg $\cdot$ m^2. The damping coefficient

is calculated to be 0.0015 N · ms/rad, based on free decay tests in quiescent air. More details of this apparatus are referred to Section 3.4. In a previous study with constrained heave [60], depending on factors like Reynolds number and initial disturbance, the system was attracted to different states, including equilibrium after decay, small-amplitude oscillation (SAO) indicating LSF, and large-amplitude oscillation (LAO) indicating SF. The SAO amplitude was observed around 5°, well below the stall angle. To simplify the gusting aeroelastic problem and eliminate the boundary layer transition effects in this study, a sandpaper strip is mounted to the leading edge of the aeroelastic wing, as shown in Fig. 6.1. By promoting an earlier transition to a more turbulent boundary layer, this trip suppresses the LSF branch so that the experiments focus on the stall flutter response to transverse gust excitation.

Figure 6.1: Combination of the gust generator and the flutter rig.

Prior to gust response, Fig. 6.2 summarizes the response of the pitch-only flutter rig in a steady uniform freestream. Note that this is a particular type of stall flutter as the LCOs are symmetric about the zero pitch angle. The onset speed of stall flutter is $U_{\mathrm{SF,onset}} = 6$ m/s (Re $\approx 6.2 \times 10^4$), and the analytical divergence (static loss-of-equilibrium, see [60] for more details) speed is $U_D = 7.5$ m/s (Re $\approx 7.7 \times 10^4$), see

Fig. 6.2(a). For $U_\infty < U_{\mathrm{SF,onset}}$, small perturbations decay to the zero-equilibrium state. For $U_{\mathrm{SF,onset}} < U_\infty < U_D$, two stable attractors coexist (two solid-line branches), i.e., sufficiently large initial disturbances lead to stall flutter exhibiting LAO; whereas small perturbations still return to zero equilibrium. When $U_\infty > U_D$, stall flutter is self-triggered without external perturbations, and the baseline amplitude, $\bar{\theta}_0$, approaches a plateau of $\sim 41^\circ$ near $U_\infty = 10$ m/s ($\mathrm{Re} \approx 10.3 \times 10^4$). This amplitude plateau of stall flutter was also observed by [95] at a similar level.

Figure 6.2(b) shows the frequency evolution. The structural natural frequency f_n is measured in quiescent air. The flutter frequency in the no-gust case, $f_{\theta,0}$, increases approximately linearly with U_∞. Since f_n is fixed while the effective aerodynamic stiffness grows with dynamic pressure, the rise of $f_{\theta,0}$ with U_∞ reflects the coupled structural–aerodynamic stiffness.

6.2 Gust-Induced Lock-In During Stall Flutter

As depicted in Fig. 6.3, gust effects are examined on an aeroelastic wing by combining the flutter rig and the gust generator. The measurements of the vane oscillation and the pitch angle are conducted simultaneously using a 16-channel Data Acquisition (DAQ) module NI-9202 from National Instruments. Considering that both the upstream oscillating vanes and the downstream fluttering wing alter the local flow field, the in-situ gust profile used for the gusting aeroelastic study cannot be measured directly. Therefore, the gust amplitude measurements in an empty test section are used, without the wing installed. The gust frequency is determined by measuring the vane frequency. Unless otherwise noted, the vane's harmonic pitch amplitude is fixed at 12° for most of the experiments reported here. Because the vane amplitude is held fixed while the gust frequency f_g is varied, the gust angle is frequency-dependent (see Figs. 4.9 and 4.10) and thus is not strictly constant across a frequency sweep. For reference, the gust angle ranges from

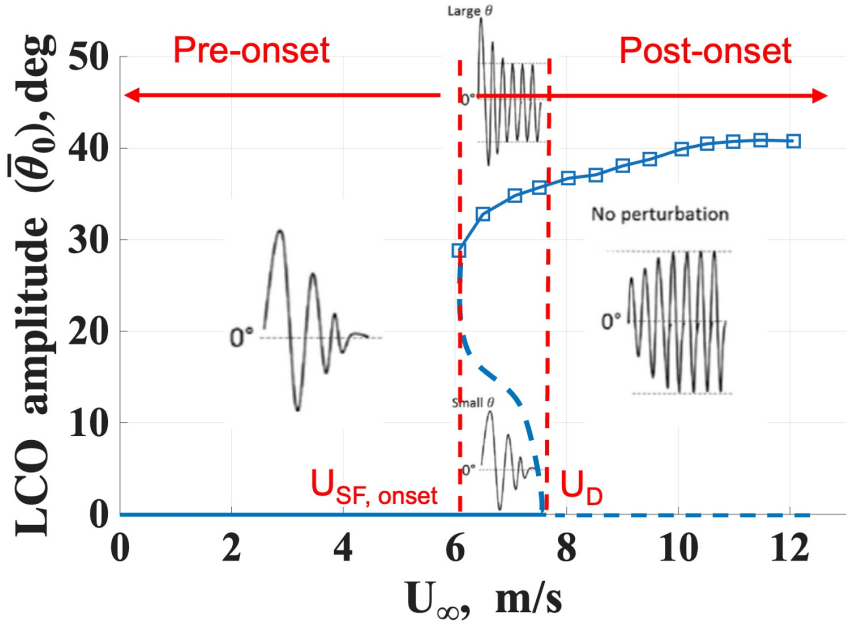

(a)

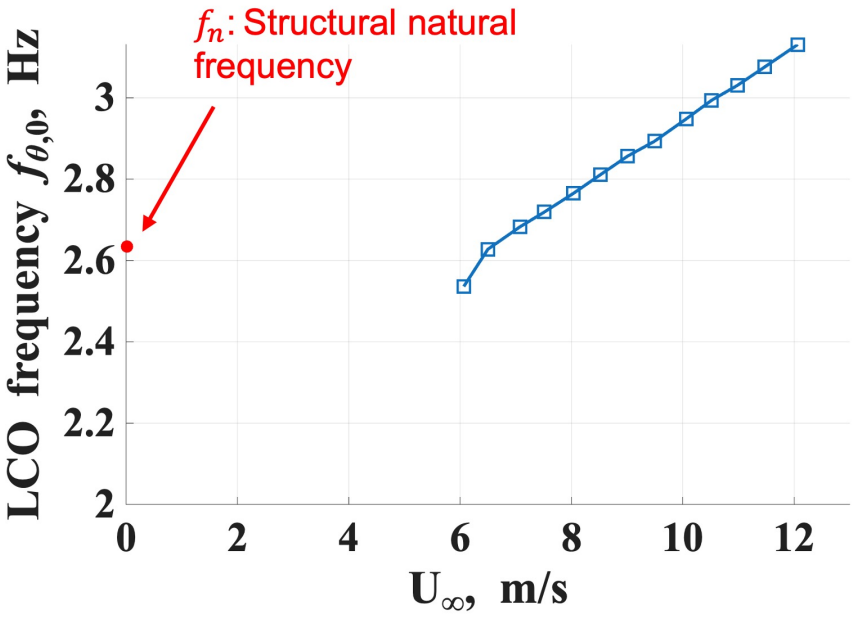

(b)

Figure 6.2: Schematic of (a) bifurcation diagram with attractors observed within each subrange of airspeeds tested; (b) flutter frequency trend against airspeed, under uniform freestream (no gust) condition. The corresponding chord Reynolds number is in the range of $(6.2–10.3)\times10^4$.

around 6° to 7° as the vane frequency increases from 2 Hz to 3 Hz at $U_\infty = 7$ m/s. Consequently, regime trends versus frequency sweep reflect the effect of f_g primarily, with a secondary co-variation of gust excitation level. The influence of the excitation level is examined explicitly with separate runs at a reduced vane amplitude of 6° ($\alpha_{g,max} \approx 3°$), which will be discussed later.

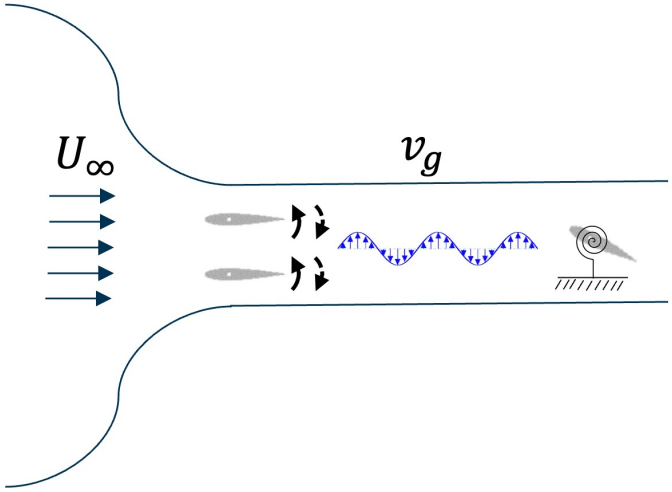

Figure 6.3: Sketch of an aeroelastic wing with a large incidence angle encountering transverse gusts generated by the upstream gust generator.

To avoid the uncertainties near the inception of dynamic instability, the gust effects on stall flutter are investigated at U_∞ varying from 7 to 10 m/s (Re $\approx (7.2 - 10.3) \times 10^4$), larger than $U_{SF,onset}$. At $U_\infty = 7$ m/s, the oscillation frequency with no gust, $f_{\theta,0}$, is measured at 2.65 Hz, as shown in Fig. 6.2(b). By performing a sweep of the gust frequency at this airspeed, several key aeroelastic phenomena are observed, as summarized in Fig. 6.4. Gust-induced amplitude modulation and lock-in attracted significant interest. In general, amplitude modulation occurs when two signals with slightly different frequencies interfere, producing a periodic variation in amplitude and forming modulation envelopes, known as a *beat*. Thus, this amplitude modulation phenomenon is also called beating. By contrast, lock-in describes the synchronization of two frequencies of oscillating systems due to coupling or interaction. Once synchronized, or locked, within a finite band, the systems oscillate at the same frequency, even if their original frequencies differed. This lock-in

band is widely called the *synchronization window/zone*, or, more recently, the *Arnold tongue* (after V. I. Arnold) for both externally forced and parametrically excited systems [73]. The term *entrainment* is also used, but especially for externally forced frequency locking [73], [96].

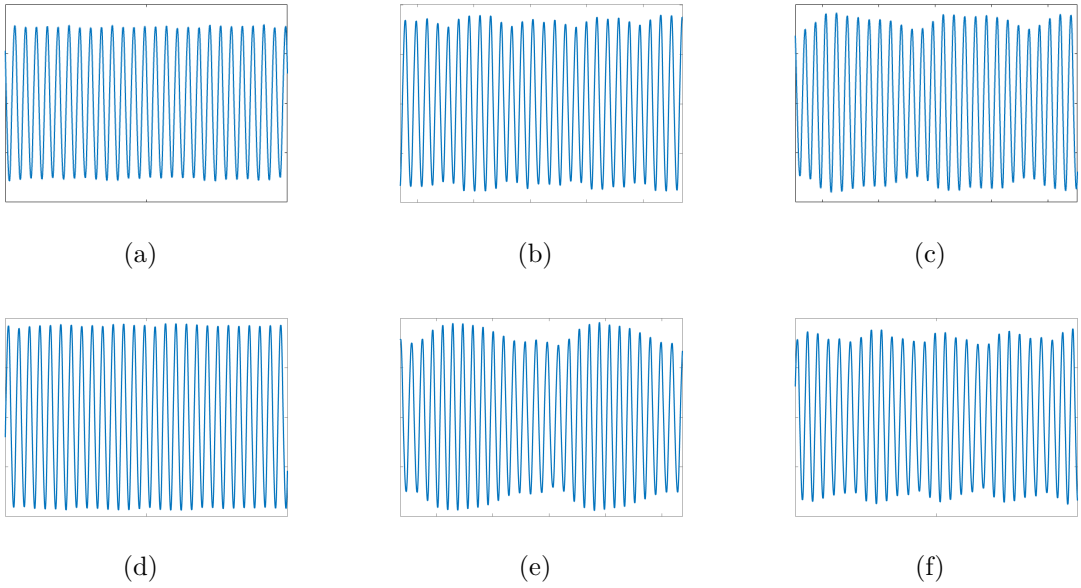

Figure 6.4: Key aeroelastic phenomenon summary with varying gust frequencies, represented by sketches of oscillating geometric pitch angle centered about zero: (a) $f_g = 1.45$ Hz; (b) $f_g = 2.2$ Hz; (c) $f_g = 2.4$ Hz; (d) $f_g = 2.7$ Hz; (e) $f_g = 2.9$ Hz; (f) $f_g = 3.1$ Hz, at $U_\infty = 7$ m/s.

At lower frequencies below 2 Hz, as shown in Fig. 6.4(a), the oscillation amplitude remains nearly constant across cycles. As the gust frequency increases, beating is gradually observed (b): plotting pitch over time reveals an amplitude envelope that periodically grows and decays, a clear visual marker of two competing, unsynchronized oscillations. Beating becomes increasingly pronounced from (b) to (c) as f_g rises, until reaching a lock-in band (d) where the oscillation amplitude is stabilized. Beyond the lock-in band, as gust frequency continues to increase (e–f), beating re-emerges, and the amplitude envelope trends towards constancy at even higher gust frequencies.

To analyze the phenomena better, a nondimensional standard deviation, σ_θ, is intro-

duced to assess the beating strength:

$$\sigma_\theta = \frac{\mathrm{std}(\theta_i)}{\bar{\theta}},$$

where $\mathrm{std}(\theta_i)$ is the standard deviation of the cycle-peak values (θ_i) and $\bar{\theta}$ is the averaged oscillation amplitude, $\bar{\theta} = \frac{1}{N}\sum_{i=1}^{N} |\theta_i|$. The beating parameter, $\sigma_\theta = 0$, indicates a purely constant LCO, and increases monotonically with the strength of amplitude modulation. The variations of f_θ, $\bar{\theta}$, and σ_θ against f_g are plotted in Fig. 6.5, where f_θ is the primary pitch frequency of stall flutter obtained from power spectral density (PSD) plots. The frequency resolution is 0.0046 Hz for the experimental results. As f_g approaches the lock-in band, σ_θ increases, denoting larger scales of beating; upon entering lock-in, σ_θ drops steeply, corresponding to oscillation with nearly constant amplitude. Thus, the beating variations at various f_g can be well assessed by σ_θ.

Besides constant-amplitude oscillation in time history, the other primary feature of lock-in is the oscillation frequency remaining aligned with f_g. This locked frequency is more clearly shown in Fig. 6.6, where the frequency ratio is exactly equal to unity within the lock-in band. Combining the trends of σ_θ and f_θ, the lock-in band is determined to be 2.5 to 2.8 Hz, a range centered around $f_{\theta,0} = 2.65$ Hz. Across the lock-in band, the amplitude generally increases with f_g; however, at the lower-frequency edge, it shows a distinct reduction rather than the expected rise. This behavior contrasts with the common expectation in classical vortex-induced vibration problems, where synchronization typically amplifies the structural response. Given that the amplitude is set by a balance between the aerodynamic energy input and the structural damping during oscillation, it is inferred that the initial phase adjustment between the gust forcing and structural response reduces the effective aerodynamic work per cycle, producing the entry-edge amplitude dip. This point of view can be supported by the amplitude recovery to the out-of-lock-in level with f_θ around $f_{\theta,0}$.

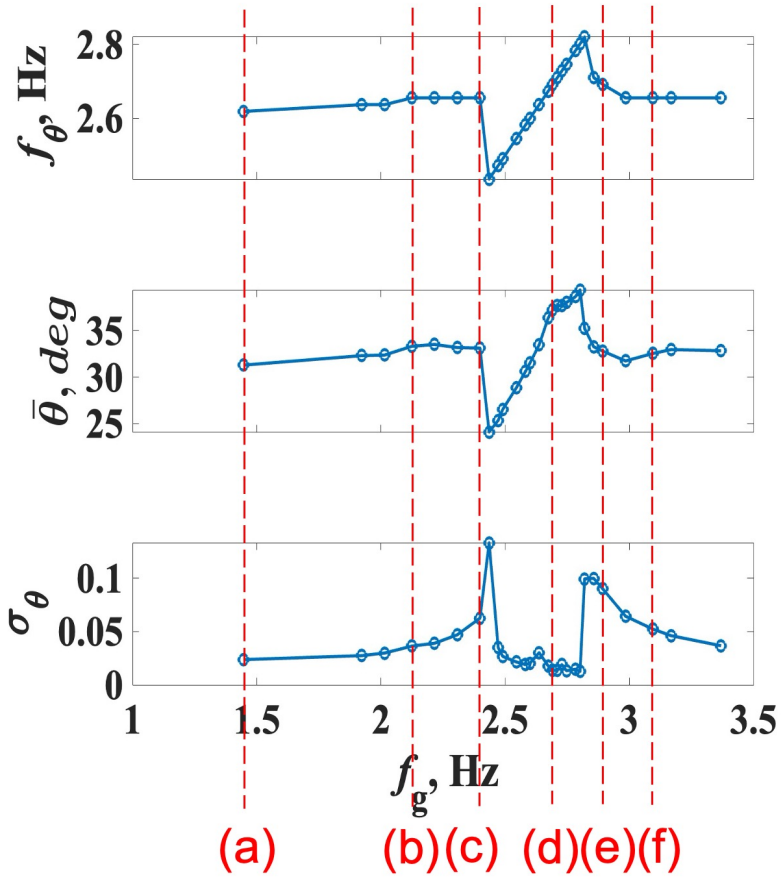

Figure 6.5: Aeroelastic response of stall flutter with frequency sweep of transverse gusts at $U_\infty = 7$ m/s.

The gust-induced stall flutter lock-in is somewhat similar to, but not entirely comparable with, the lock-in phenomena between pitch and heave in the two-DOF stall flutter system [60], [61]. In those studies, a notable observation was that at frequency ratios other than one, the pitch mode dominated the oscillation frequency; while with frequency ratios close enough to one, the heave amplitude surged, and the system's primary oscillatory frequency shifted to align with the heave-dominated mode due to the feedback mechanism between the two modes, indicating lock-in. In the pitch-heave aeroelastic system, pitch could be seen as the primary driver (input) of the aeroelastic response, while heave responded to the pitch motion (stall flutter), making it somewhat analogous to the plant in a control-theory framework. With this concept of analogy, the pitch in one-DOF

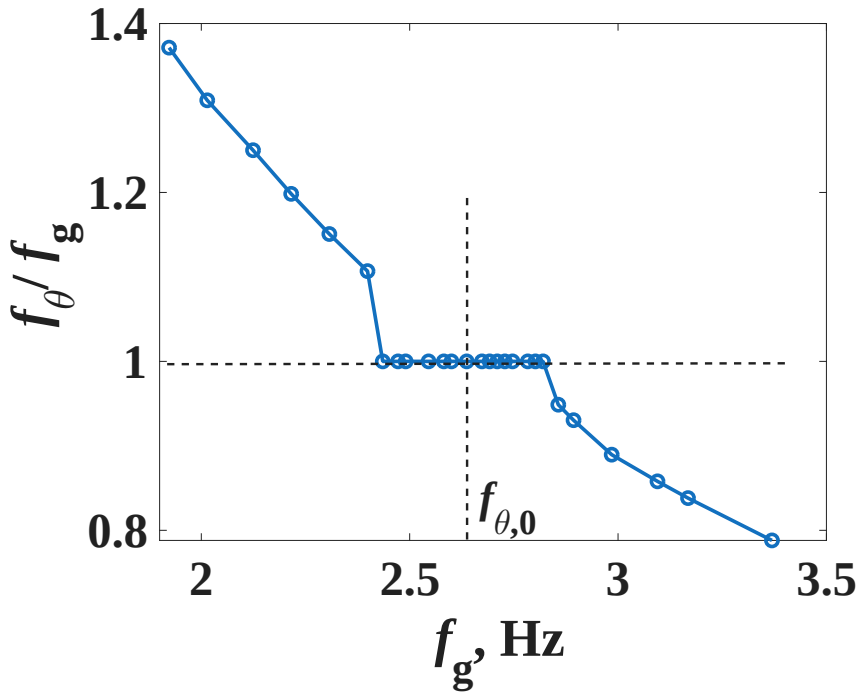

Figure 6.6: Frequency ratio as a function of f_g at $U_\infty = 7$ m/s.

stall flutter is the plant, and the gust is the driver in the present chapter. By contrast, gust-induced lock-in is an open-loop one-DOF mechanism (no feedback from the oscillator to the input), whereas pitch-heave lock-in represents a coupled mechanism, which can be called a two-DOF lock-in. Ref. [61] provided a detailed discussion regarding the differences between these two types of lock-in mechanisms.

Varying the gust frequency out of the lock-in band, the plant remains governed by the mean freestream and fixed structural characteristics: the primary oscillation frequency stays at $f_{\theta,0}$ and the averaged amplitude remains aligned with $\bar{\theta}_0$ (their values depicted in Fig. 6.2), while the gust introduces only amplitude modulation (a beating envelope). Within the lock-in band, as discussed above, the gust takes control of the plant, impacting both oscillation frequency and amplitude. Overall, the one-DOF aeroelastic system is dominated by the gust input during lock-in, but gust effects are not decisive out of lock-in.

With $f_g = 2.4$ ($< f_{\theta,0}$) and 3.1 Hz ($> f_{\theta,0}$), the gust response of stall flutter is shown in Figs. 6.7 and 6.8, respectively. In the PSD plots, the beating frequency, f_b, is

the difference between the gust and wing pitch frequencies. In addition to the primary pitch peak, the spectra exhibit several smaller *sideband peaks* on either side of it. These sidebands are discrete spectral peaks (not a continuous band) that arise from amplitude modulation: the modulation effectively replicates the main pitch peak at frequencies offset by integer multiples of the beat frequency, producing evenly spaced peaks around the carrier frequency. Accordingly, the frequency offset between each sideband and the primary pitch peak equals f_b, and the spacing between adjacent sidebands is also f_b. For instance, the sideband spacings are 0.25 and 0.45 Hz in Figs. 6.7(b) and 6.8(b), respectively, matching the frequency differences between the gust excitation and the pitch LCO. These beating frequencies are also confirmed by evaluating the beating envelope periods in Figs. 6.7(a) and 6.8(a).

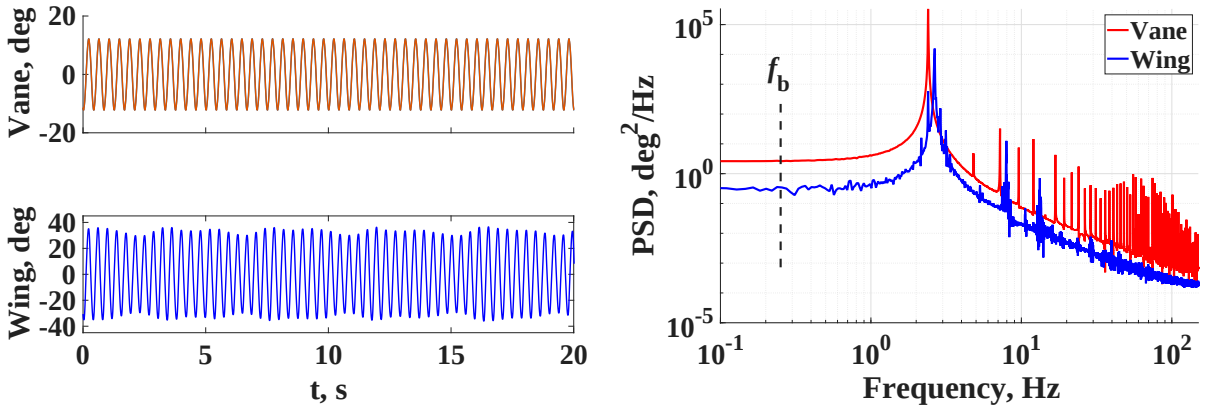

(a) (b)

Figure 6.7: Time histories (a) and PSD plots (b) for oscillating vanes and pitching wing with $f_g = 2.4$ Hz at $U_\infty = 7$ m/s, corresponding to case (c) in Fig. 6.5.

The beating frequency is faintly discernible in Fig. 6.8(b) but invisible in Fig. 6.7(b). In other scenarios at $U_\infty = 7$ m/s and other airspeeds not shown here, f_b does not occupy a distinct spectral peak in most cases. This denotes that the transverse gust acts as an external force on the nonlinear aeroelastic system [70], [74]. If the transverse gust had coupling effects with the plant (stall flutter system) itself, the response spectrum would embody the f_b content. The occasional, much smaller peaks near f_b, well below the peak

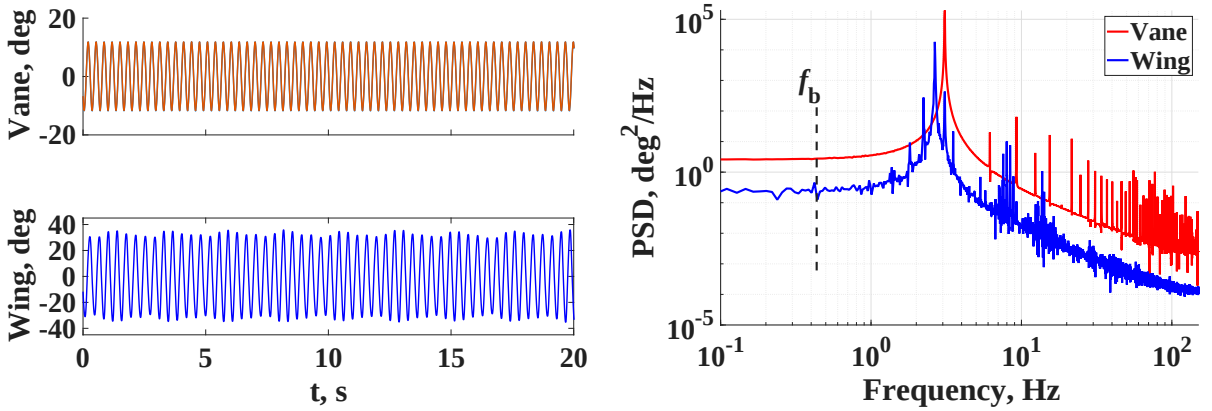

Figure 6.8: Time histories (a) and PSD plots (b) for oscillating vanes and pitching wing with $f_g = 3.1$ Hz at $U_\infty = 7$ m/s, corresponding to case (e) in Fig. 6.5.

at f_θ, are attributed to the weak u-variation in the gusting flow, which are unavoidable with the present gust generation method [92].

This interpretation is reinforced by our companion findings (detailed in the next chapter) for longitudinal gust excitation, where f_b emerges as a clear spectral peak despite only modest amplitude modulation in time history, whereas f_g is spectrally absent. Moreover, no lock-in occurs at a unity frequency ratio for the longitudinal case. Combining these features indicates that the longitudinal gust enters the dynamics as a parametric excitation, whereas the transverse gust acts as an external force.

As the gust frequency approaches $f_{\theta,0}$ closely enough, for instance, at $f_g = 2.7$ Hz, stall flutter lock-in is observed, as shown in Fig. 6.9. The fundamental feature of the lock-in phenomena is that the pitch frequency is shifted to the gust frequency across a finite frequency band, supported by the frequency coincidence in Fig. 6.9(b). This frequency synchronization band is clearly observed in Fig. 6.6. Within this frequency range, limit cycle oscillations exhibit nearly constant rather than modulated amplitude, see Fig. 6.9(a). Consequently, the lower-level beating corresponds to the remarkable drop of σ_θ in Fig. 6.5.

Near the edge of the lock-in band, the response exhibits mixed behaviors, perform-

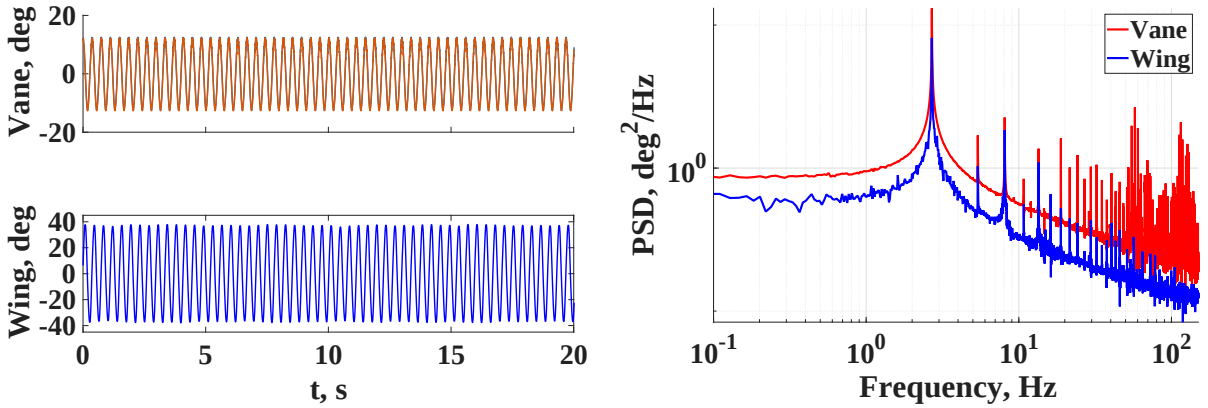

Figure 6.9: Time histories (a) and PSD plots (b) for oscillating vanes and pitching wing with $f_g = 2.7$ Hz at $U_\infty = 7$ m/s, corresponding to case (d) in Fig. 6.5.

ing both frequency synchronization and amplitude modulation, as shown in Fig. 6.10. Although the primary pitch frequency is locked to the gust frequency, the beating envelope persists, becoming even more pronounced than in the two preceding beating cases in Figs. 6.7 and 6.8. Since the primary and gust frequencies coincide at 2.44 Hz, the beating frequency is given by the sideband spacing (or the difference between the primary peak and the highest sideband), yielding $f_b = 0.19$ Hz. Considering that the highest sideband is 2.63 Hz, close to $f_{\theta,0}$ at $U_\infty = 7$ m/s, this case corresponds to the transitional state between beating and fully lock-in. This behavior is consistent with classical synchronization theory under external forces: near lock-in boundaries, systems can remain frequency-locked while the amplitude exhibits strong modulation under large external forcing [97]. The existence of this transitional state attests to the complexity and nonlinearity of the gust-forced stall flutter.

Considering $U_\infty = 7$ m/s is close to the onset airspeed of stall flutter, several higher airspeeds, $U_\infty = 8$, 9, and 10 m/s, are also tested, as shown in Fig. 6.11. The gust-induced beating and lock-in are widely observed at all airspeeds tested. The black dashed line denotes a ratio of one. Before lock-in, all the primary pitch LCO frequencies are close to the frequencies under uniform freestream conditions (Fig. 6.2). At the onset of lock-in, the

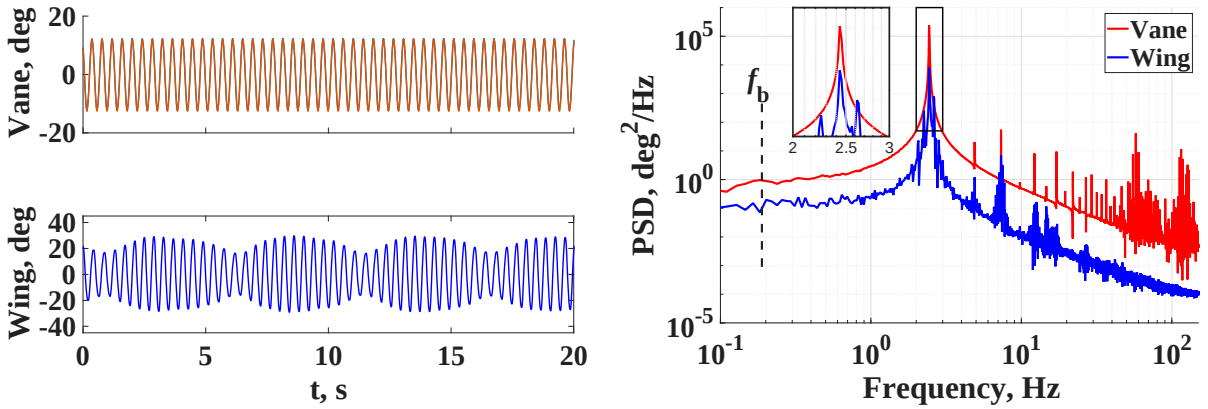

(a) (b)

Figure 6.10: Time histories (a) and PSD plots (b) for oscillating vanes and pitching wing with $f_g = 2.44$ Hz at $U_\infty = 7$ m/s.

pitch frequency drops to align with the gust frequencies and remains consistent throughout the lock-in band. As f_g increases beyond the lock-in band, the flutter frequency recovers to the corresponding $f_{\theta,0}$ under uniform freestream conditions.

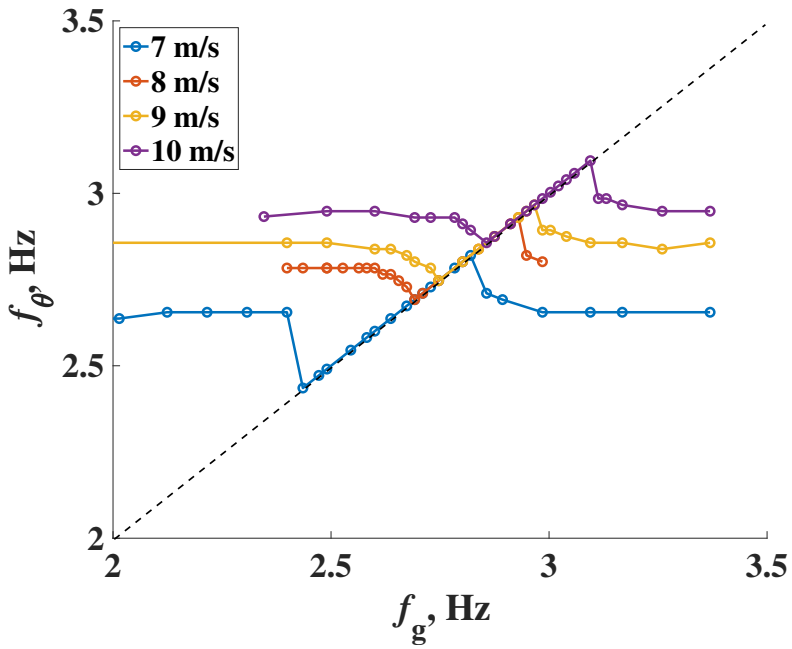

Figure 6.11: Pitch oscillation frequency as a function of gust frequency at $U_\infty = 7$, 8, 9, and 10 m/s.

Outside lock-in, the mean LCO amplitude remains nearly constant and close to the

no-gust value (baseline amplitude), as shown in Fig. 6.12. Within the lock-in band, the amplitude increase is nonlinear. For $U_\infty = 10$ m/s, the amplitude growth approaches an apparent limitation. This limitation is close to the value of the plateau under uniform flow conditions, as shown in Fig. 6.2(a). This finding agrees well with the previous discussions in Ref. [60] and in another literature [95]: there existed an LCO amplitude convergence for stall flutter with growing airspeeds. The finding in this study suggests that this convergence also limits the amplitude of stall flutter lock-in induced by transverse gusts. Figure 6.13 shows that the overall beating trends for all airspeeds are similar while denoting different frequency ranges of lock-in. Combining Figs. 6.11 and 6.13, the lock-in band tends to be narrower with a larger baseline amplitude as U_∞ increases.

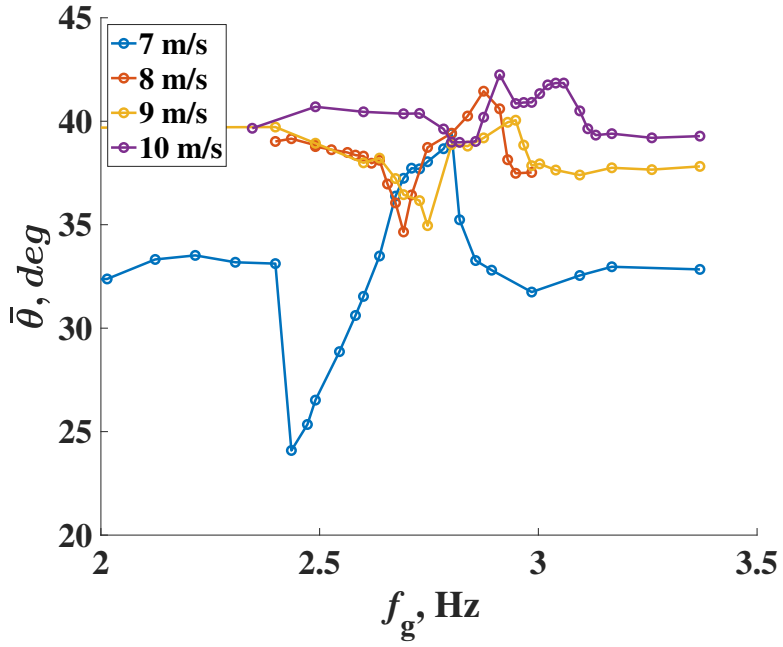

Figure 6.12: Averaged pitch oscillation amplitude as a function of gust frequency at $U_\infty = 7$, 8, 9, and 10 m/s.

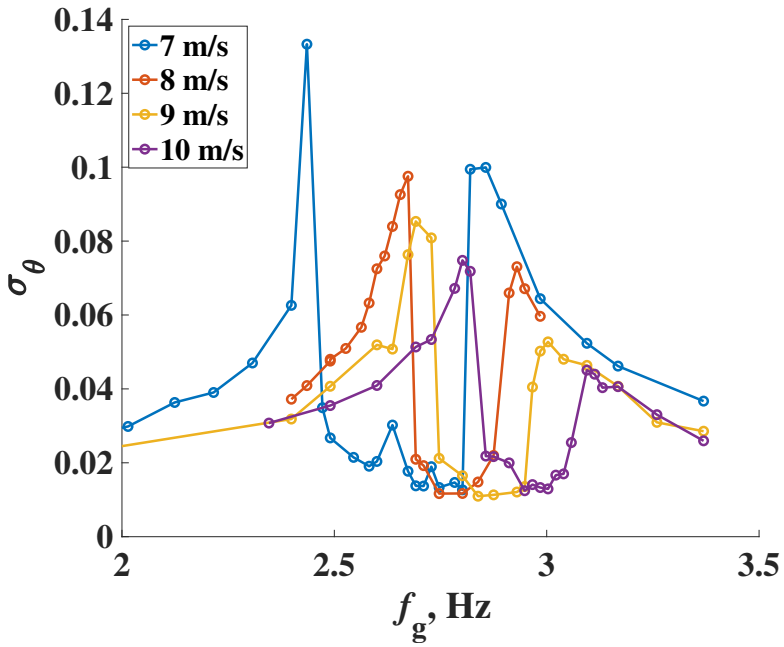

Figure 6.13: Normalized beating strength as a function of gust frequency at $U_\infty = 7$, 8 , 9, and 10 m/s.

A smaller vane amplitude of 6° is also tested to examine the effects of the weaker external forcing on the gust-induced lock-in and beating. Figure 6.14 shows a beating case when $f_g = 2.75$ Hz is close to $f_{\theta,0}$. At the same gust frequency, the system is within the lock-in band for a vane amplitude of 12°, as shown in Fig. 6.11. Figure 6.15 shows frequency sweeps at $U_\infty = 7$–10 m/s. It is observed that lock-in bands persist but become consistently narrower for all the tested airspeeds with weaker transverse gusts. Besides, out of the lock-in band, the primary oscillation frequency overall remains aligned with $f_{\theta,0}$ for the corresponding airspeeds.

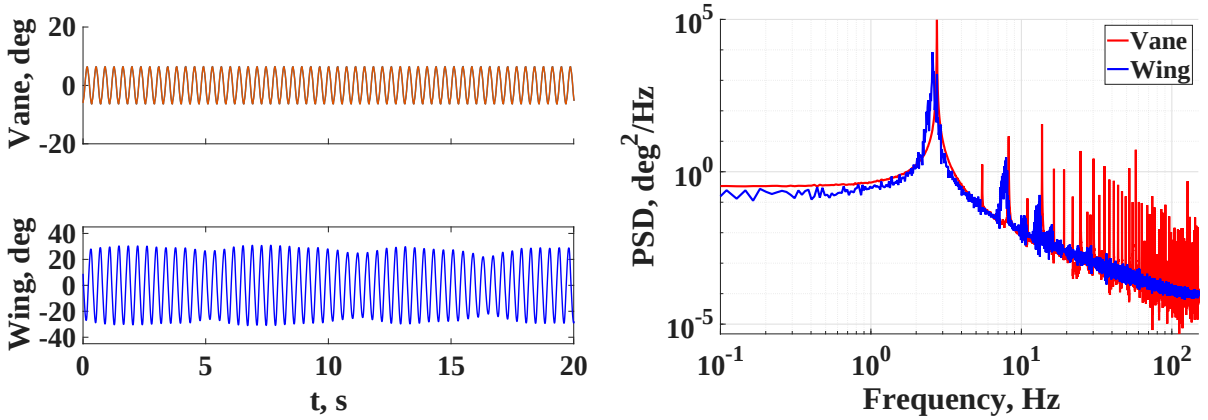

(a) (b)

Figure 6.14: Time histories and PSD plots for oscillating vanes and pitching wing with $f_g = 2.75$ Hz with vane amplitude being 6° (smaller gust) at $U_\infty = 7$ m/s.

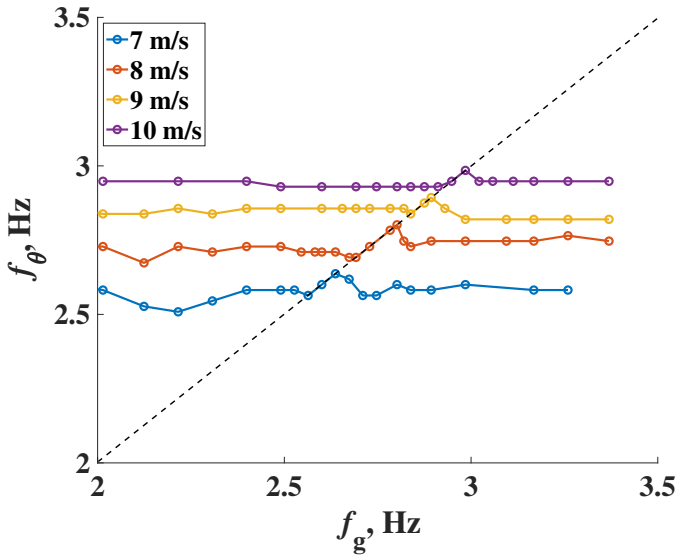

Figure 6.15: Pitch oscillation frequency as a function of gust frequency at $U_\infty = 7$, 8, 9, and 10 m/s, with vane amplitude being 6° (smaller gust).

6.3 Transverse-Gust-Forced van der Pol Oscillator

To interpret the experimental observations from the preceding section, the focus is shifted from the experimental evidence to the development of an analytical model. The pitch-only stall flutter is a one-DOF self-sustained instability that requires negative aerodynamic damping, so that the flow does net positive work on the structure. From an energy viewpoint, if the cycle-integrated aerodynamic work is positive, the motion grows until a nonlinear mechanism limits the amplitude. Practically, two ingredients are needed: (i) a loss of equilibrium via net negative damping of aerodynamic origin that overcomes structural damping, and (ii) a nonlinear saturation that re-stabilizes the motion onto a limit cycle rather than letting it diverge. These ingredients are compactly captured by the van der Pol (VdP) oscillator, which can act as a minimal phenomenological model for the pitch dynamics [70]. In this context, a minimal model refers to a reduced-order oscillator equation designed to capture the essential features of the instability, specifically the competition between energy input and nonlinear saturation, without resolving the underlying flow field. By stripping away complex aerodynamic details, such a model isolates the fundamental synchronization mechanisms governing the fluid-structure interaction.

6.3.1 From one-DOF aeroelastic pitch to forced van der Pol oscillator

Consider the standard one-DOF pitch aeroelastic equation about the elastic axis (EA):

$$I\,\ddot{\theta} + c_s\,\dot{\theta} + k_s\,\theta \;=\; M_{\mathrm{EA}}(t,\theta,\dot{\theta},\ddot{\theta}), \tag{6.1}$$

where $\theta(t)$ is the pitch angle; I is the mass polar moment of inertia about the EA; c_s is the structural torsional damping about the EA; k_s is the structural torsional stiffness about the EA; M_{EA} is the unsteady aerodynamic pitching moment about the EA.

To capture the onset of self-sustained stall flutter and its saturation with minimal terms, assume a quasi-steady representation for the aerodynamic moment [71]:

$$M_{\mathrm{EA}}(\theta,\dot{\theta}) \;\approx\; k_a\,\theta \;+\; c_a\,\dot{\theta} \;-\; c_n\,\theta^2\dot{\theta}, \tag{6.2}$$

where

- k_a is the (quasi-steady/linearized) negative aerodynamic stiffness coefficient (moment slope with respect to angle); it modifies the effective torsional stiffness.
- $c_a > 0$ is the aerodynamic (destabilizing) damping coefficient; when moved to the left-hand side of Eq. (6.1) it reduces the net damping, enabling growth when $c_a > c_s$ (negative net damping).
- $c_n > 0$ is a leading-order nonlinear (cubic-in-amplitude) aerodynamic coefficient that increases the effective damping with amplitude ($\propto \theta^2\dot{\theta}$), providing saturation and a finite limit cycle.

Substituting Eq. (6.2) into Eq. (6.1) and collecting terms gives

$$I\,\ddot{\theta} \;+\; \underbrace{\left(c_s - c_a + c_n\,\theta^2\right)}_{\text{effective damping}}\,\dot{\theta} \;+\; \underbrace{\left(k_s - k_a\right)}_{\text{effective stiffness}}\,\theta \;=\; 0, \tag{6.3}$$

so that $c_a > c_s$ yields net negative (energy-adding) damping at small amplitude, while $c_n > 0$ restores positive damping at larger amplitude, producing a limit cycle.

Introducing the nondimensional variables and parameters

$$x = \frac{\theta}{\bar{\theta}_0}, \qquad \omega_0^2 = \frac{k_s - k_a}{I}, \qquad \tau = \omega_0 t,$$

where $\bar{\theta}_0 > 0$ is a characteristic pitch-angle scale used for nondimensionalization (e.g., the baseline no-gust limit-cycle amplitude, expressed in radians) so that $x = O(1)$ over the

range of interest. With a small quantity $\epsilon \ll 1$ (higher order of this term can be ignored),

$$\epsilon\bar{\mu} = \frac{c_a - c_s}{I\omega_0}, \qquad \epsilon\nu = \frac{c_n\,\bar{\theta}_0^2}{I\omega_0},$$

the equation becomes the classical VdP form

$$x'' - \epsilon\big(\bar{\mu} - \nu x^2\big)x' + x \;=\; 0, \tag{6.4}$$

where $(\;)'$ denotes $d/d\tau$. In the presence of a transverse gust, the minimal model is augmented with a weak harmonic input that represents the gust-induced aerodynamic moment,

$$\boxed{x'' - \epsilon\big(\bar{\mu} - \nu x^2\big)x' + x \;=\; \epsilon \underbrace{F_g}_{\text{gust level}} \cos\big(\Omega\,\tau\big),} \tag{6.5}$$

where $\Omega = \omega_g/\omega_0$. This is the nondimensional phenomenological model used to reproduce the gust-forced stall flutter. In this notation, $\bar{\mu} > 0$ stands for the net negative (energy-adding) aerodynamic effect, while $\nu > 0$ sets the saturation that limits the amplitude.

6.3.2 Method of averaging

When the forcing frequency ω_g lies sufficiently close to the natural frequency ω_0 ($\Omega \approx 1$) and the nonlinearity/forcing are weak ($\epsilon \ll 1$), the response can be expressed as a slowly modulated carrier [70], [96],

$$x(\tau) \approx r(\tau)\cos\big(\tau + \phi(\tau)\big), \tag{6.6}$$

where $r(\tau)$ is the slowly varying amplitude and $\phi(\tau)$ is the phase with $r', \phi' = O(\epsilon)$. Define the phase difference of the response with respect to the gust as

$$\begin{aligned} \psi(\tau) &= \tau + \phi(\tau) - \Omega\,\tau \\ &= -\Delta\,\tau + \phi(\tau), \end{aligned} \tag{6.7}$$

where $\Delta = \Omega - 1$ is the detuning parameter (a control parameter based on the input gust). Insert $x(\tau) = r(\tau)\cos\big(\tau + \phi(\tau)\big)$ into Eq. (6.5), differentiate using the product rule (with $r', \phi' = O(\epsilon)$), project the residual onto the basis $\{\cos(\tau+\phi), \sin(\tau+\phi)\}$, and average over one carrier cycle, 2π, to remove rapidly oscillating terms. This standard averaging procedure yields the slow "amplitude–phase" system (see Ref. [96] for more details)

$$\begin{aligned} r' &= \tfrac{1}{2}\bar{\mu}\,r - \tfrac{1}{8}\nu\,r^3 - \tfrac{F_g}{2}\sin\psi, \\ \psi' &= \Delta - \tfrac{F_g}{2r}\cos\psi. \end{aligned} \tag{6.8}$$

These equations have a direct physical reading: r' is an energy balance (aerodynamic work in vs. saturation/structural loss, plus the gust contribution via $\sin\psi$), while ψ' is a phase balance (detuning causes phase slip; forcing via $\cos\psi$ tries to hold a fixed phase). In addition, the expression of ψ' contains no $r(\tau)$-dependent term, indicating no amplitude-dependent phase (frequency) shift. This reflects the VdP nonlinearity being purely dissipative, i.e., modulating damping but not stiffness.

6.3.3 Lock-in and consequences

At synchronization ($r' = \psi' = 0$), one finds

$$\cos\psi = \frac{2r\,\Delta}{F_g}, \qquad \sin\psi = \frac{r}{F_g}\Big(\bar{\mu} - \tfrac{1}{4}\nu r^2\Big), \tag{6.9}$$

and, by elimination,

$$\boxed{{F_g}^2 \;=\; 4r^2\Delta^2 + \left(\bar{\mu}r - \tfrac{1}{4}\nu r^3\right)^2.} \tag{6.10}$$

This relation is the lock-in condition: the gust can simultaneously satisfy the energy and phase balances only for (r, Δ) pairs lying on this curve.

From the boxed condition, Eq. (6.10), and the slow-flow system, Eq. (6.8), the minimal model reproduces the primary observed features:

- **Finite synchronization window:** a bounded lock-in region (Arnold-tongue-like band) about ω_0 in which a phase-locked periodic solution with constant amplitude exists.

- **Outside lock-in:** a quasi-periodic response with beating at $f_b = |f_g - f_{\theta,0}|$ (equivalently $f_b = |\Delta|\omega_0/(2\pi)$). The phase difference drifts at the beat rate, so the forcing term in the averaged amplitude equation averages to zero over a beat period; consequently, the long-time mean amplitude follows the unforced slow flow and relaxes to the no-gust limit-cycle value $r_0 = 2\sqrt{\bar{\mu}/\nu}$.

- **Inside lock-in:** an amplitude profile that is symmetric with respect to detuning about ω_0 (i.e., invariant under $\Delta \to -\Delta$) and therefore attains its maximum at $\Delta = 0$ (i.e., $\omega_g = \omega_0$).

A back-of-the-envelope half-width estimate obtained by evaluating the boxed relation near $r = r_0$ yields

$$\boxed{|\Delta|_{\max} \;\approx\; \frac{F_g}{2\,r_0},} \tag{6.11}$$

implying that stronger gusts or smaller baseline amplitudes widen the synchronization window, which agrees well with the experimental observations.

6.3.4 Analytico-numerical verification

Setting $F_g = 1$ as the nominal case, and adjusting the values of $\epsilon, \bar{\mu}$, and ν, the analytico-numerical solution reproduces the experimental measurements at $U_\infty = 7$ m/s, such as $\overline{\theta}_0 = 33°$ and $f_{\theta,0} = 2.65$ Hz. With $f_g = 2.4$ Hz, the gust-forced VdP response is shown in Fig. 6.16. Out of the lock-in band, amplitude modulation is observed in the time history, and the spectral beating peak is absent in the PSD plot, as expected. The primary peak occurs at $f_{\theta,0} = 2.65$ Hz, and sidebands are evenly distributed with f_b as the interval. Figures 6.17 and 6.18 depict two frequency sweeps to examine the effects of the external forcing F_g and the no-gust oscillation amplitude $\overline{\theta}_0$ on the lock-in band, respectively. Lock-in bands can be determined either by the linear proportion ($f_\theta = f_g$) or the no-beating indicator ($\sigma_\theta = 0$). Higher F_g or lower $\overline{\theta}_0$ widens the lock-in band, confirming the analytical derivation in Section 6.3.3 as well as matching the experimental observations in Section 6.2.

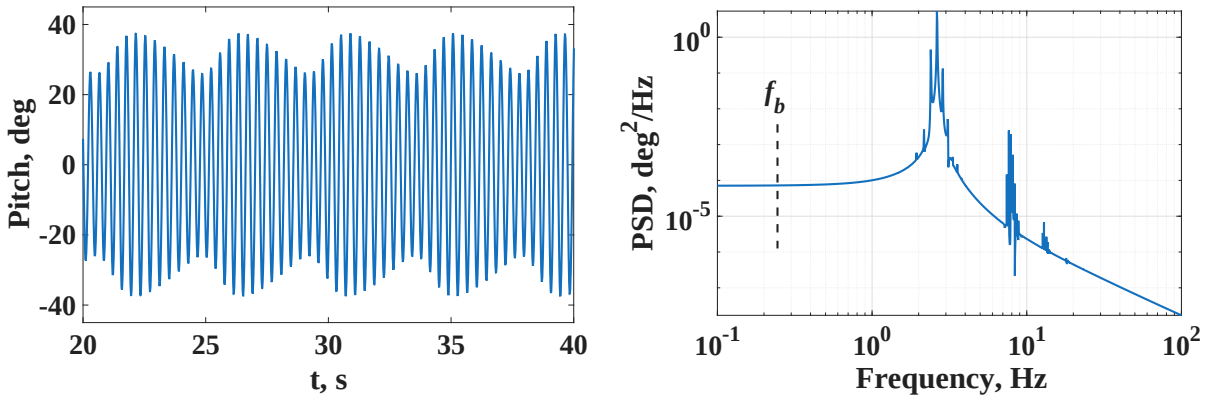

(a) (b)

Figure 6.16: Analytico-numerical time history and PSD plot for stall flutter at $f_g = 2.4$ Hz with $f_{\theta,0} = 2.65$ Hz, reproducing the stall flutter forced by transverse gusts shown in Fig. 6.7.

The numerical results predict a decrease in the oscillation amplitude with a stronger external forcing at both edges of the lock-in band. However, the intra-band amplitude trend in the experiments is more nuanced: the measured amplitude tends to increase

monotonically with f_g across the band (before amplitude convergence) and peaks near the upper edge (see Fig. 6.5), whereas the minimal forced van der Pol model predicts a symmetrical profile peaking at the center ($\omega_g = \omega_0$). This discrepancy suggests that additional weak physics (asymmetries) influence the phase balance within lock-in. Although a revised reduced-order model is further needed to capture detailed amplitude trends, it is noted that the current analytical framework captures the principal features of transverse-gust-forced stall flutter, thereby supporting the analysis of the complex physics underpinning the experimental observations.

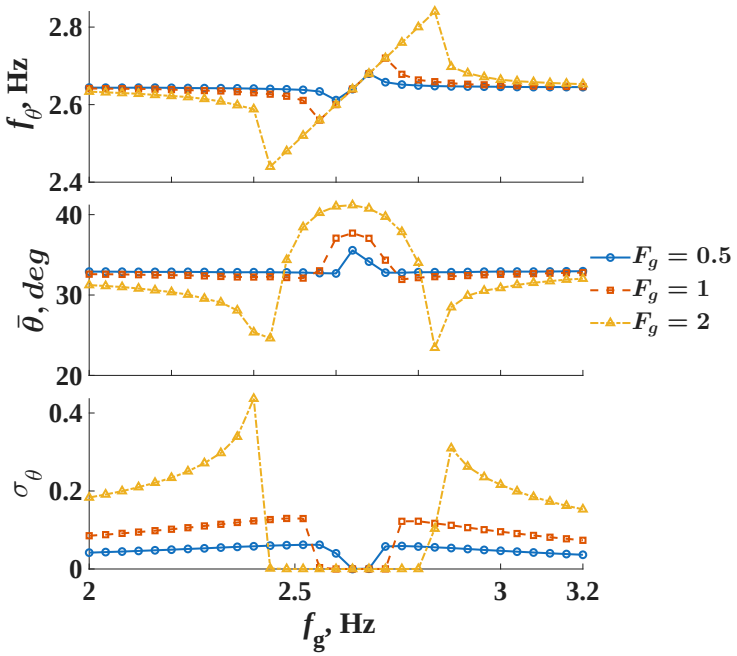

Figure 6.17: Analytico-numerical result summary with frequency sweeps of external forcing with $\bar{\theta}_0 = 33°$ and $F_g = 0.5$, 1, 2; reproducing beating and lock-in observed for stall flutter forced by transverse gusts shown in Fig. 6.5.

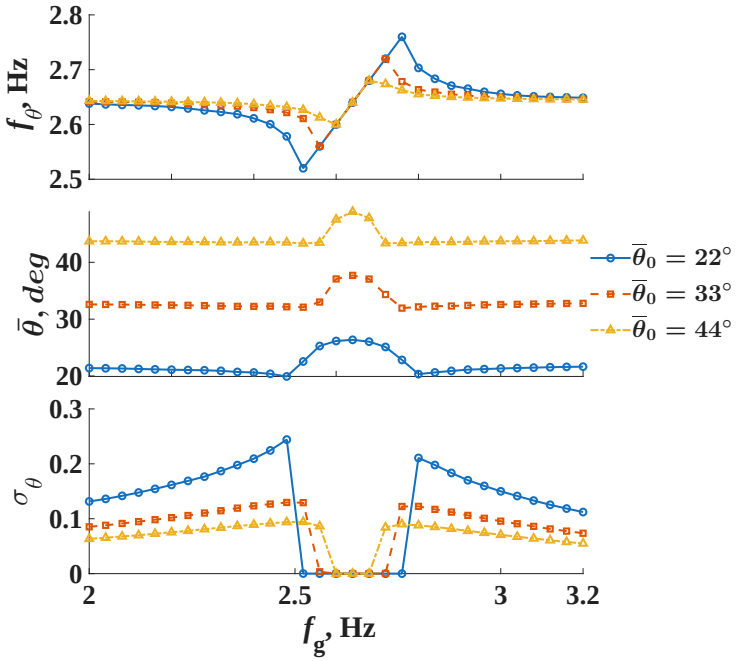

Figure 6.18: Analytico-numerical result summary with frequency sweeps of external forcing with $F_g = 1$ and $\bar{\theta}_0 = 22°, 33°, 44°$; reproducing beating and lock-in observed for stall flutter forced by transverse gusts shown in Fig. 6.5.

6.4 Stall Flutter Advancement by Transverse Gusts

While the preceding sections of this chapter focused on the post-onset regime ($U_\infty \geq$ 7 m/s), primarily a performance and structural load concern, this section investigates the influence of harmonic transverse gusts on the stability boundary of the system.

Figure 6.19 illustrates the stall flutter onset boundary as a function of gust frequency. In the absence of external excitation, the baseline onset speed is $U_{SF,onset} = 6$ m/s, which is also indicated in Fig. 6.2(a). Experimental results indicate that transverse gusts generally advance the onset of stall flutter (lowering the critical airspeed). As shown in Fig. 6.2(b), the intrinsic limit cycle frequency at the baseline onset is $f_{\theta,0} = 2.54$ Hz. When the gust frequency f_g is far from $f_{\theta,0}$, $U_{SF,onset}$ is reduced by approximately 0.5 m/s. However, as f_g approaches $f_{\theta,0}$, the onset speed exhibit a sensitivity trend: it increases slightly near $f_g = 2.35$ Hz and 2.8 Hz before decreasing dramatically as it nears resonance. The system reaches its lowest onset speed of 3.82 m/s at $f_g \approx f_{\theta,0}$, resulting in a characteristic "wedge-like" or V-shaped stability boundary centered around the structural natural frequency.

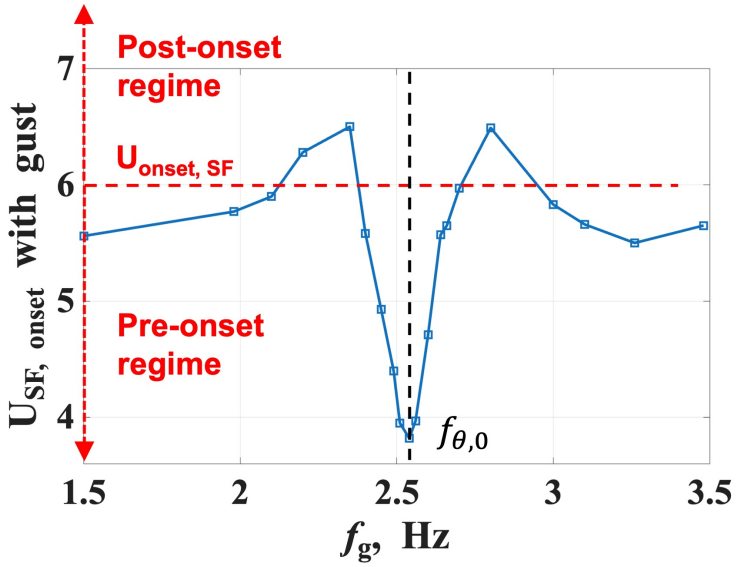

Figure 6.19: Critical onset airspeed of stall flutter as a function of gust frequency, illustrating the advancement of the instability boundary.

At $f_g = 3.48$ Hz, the gust response in the pre-onset regime is shown in Fig. 6.20. This

behavior mirrors the beating patterns observed in the post-onset regime (e.g., Figs. 6.7 and 6.8): the dominant response frequency remains at $f_{\theta,0}$, and the spectral sidebands appear at $f_i = |f_g - (i-1)f_b|$, while f_b lacks a distinct peak. The early onset is sustained by continuous energy injection from the gust, specifically through enhanced dynamic stall effects by transverse gusts.

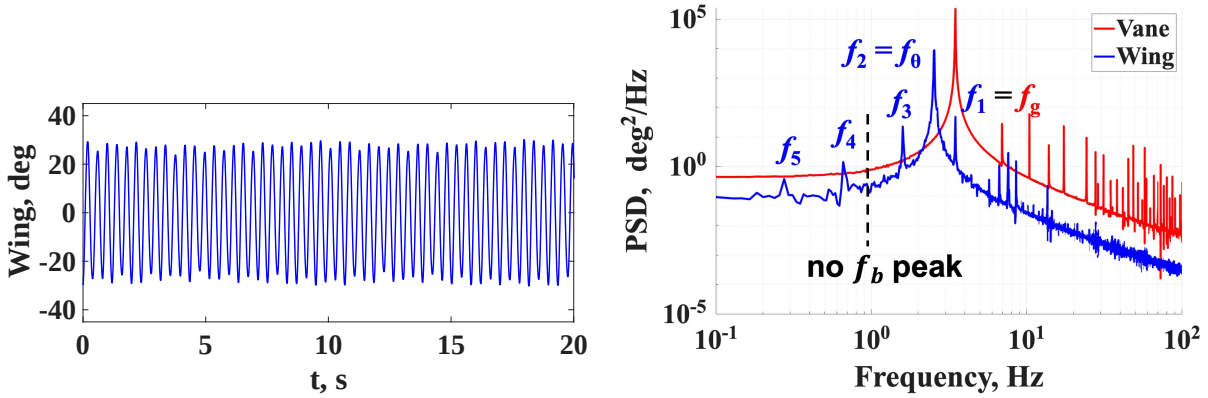

(a) (b)

Figure 6.20: Time history (a) and PSD (b) for the pitching wing at $U_\infty = 5.65$ m/s and $f_g = 3.48$ Hz. Sidebands are marked at $f_i = |f_g - (i-1)f_b|$.

In contrast, at $f_g = 2.55$ Hz, the response aligns with the lock-in patterns observed in the post-onset regime (e.g., Fig. 6.9), where the flutter frequency synchronizes with the gust frequency. As shown in the time history of Fig. 6.21, the initial stage consists of gust-forced linear oscillations, which can be predicted analytically by combining Wagner's and Küssner's functions. Upon applying a large external perturbation, stall flutter is triggered following a transient phase. In particular, the freestream velocity decreases by approximately 0.2 m/s at the onset of stall flutter compared with the case of no stall flutter based on the mean velocity measurement using the pitot tube. This drop is attributed to increased total pressure losses within the wind tunnel circuit, caused by energy extraction from the flow and significant wake blockage associated with the LAOs. In this state, the flutter amplitude remains nearly constant, averaging approximately 29°. This lock-in pattern persists across an airspeed range from $U_\infty = 3.92$ m/s to 6.3 m/s, with the average

amplitude varying only slightly between 27° and 30°.

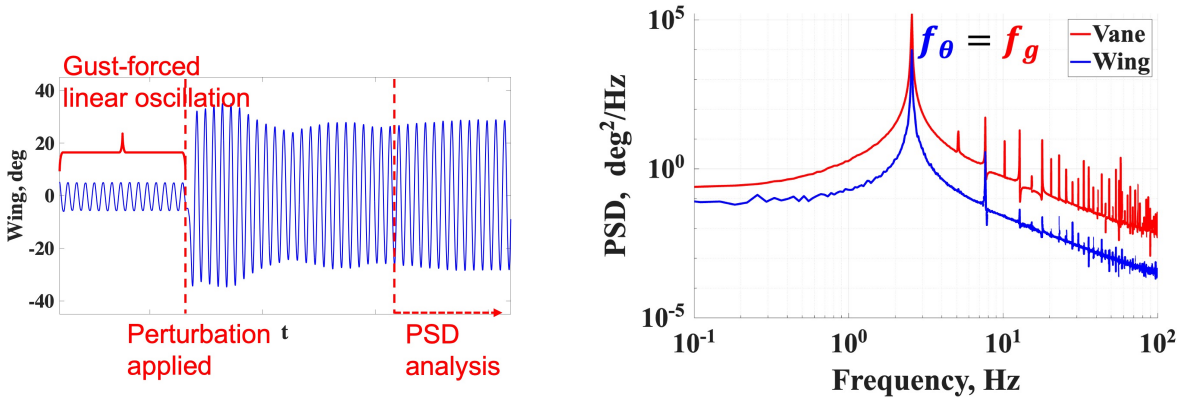

Figure 6.21: Time history (a) and PSD (b) illustrating lock-in behavior at $U_\infty = 5.1$ m/s and $f_g = 2.55$ Hz.

A transient state, characterized by frequency lock-in accompanied by spectral sidebands and large-scale amplitude modulation, is observed at the stall flutter boundary (Fig. 6.22). This response is qualitatively similar to the post-onset behavior shown in Fig. 6.10. However, the states outside the boundary differ significantly: the pre-onset regime exhibits small constant-amplitude oscillations corresponding to gust-forced linear oscillation, as depicted by the first stage of Fig. 6.21(a); whereas the post-onset regime maintains stall flutter with beating. The significant amplitude modulation appears to delay the onset of non-fully developed stall flutter. In cases where the gust frequency delays onset (the blue curve above the red dash line in Fig. 6.19), LAOs with strong beating persist for several cycles before the oscillations damp out to small amplitude, typically when the minimum amplitude of a beating cycle falls near or below the static stall angle.

Finally, the system's bifurcation diagram is updated to account for these representative gust frequencies in Fig. 6.23. The onset effects of lower and higher gust frequencies are revealed in Fig. 6.19. Transverse gusts advance the stall flutter onset to varying extent depending on f_g, and the resulting LCO amplitudes are also frequency-dependent. In the bi-attractor zone (between $U_{SF,onset}$ and U_D), gust frequencies of $f_g = 2.45$ and 2.53 Hz

yield lower average amplitudes, corresponding to the initial drop at the lower boundary of the lock-in band seen in Fig. 6.5. This capability of transverse gusts to fundamentally alter the stability map and bifurcation characteristics of the stall flutter system is a compelling finding, warranting the analytical investigations currently underway for future publication.

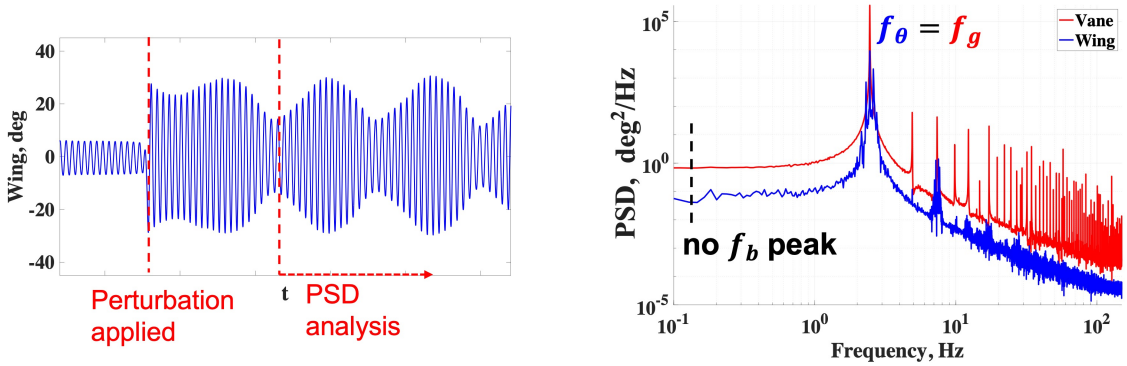

(a) (b)

Figure 6.22: Time history (a) and PSD (b) showing modulated lock-in at the stability boundary ($U_\infty = 5.1$ m/s, $f_g = 2.45$ Hz).

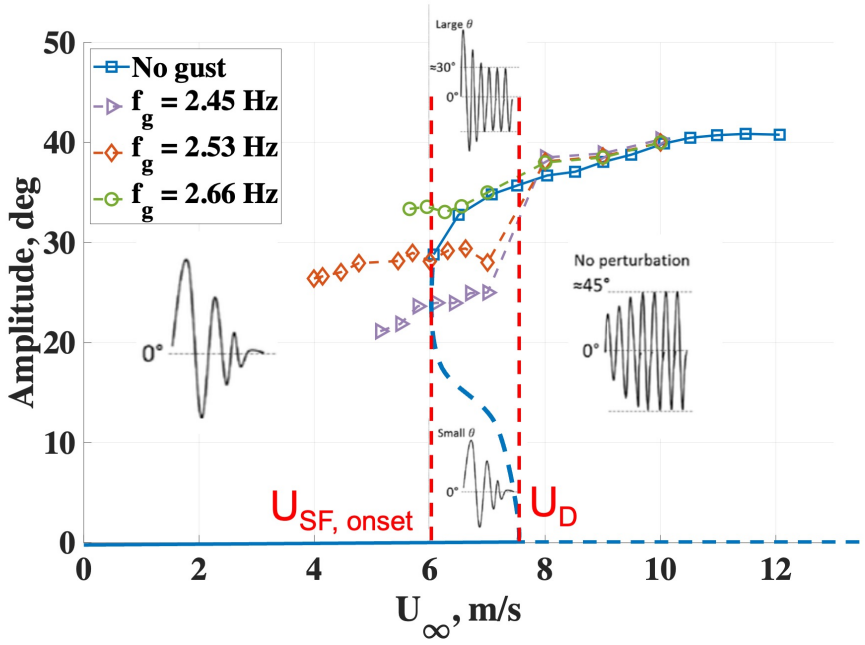

Figure 6.23: Updated bifurcation diagram illustrating the advancement of stall flutter attractors under transverse gust excitation.

Chapter 7

STALL FLUTTER EXCITED BY LONGITUDINAL GUSTS

As noted earlier, most studies on stall flutter focused on either steady uniform freestream conditions or transverse gusts, while the influence of longitudinal (streamwise) gusts on stall flutter remains largely underexplored. Unlike transverse gusts, which primarily perturb the effective angle of attack, longitudinal gusts modulate the freestream speed and thereby the dynamic pressure [31], introducing a different coupling pathway. From a classical (linear) aeroelasticity point of view, such velocity fluctuations alter the effective stiffness and damping of the system; that is, they modify the aeroelastic plant itself rather than acting as an external generalized force [10], [35], [37]. For a strongly nonlinear oscillator such as stall flutter associated with a large scale of flow separation, however, it is not evident a priori whether longitudinal gusts act purely through parametric (plant) modulation, or also introduce other effects. This question motivates the present investigation.

This chapter aims to disclose the effects of longitudinal gusts on stall flutter. Chapter 6 investigated the impact of transverse gust on stall flutter, using the same experimental facility as the present study. By modifying the gust generation strategy, performing anti-phase vane motion instead of in-phase motion for transverse gusts, harmonic longitudinal gusts are generated, as depicted in Fig. 7.1. Experimental results are presented and inter-

preted in Section 7.1 to analyse the differences in nonlinear aeroelastic response between the present longitudinal gusts and previously studied transverse gusts. Analytically, a minimal phenomenological model is developed in Section 7.2 to aid in understanding the complex observations and making some predictions beyond experimental constraints.

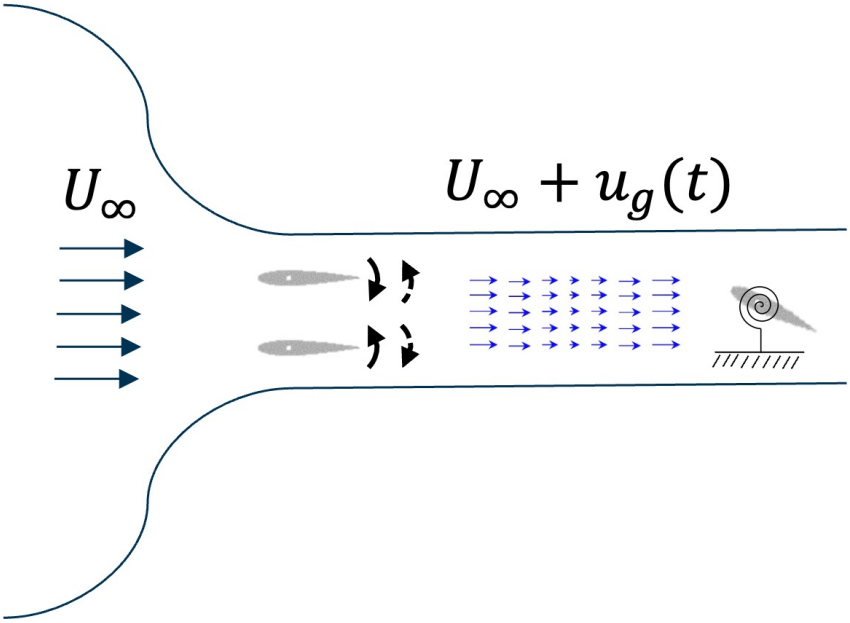

Figure 7.1: Sketch of an aeroelastic wing undergoing stall flutter, encountering longitudinal gusts generated by the upstream gust generator.

7.1 Experimental Results

Gust response tests are conducted at $U_\infty = 10$ m/s, a velocity well above the onset speed of stall flutter. With the anti-phase vane motion, the longitudinal gusts generated are depicted in Fig. 4.11, behaving in the nearly harmonic pattern as desired, $U(t) = U_\infty + u_{g,max} \sin(2\pi f_g t)$. The fluttering motion is self-induced and persists under the excitation of longitudinal gusts. In the absence of gust, the pitch-flutter frequency is measured as $f_{\theta,0} = 2.93$ Hz. Under longitudinal-gust excitation at $f_g = 2.5$ Hz, the upper plot in Fig. 7.2(a) shows the pitch angles of the two vanes in anti-phase motion. The lower time history of the wing pitch angle reveals slight amplitude modulation (beating). The PSD in

Fig. 7.2(b) shows that the beating frequency, $f_b = |f_\theta - f_g|$, appears as a distinct peak in the wing PSD. In addition, harmonic pairs with components at $|mf_\theta \pm nf_g|$ (m is odd and $n = 1, 2, 3 \ldots$) are also observed, while f_g does not appear as a distinct peak in the wing response. By comparison, Chapter 6 investigated the stall flutter response to transverse gusts and reported substantially stronger beating in the time histories outside lock-in, while the wing spectrum showed no distinct beating peak and the highest sideband was the gust frequency, indicating that the transverse gust acts as an external force.

Increasing the gust frequency to 2.96 Hz (nearly matching $f_{\theta,0}$) does not yield lock-in behavior, as shown in Fig. 7.3, as the flutter frequency does not shift to f_g (i.e. $f_\theta \neq f_g$). This contrasts with the previously studied transverse-gust response, where a clear lock-in band emerged when $f_g \approx f_{\theta,0}$. Figure 7.4 shows the longitudinal gust response at $f_g = 3.5$ Hz. Similar to Fig. 7.2, weak beating in the time history but a strong spectral beating peak in PSD are observed. The gust peak is still essentially absent.

A summary of the frequency sweep at $U_\infty = 10$ m/s is shown in Fig. 7.5(a). All three trends are fundamentally unchanged along the frequency sweep, confirming the absence of 1:1 lock-in under longitudinal gusts. For comparison, Fig. 7.5(b) shows the frequency sweep under transverse gusts at $U_\infty = 10$ m/s. The lock-in band is determined by the frequency entrainment ($f_\theta = f_g$) and σ_θ drop, which are clearly observed around $f_{\theta,0}$ in Fig. 7.5(b) but absent in Fig. 7.5(a). Moreover, within lock-in, $\bar{\theta}$ slightly drops first, increases afterwards, and reaches a plateau around 41°. This amplitude plateau can also be seen in Fig. 6.2(a) with no gust. For gust cases associated with smaller $\bar{\theta}_0$, such as $U_\infty = 7$ and 8 m/s, the $\bar{\theta}$ increases monotonically within the lock-in band. The existence of the plateau indicates that the constant amplitude limitation of stall flutter occurs for both the no-gust case and the gust-induced lock-in case.

As discussed in the last chapter, the transverse gust acts as an external force to the stall flutter system, adding a forcing term to the right-hand side of the aeroelastic system. Given that the longitudinal gust directly varies the streamwise component of the airflow,

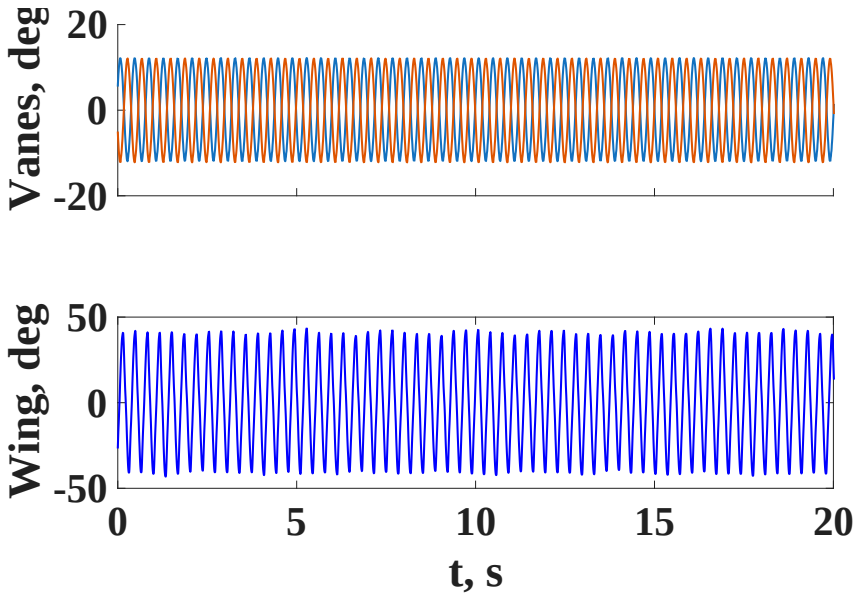

(a)

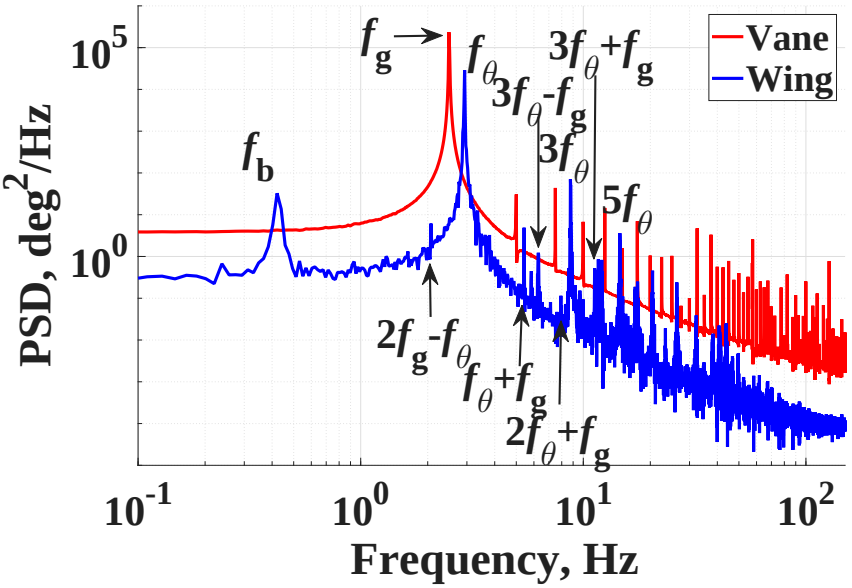

(b)

Figure 7.2: Time history (a) and PSD plots (b) for anti-phase oscillating vanes and pitching wing with $f_g = 2.5$ Hz and $f_{\theta,0} = 2.93$ Hz at $U_\infty = 10$ m/s.

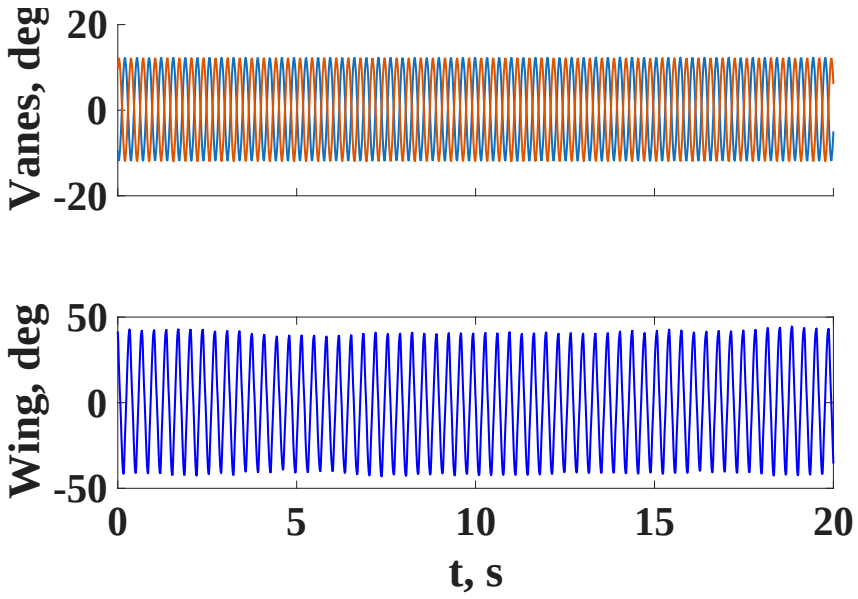

(a)

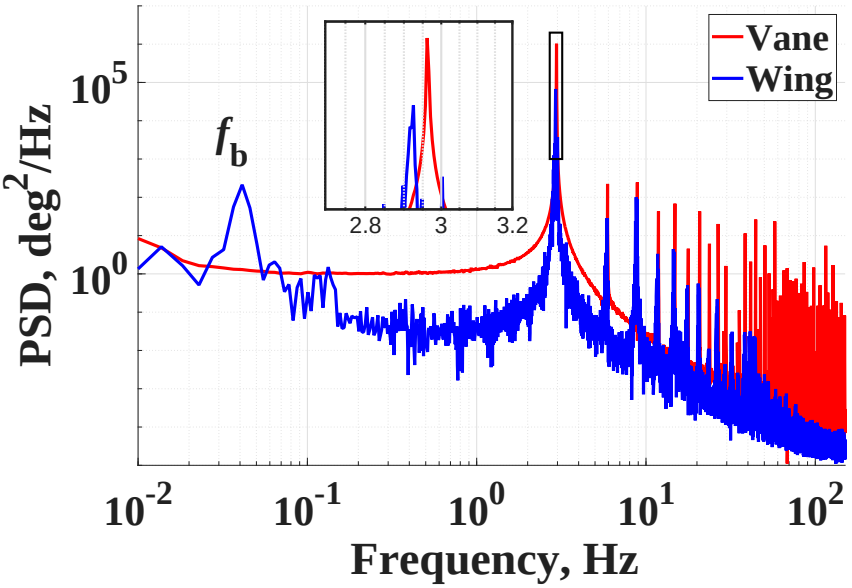

(b)

Figure 7.3: Time history (a) and PSD plots (b) for anti-phase oscillating vanes and pitching wing with $f_g = 2.96$ Hz and $f_{\theta,0} = 2.93$ Hz at $U_\infty = 10$ m/s.

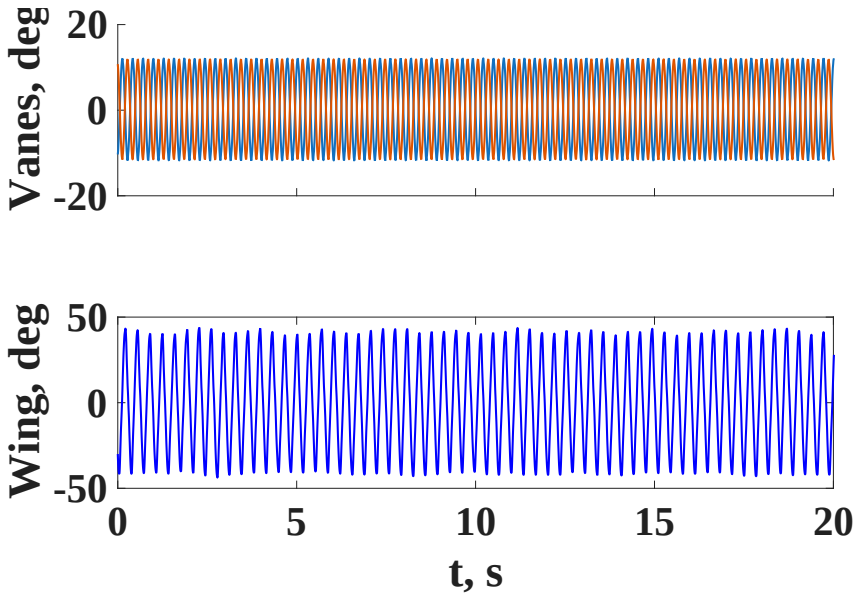

(a)

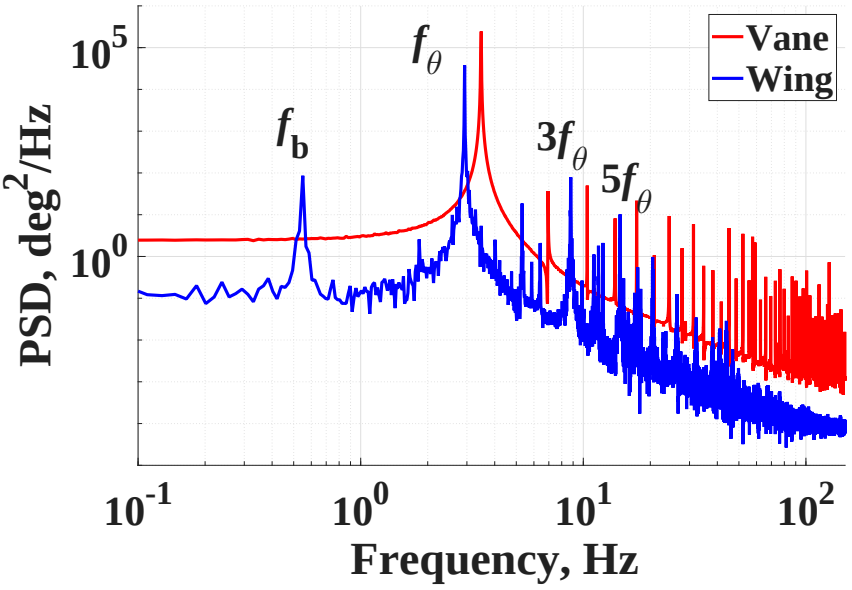

(b)

Figure 7.4: Time history (a) and PSD plots (b) for anti-phase oscillating vanes and pitching wing with $f_g = 3.5$ Hz and $f_{\theta,0} = 2.93$ Hz at $U_\infty = 10$ m/s.

which is embodied in the aerodynamic stiffness and damping terms on the left-hand side of the aeroelastic system for the classical aeroelasticity [31], it is thus inferred that the longitudinal gust, present in this chapter, also excites the nonlinear stall flutter system through a parametric modulation mechanism. Based on this inference, the lock-in band for this nonlinear parametric modulation system is thought to occur around the 2:1 zone instead of the 1:1 zone [74].

To validate the existence of the 2:1 lock-in band, the gust frequency must reach around 6 Hz, which is unfortunately beyond the capability of the present gust generator. Alternatively, the structural stiffness of the flutter rig is reduced to half, which results in a natural flutter frequency $f_{\theta,0} = 1.87$ Hz at $U_\infty = 7$ m/s without gust. Repeating the frequency sweep and covering both 1:1 and 2:1 zones, the results are summarized in Fig. 7.6. Clear evidence of a 2:1 lock-in band is confirmed by the observations, including f_θ aligned to $\frac{1}{2}f_g$, monotonically increasing $\bar{\theta}$, and an apparent drop of σ_θ. The lock-in bandwidth is roughly 0.5 Hz. Combining Figs. 7.5 and 7.6, despite different excitation mechanisms of transverse and longitudinal gusts, both configurations share key features in common: f_θ and $\bar{\theta}$ remain constant with their values close to the no-gust levels ($f_{\theta,0}$ and $\bar{\theta}_0$) when out of lock-in; the lock-in trend of $\bar{\theta}$ is asymmetric, i.e., dropping at the lower boundary and peaking at the higher boundary (or flatten if reaching the amplitude plateau).

Table 7.1 summarizes the primary experimental features of stall flutter excited by longitudinal gusts, and compares them with the primary features of transverse gusts from Chapter 6. The comparison confirms that longitudinal gusts induce parametric excitation, that is, the governing system remains homogeneous (no external forcing term on the right-hand side) but with harmonically modulated coefficients, which aids in reduced-order model development.

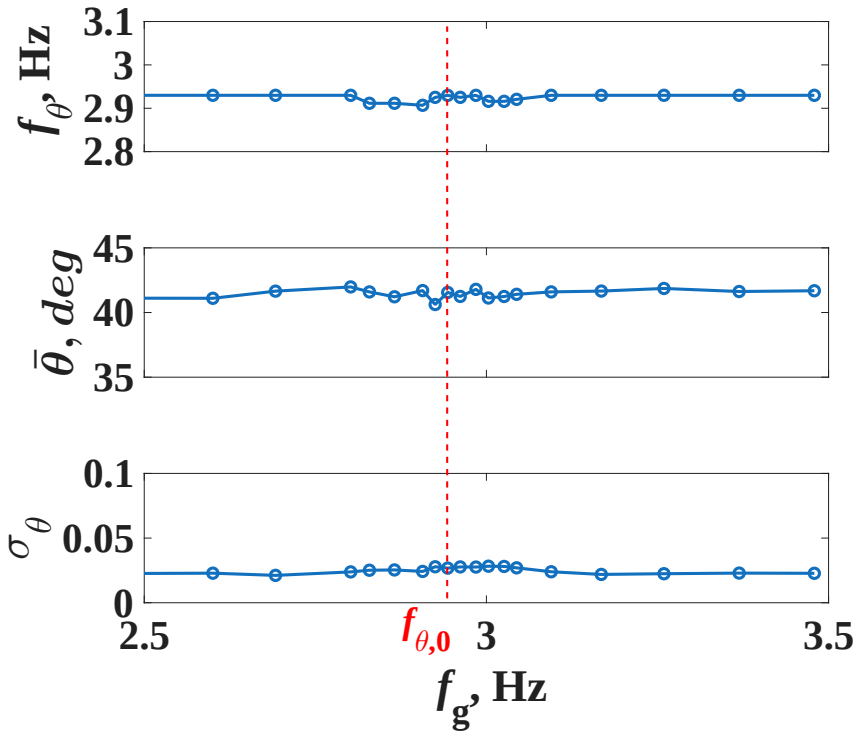

(a)

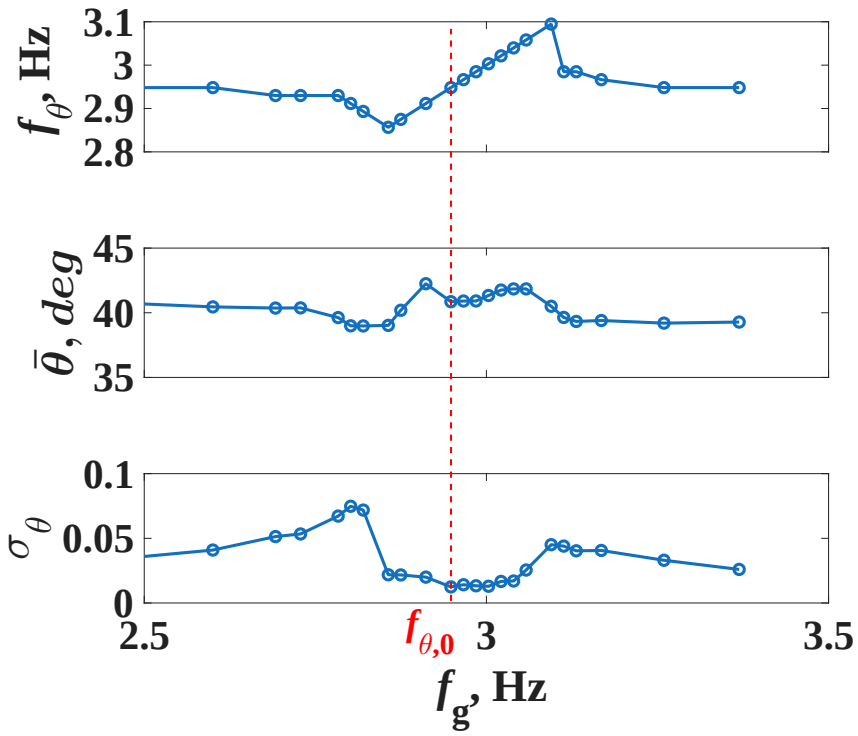

(b)

Figure 7.5: Aeroelastic response of stall flutter at $U_\infty = 10$ m/s, $f_{\theta,0} = 2.93$ Hz with frequency sweeps of (a) longitudinal gusts; (b) transverse gusts.

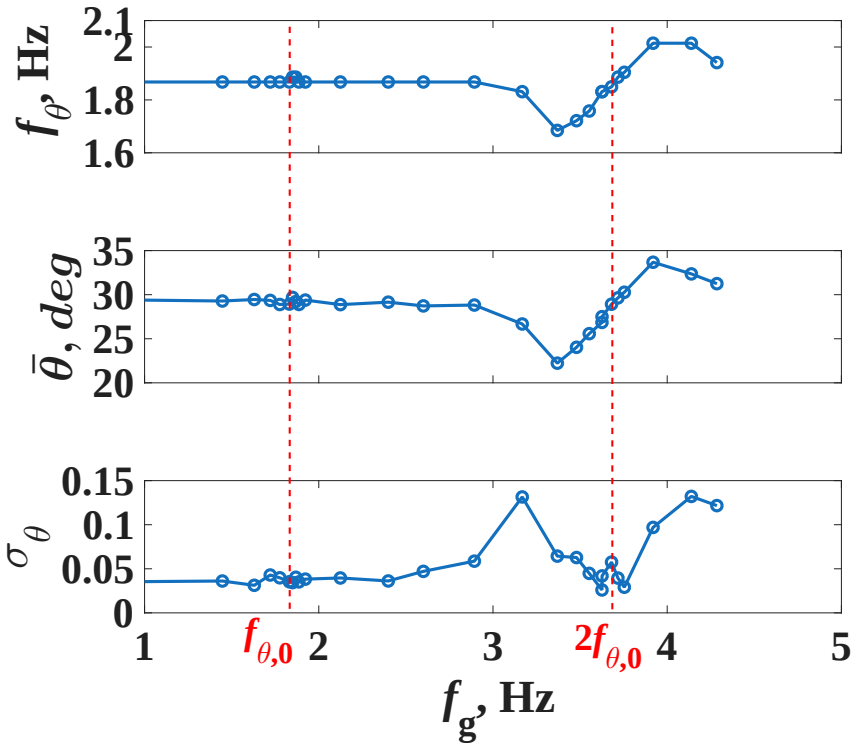

Figure 7.6: Aeroelastic response of stall flutter with frequency sweeps of longitudinal gusts at $U_\infty = 7$ m/s, $f_{\theta,0} = 1.87$ Hz.

Table 7.1: Qualitative comparison of spectral features and lock-in behavior for longitudinal (LG) and transverse (TG) gusts.

Feature	**LG**	**TG**
Spectral peak at f_g	invisible	distinct
Spectral peak at f_b	distinct	invisible
Lock-in band	2:1	1:1

7.2 Interpretation Using Mathieu-Type van der Pol Model

The foregoing experiments point to a parametric excitation mechanism; accordingly, classical theories for Mathieu-type systems provide a natural framework to interpret the effect of longitudinal gusts on stall flutter. The stall flutter oscillation itself under uniform freestream conditions, being self-sustained, can be represented phenomenologically by a VdP oscillator [70].

7.2.1 Aerodynamic stiffness simplification

Before proposing a minimal model, how a longitudinal gust, $U(t) = U_\infty + u_g(t)$, modulates the system needs to be identified. In the canonical VdP oscillator, the nonlinearity resides in the state-dependent damping. To capture the parametric action of the streamwise gust, a modulation of the effective pitch stiffness is introduced, and the damping modulation will be discussed later. Classical aeroelasticity predicts that the aerodynamic stiffness felt by a lifting surface in pitch scales quadratically with the freestream speed [8], [31], [98]. At the most basic level, aerodynamic pressure scales as $q = \frac{1}{2}\rho U^2$, and the linearized moment response to a small angular displacement contains a stiffness-like term proportional to q (times appropriate geometry/aerodynamic derivatives). Consequently, if a longitudinal (streamwise) gust induces a small relative speed variation

$$U(t) = U_\infty\big[1 + \varepsilon_g \cos(\omega_g t)\big],$$

where $\varepsilon_g = GR_u$ from Chapter 4, the aerodynamic stiffness inherits a parametric dependence through

$$K_a(t) \;\propto\; U(t)^2 \;=\; U_\infty^2\big[1 + \varepsilon_g \cos(\omega_g t)\big]^2.$$

Expanding the square shows what this injects into the pitch equation:

$$\big[1+\varepsilon_g\cos(\omega_g t)\big]^2 \;=\; 1 \;+\; 2\varepsilon_g\cos(\omega_g t) \;+\; \frac{\varepsilon_g^2}{2}\Big[1+\cos(2\omega_g t)\Big].$$

Three ingredients appear: (i) a small constant stiffening $+\frac{\varepsilon_g^2}{2}$, (ii) a dominant tone at ω_g of order $\mathcal{O}(\varepsilon_g)$, and (iii) a weaker tone at $2\omega_g$ of order $\mathcal{O}(\varepsilon_g^2)$.

Considering small-moderate gust intensities, $\varepsilon_g \ll 1$, the following practical simplification is adopted:

- The parametric stiffness with a single-tone modulation is modeled as

  $$\big[1+\varepsilon\cos(\omega_g t)\big]\,x,$$

  where x is the normalized pitch angle and $\varepsilon \;\approx\; 2\,\varepsilon_g$.

- The constant stiffness term, $+\varepsilon_g^2/2$, produces only a small upward shift of the carrier frequency, $\omega_{0,\text{eff}} \approx \omega_0(1+\varepsilon_g^2/4)$, which is higher order and negligible at the gust levels considered (~ 0.1).

- The $2\omega_g$ tone has amplitude $\mathcal{O}(\varepsilon_g^2)$ and yields much weaker second-order sidebands.

Therefore, the single-tone parametric form $\big[1+\varepsilon\cos(\omega_g t)\big]\,x$ captures the leading-order physics while keeping the derivation compact and transparent.

Stall flutter under longitudinal gusts is modeled by the conventional Mathieu-type van der Pol (M-VdP) equation with stiffness modulation and no external forcing:

$$\boxed{\ddot{x}-\mu\big(1-x^2\big)\dot{x}+\omega_0^2\big[1+\varepsilon\cos(\omega_g t)\big]\,x=0, \qquad |\varepsilon|\ll 1, 0<\mu\ll 1}, \tag{7.1}$$

where $x = \frac{\theta}{\theta_0}$ is the normalized pitch angle, ω_0 is the natural flutter frequency (no-gust), and μ is the effective aeroelastic damping parameter governing the nonlinearity strength. For the detailed derivation linking this oscillator to the physical aeroelastic pitch

equations, the reader is referred to Section 6.3.1. Throughout, $\dot{(\,)}$ denotes time derivatives in dimensional time t. Compared with Eq. (6.4), Eq. (7.1) employs dimensional time derivatives to facilitate the discussions regarding spectral content and reduces notation to ease the derivation. Both representations share the same underlying van der Pol oscillator structure, and thus, they can be readily interconverted.

Modulation of the aerodynamic damping is neglected in Eq. (7.1) since the damping force is scaled by the small parameter μ. Any parametric variation in damping would scale as $\mathcal{O}(\mu\varepsilon)$, rendering it a significantly weaker coupling mechanism compared to the dominant stiffness modulation of order $\mathcal{O}(\varepsilon)$, especially considering the complexity of damping modulation that would attribute to the nonlinear state-dependent damping term, $-\mu\big[1+\varepsilon_g\cos(\omega_g t)\big]\left(1-x^2\right)\dot{x}$. Thus, instead of laborious analytical derivation, the damping modulation will be studied using numerical results in Section 7.2.4.

Equations of this form, a self-excited van der Pol oscillator with a parametrically modulated stiffness, are classical canonical models for 2:1 parametric resonance and Mathieu-type synchronization, and have been analysed extensively in the nonlinear dynamics studies, e.g. [99] and [100], where the emphasis is on a systematic analytical classification of periodic and quasiperiodic responses over broad parameter ranges. In the present study, the same canonical structure is adopted, but with a different emphasis. The derivations developed below are deliberately minimal and tailored to the present aeroelastic problem: only the spectral and averaged amplitude-phase relations are retained to interpret the observed sidebands and 2:1 lock-in band in stall flutter under longitudinal gusts. In this sense, the analysis below is not intended as a complete mathematical classification of the M-VdP dynamics, but as a problem-driven reduction tailored to interpret the preceding experimental observations.

7.2.2 Spectral content analysis away from lock-in

To understand the system's spectral signature, the autonomous case is firstly considered by setting the parametric excitation to zero ($\varepsilon = 0$). The model reduces to the classical van der Pol oscillator, which is known to exhibit a stable limit cycle. The carrier frequency of this autonomous oscillation, ω_θ, is given by:

$$\omega_\theta = \omega_0 + \mathcal{O}(\mu^2), \tag{7.2}$$

This represents the primary response frequency, which experiences a minor, higher-order shift from the linear natural frequency ω_0. The nonlinear damping term, $-\mu(1-x^2)\dot{x}$, is an odd function of x, resulting in a limit cycle $x_0(t)$ that is, to leading order, half-wave symmetrical. This symmetry suppresses the even Fourier components. Consequently, the autonomous response spectrum consists predominantly of the fundamental frequency ω_θ and its odd harmonics:

$$x_0(t) = c_1 \cos(\omega_\theta t) + c_3 \cos(3\omega_\theta t) + c_5 \cos(5\omega_\theta t) + \cdots, \qquad c_{2k} \approx 0. \tag{7.3}$$

Now the parametric excitation is introduced by treating ε as a small perturbation parameter. A standard perturbation expansion for the solution $x(t)$ is employed:

$$x(t) = x_0(t) + \varepsilon x_1(t) + \varepsilon^2 x_2(t) + \cdots. \tag{7.4}$$

Substituting this expansion into Eq. (7.1) and collecting terms at the first order, $\mathcal{O}(\varepsilon)$, yields the equation for the first correction, $x_1(t)$. With the linear operator $\mathcal{L} \equiv \frac{d^2}{dt^2} + \omega_0^2$, this equation is

$$\mathcal{L}\, x_1 = -\,\omega_0^2 \cos(\omega_g t)\, x_0. \tag{7.5}$$

The right-hand side of Eq. (7.5) acts as a multiplicative forcing term. This term causes

frequency mixing between the gust, $\cos(\omega_g t)$, and the autonomous response, $x_0(t)$. Applying the trigonometric identity $\cos\alpha\cos\beta = \frac{1}{2}[\cos(\alpha+\beta)+\cos(\alpha-\beta)]$, each odd carrier harmonic $m\omega_\theta$ in x_0 interacts with ω_g to generate a pair of first-order sidebands at:

$$\omega_{m,\pm}^{(1)} = m\omega_\theta \pm \omega_g, \qquad m = 1, 3, 5, \ldots . \tag{7.6}$$

The magnitude of these sidebands scales linearly with the perturbation, $\propto \varepsilon$.

This recursive process continues at higher orders. At $\mathcal{O}(\varepsilon^2)$, the first-order solution x_1, which contains the sidebands from Eq. (7.6), is in turn multiplied by the parametric term $\cos(\omega_g t)$:

$$\mathcal{L}\, x_2 = -\,\omega_0^2 \cos(\omega_g t)\, x_1 \;+\; (\text{weak VdP cross-terms}). \tag{7.7}$$

This secondary mixing generates the second-order sidebands:

$$\omega_{m,\pm}^{(2)} = m\omega_\theta \pm 2\omega_g, \qquad m = 1, 3, 5, \ldots . \tag{7.8}$$

These components have magnitudes scaling as $\propto \varepsilon^2$. Generalizing to $\mathcal{O}(\varepsilon^n)$, this parametric cascade generates a full lattice of sidebands at $\omega_{m,\pm}^{(n)} = m\omega_\theta \pm n\omega_g$.

Thus, for the non-resonant case (away from lock-in), the predicted spectral content is characterized by three key features:

- *Odd Carrier Harmonics:* The fundamental frequency ω_θ and its odd multiples ($m = 1, 3, 5, \ldots$), originating from the underlying van der Pol dynamics.
- *Parametric Sideband Lattice:* A symmetrical lattice of sidebands, $\omega = m\omega_\theta \pm n\omega_g$ ($n = 1, 2, \ldots$), surrounding each carrier harmonic. The amplitude of the n-th order sideband is expected to scale as $\propto \varepsilon^{\,n}$.
- *Absence of Gust-Frequency Peak:* A critical distinction of this parametric model is

the absence of an isolated spectral peak at the gust frequency ω_g itself. Because the excitation is multiplicative (not additive), the ω_g component only appears as part of the mixed sideband pairs (e.g., $\omega_\theta \pm \omega_g$) unless an external forcing at ω_g is present.

7.2.3 Lock-in band

Introducing nondimensional time $\tau = \omega_0 t$, frequency ratio $\Omega = \omega_g/\omega_0$, and normalized damping $\tilde{\mu} = \mu/\omega_0$ to Eq. (7.1) yields the nondimensional M-VdP model:

$$x'' - \tilde{\mu}(1 - x^2)\, x' + \big[1 + \varepsilon \cos(\Omega\tau)\big] x = 0, \tag{7.9}$$

where $(\,)'$ denotes the derivative with respect to τ. This nondimensional framework facilitates the application of the averaging method and the subsequent analysis of lock-in.

7.2.3.1 Averaging procedure

Considering the principal parametric resonance $\Omega \approx 2$, let $\delta = \Omega - 2 = \mathcal{O}(\varepsilon)$ represent the small detuning from exact resonance. To capture the dynamics, we recognize two distinct timescales: the 'fast time' τ, which tracks the natural oscillation of the structure, and the 'slow time', over which the amplitude and phase modulation evolve due to the weak parametric perturbation. The method of averaging [101] is employed to separate these scales. Adopt the near-harmonic representation with slowly varying amplitude $r(\tau)$ and phase $\phi(\tau)$:

$$x(\tau) = r(\tau)\cos(\tau + \phi), \qquad \psi(\tau) = \tau + \phi - \frac{\Omega}{2}\tau, \tag{7.10}$$

where ψ is the phase difference, or mismatch, between the oscillator's phase $(\tau + \phi)$ and the effective parametric forcing phase $(\Omega\tau/2)$. Assume $r' = O(\tilde{\mu}, \varepsilon)$ and $\phi' = O(\tilde{\mu}, \varepsilon)$;

then

$$\begin{aligned} x' &= r'\cos(\tau+\phi) - r(1+\phi')\sin(\tau+\phi), \\ x'' &\approx -r(1+\phi')^2\cos(\tau+\phi) - 2r'(1+\phi')\sin(\tau+\phi), \end{aligned} \tag{7.11}$$

where r'' and ϕ'' are higher order and are dropped. Substituting Eqs. (7.10) and (7.11) into Eq. (7.9), and applying the standard averaging procedure—projecting onto the basis functions $\cos(\tau+\phi)$ and $\sin(\tau+\phi)$ and integrating over one cycle (2π) of the fast time τ—filters out the rapidly oscillating terms and isolates the secular terms that drive the slow dynamics; see classical nonlinear dynamics textbooks such as [74], [70], and [101] for more details. Finally, utilizing the kinematic relationship $\psi' = \phi' - \delta/2$, the system is transformed into the variables r and ψ. This yields the slow-flow equations (a dynamical systems term referring to the flow of trajectories in the reduced phase space, rather than physical fluid motion), which govern the long-term evolution of the system:

$$r' = \frac{1}{2}\tilde{\mu}r - \frac{1}{8}\tilde{\mu}r^3 + \frac{1}{4}\varepsilon r\sin(2\psi), \tag{7.12}$$

$$\psi' = -\frac{1}{2}\delta + \frac{1}{4}\varepsilon\cos(2\psi). \tag{7.13}$$

Equations (7.12) and (7.13) constitute the coupled slow-flow system governing the interaction between stall flutter and longitudinal gusts. Physically, the first two terms in Eq. (7.12), $\frac{1}{2}\tilde{\mu}r$ and $-\frac{1}{8}\tilde{\mu}r^3$, represent the autonomous flutter mechanism, specifically, the competition between linear negative damping (energy input) and cubic nonlinear damping (saturation). The terms proportional to ε in both equations capture the impact of the parametric excitation. Synchronization, or lock-in, occurs when the parametric forcing is strong enough to overcome the frequency detuning δ, resulting in a stationary amplitude and a constant phase difference.

7.2.3.2 Lock-in boundary

Steady (phase-locked) solutions satisfy $r' = \psi' = 0$, hence

$$\cos(2\psi) = \frac{2\delta}{\varepsilon}, \qquad \sin(2\psi) = \frac{1}{\varepsilon}\Big(\frac{\tilde{\mu}}{2}\, r^2 - 2\tilde{\mu}\Big), \tag{7.14}$$

and eliminating ψ gives the existence boundary

$$\varepsilon^2 = 4\delta^2 + \Big(\frac{\tilde{\mu}}{2}\, r^2 - 2\tilde{\mu}\Big)^2. \tag{7.15}$$

For the autonomous VdP LCO, $\frac{\tilde{\mu}}{2}\, r^2 - 2\tilde{\mu} = 0$ so $r_0 = 2$; evaluating at $r = r_0$ removes the amplitude term and yields the half-width in detuning,

$$|\delta|_{\max} = \frac{1}{2}\varepsilon \qquad \Longleftrightarrow \qquad |\Omega - 2|_{\max} = \frac{1}{2}\varepsilon. \tag{7.16}$$

Mapping back to dimensional frequencies ($\Omega = \omega_g/\omega_0$) gives

$$\boxed{|\omega_g - 2\omega_0|_{\max} = \frac{1}{2}\varepsilon\, \omega_0.} \tag{7.17}$$

This result indicates that the synchronization bandwidth scales linearly with the modulation strength ε and the natural frequency ω_0. Importantly, to the leading order, this width is independent of the autonomous limit-cycle amplitude r_0 (and thus the baseline pitch angle $\overline{\theta}_0$), a feature that distinguishes this parametric mechanism from the classical forced Van der Pol oscillator. These analytical predictions are next verified against numerical solutions of the full system.

7.2.4 Analytico-numerical verification

All derivations in Sections 7.2.1–7.2.3 assume small ε. To test the predictions and delineate the validity range of ε, the M-VdP model in Eq. (7.1) is solved numerically. The

Table 7.2: Representative sidebands written as $f_{m,\pm}^{(n)} = m\, f_\theta \pm n\, f_g$, corresponding to the labels in Fig. 7.7(b).

Coefficient	f_0	f_1	f_2	f_3	f_4	f_5	f_6
m (f_θ)	$+1$	-1	$+3$	$+1$	$+3$	$+1$	$+3$
n (f_g)	-1	$+2$	-2	$+1$	-1	$+2$	$+1$

experimental case in Fig. 7.2 is reproduced with $f_g = 2.5$ Hz, $f_{\theta,0} = 2.93$ Hz, $\bar{\theta}_0 = 41°$, and $\varepsilon = 0.2$. As for the damping parameter $\tilde{\mu}$, it dictates the slow time scale of amplitude evolution, see Eq. (7.12), which has a negligible effect on the steady-state frequency and amplitude [70], [74]. Consequently, $\tilde{\mu}$ mainly affects the transient period, which is set to 0.1 throughout all numerical simulations. The time history in Fig. 7.7(a) shows stronger amplitude modulation than the experimental result in Fig. 7.2(a). In experiments, there is an amplitude convergence of stall flutter (approximately 41°) shown in Figs. 6.2(a) and 7.5(b), which naturally limits the beating amplitude. The amplitude convergence is a higher-order aeroelastic nonlinearity which is not captured in this minimal model. The PSD in Fig. 7.7(b) exhibits primary carriers at mf_θ (odd m) together with modulation sidebands at $|mf_\theta \pm nf_g|$ ($n = 1, 2, 3, \ldots$). Selected components are labeled and summarized as $f_{m,\pm}^{(n)} = mf_\theta \pm nf_g$ in table 7.2. These sidebands match the experimental observation in Fig. 7.2(b) and support the derivation in Section 7.2.2.

A sweep in f_g using the M-VdP model (Fig. 7.8) reveals no 1:1 lock-in near $f_g \approx f_{\theta,0}$ but a clear 2:1 synchronization band, consistent with the classical Mathieu-type parametric resonance and also the experimental observations shown in Fig. 7.6. Note that the M-VdP parameters, such as $f_{\theta,0}$ and $\bar{\theta}_0$, are adjusted to phenomenologically match the experimental sweep capturing the 2:1 lock-in zone. In addition, the modulation strength is physically calibrated to $\varepsilon = 0.26$, derived from the flow measurement using the X-hot-wire probe, which indicated $u_{g,max} = 1.3$ m/s at $f_g = 3.9$ Hz (not the ideally central frequency but within the lock-in band). With this physically constrained parameter, the numerical sweep yields a predicted lock-in bandwidth of 0.48 Hz. This result demonstrates a remark-

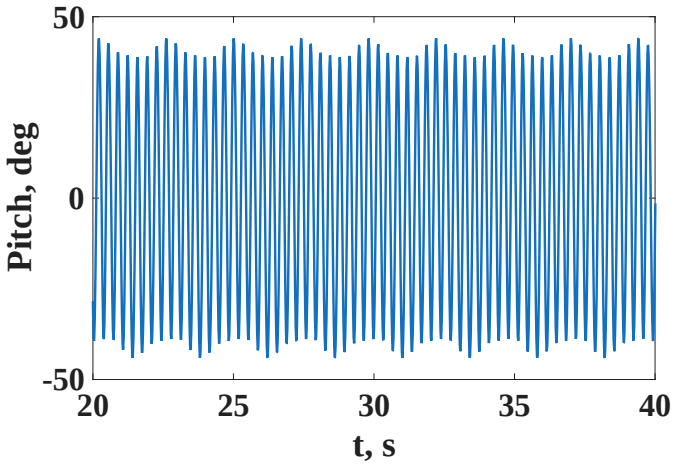

(a)

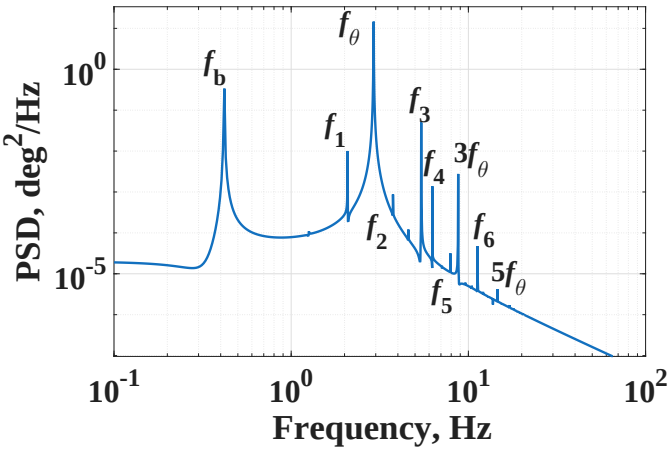

(b)

Figure 7.7: Numerical M-VdP results for $f_g = 2.5$ Hz, $f_{\theta,0} = 2.93$ Hz, $\bar{\theta}_0 = 41°$, and $\varepsilon = 0.2$: (a) time history; (b) PSD with labeled sidebands (see table 7.2), reproducing experimental results in Fig. 7.2.

able three-way quantitative agreement: it matches the analytical prediction of 0.486 Hz derived in Eq. (7.17) and aligns closely with the experimentally observed bandwidth of approximately 0.5 Hz shown in Fig. 7.6. This convergence of analytical, numerical, and experimental scales provides strong support for the validity of the proposed M-VdP model, confirming that the observed lock-in is indeed driven by the parametric stiffness modulation mechanism.

The $\bar{\theta}$ trend around the 2:1 lock-in band is symmetric for the M-VdP model, which is typical resonance performance, but asymmetric for the measured results. The measured $\bar{\theta}$ drops at the lower boundary of the 2:1 lock-in band and reaches the peak at the higher boundary. A similar mismatch was also reported in the previous study on transverse gusts in Section 6.3.4. The externally forced VdP model showed symmetric amplitude trend around the 1:1 lock-in band, while the measurements exhibited a mild asymmetry, with the peak skewed toward the upper edge of the synchronization window, see Fig. 7.6.

This discrepancy suggests that subtle physical mechanisms (e.g., higher-harmonic aerodynamic contributions) lie beyond the scope of these minimal models. One such mechanism involves nonlinear aerodynamic stiffness: as seen in Fig. 5.2, the pitching moment coefficient exhibits a non-monotonic, nonlinear trend at higher angles of attack beyond static stall, suggesting that the restoring moment might be better captured by incorporating a Duffing (cubic stiffness) term. In particular, Ref. [99] reported that a forced Mathieu-van der Pol-Duffing model can produce asymmetric amplitudes of lock-in bands, similar to Fig. 7.6, but the added cubic stiffness (Duffing term) deviates the oscillation frequency from $f_{\theta,0}$ out of lock-in, which is inconsistent with the experimental observation. Nevertheless, such extensions point to a promising pathway for refining the present minimal model in future studies.

In Chapter 6, both experimental and analytical results for the transverse gusts indicated that a lower baseline LCO amplitude or a stronger external force broadens the 1:1 lock-in band. By contrast, for the present M-VdP model, Eq. (7.16), predicts that the

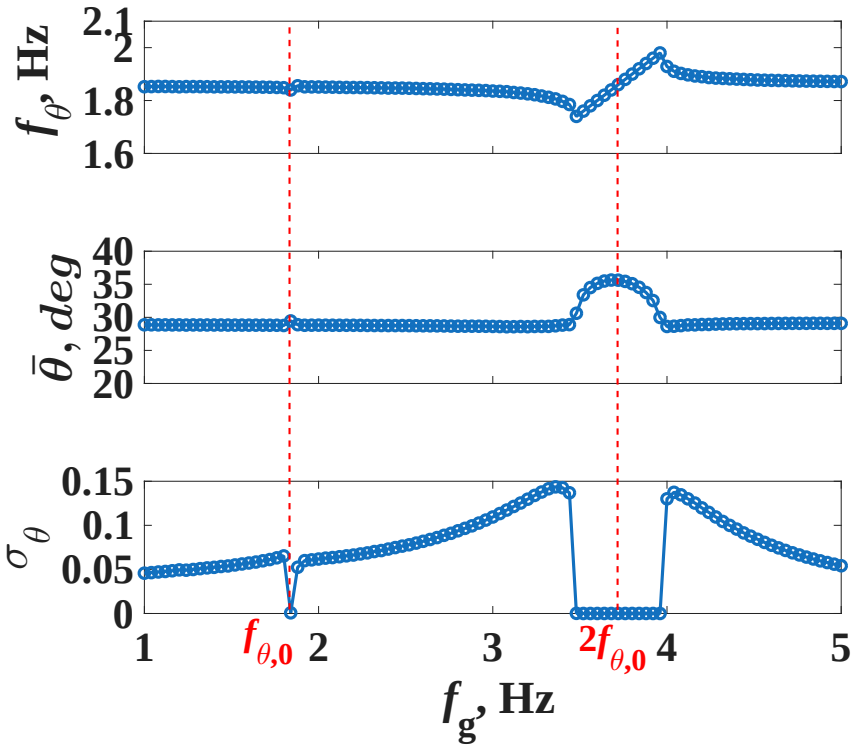

Figure 7.8: M-VdP result summary with frequency sweep of parametric excitation (covering both 1:1 and 2:1 regions), with $f_{\theta,0} = 1.87$ Hz, $\bar{\theta}_0 = 29°$, and $\varepsilon = 0.26$, reproducing experimental results in Fig. 7.6.

nondimensional parametric 2:1 bandwidth depends only on the longitudinal-gust strength, represented by ε, and is essentially independent of the baseline amplitude. These predictions are confirmed by Figs. 7.9 and 7.10, i.e., varying $\bar{\theta}_0$ leaves the band unchanged, whereas increasing ε expands it. The dimensional widths of lock-in bands are 0.18, 0.36, and 0.56 Hz for $\varepsilon = 0.1$, 0.2, and 0.3, respectively, in agreement with Eq. (7.17). For $\varepsilon = 0.3$, the response frequency deviates more noticeably from $f_{\theta,0}$, reflecting stronger nonlinear effects of the greater modulation.

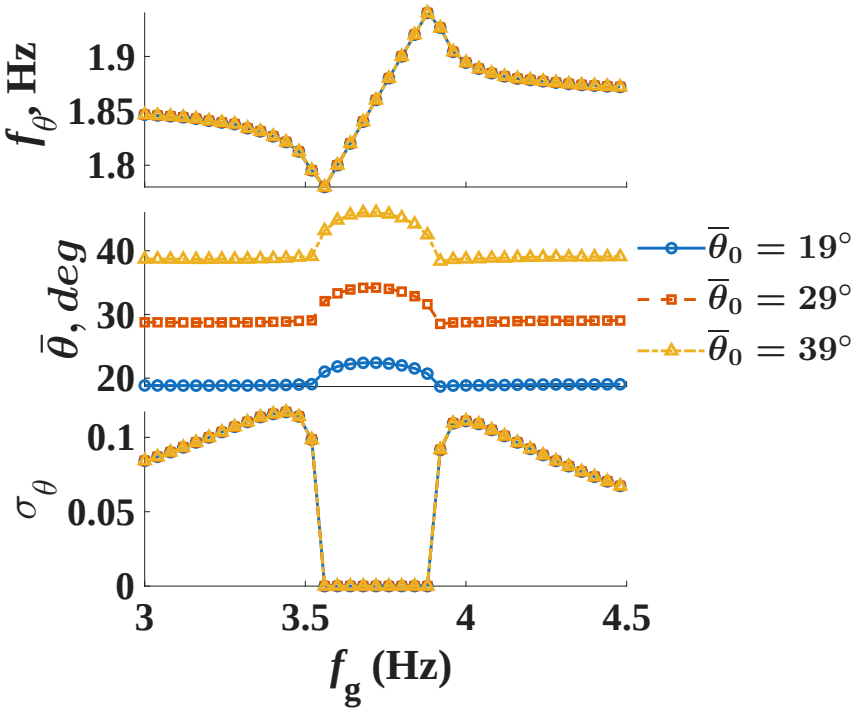

Figure 7.9: Effect of baseline amplitude around the 2:1 region: $f_{\theta,0} = 1.87$ Hz, $\varepsilon = 0.2$, and $\bar{\theta}_0 = 19°, 29°, 39°$.

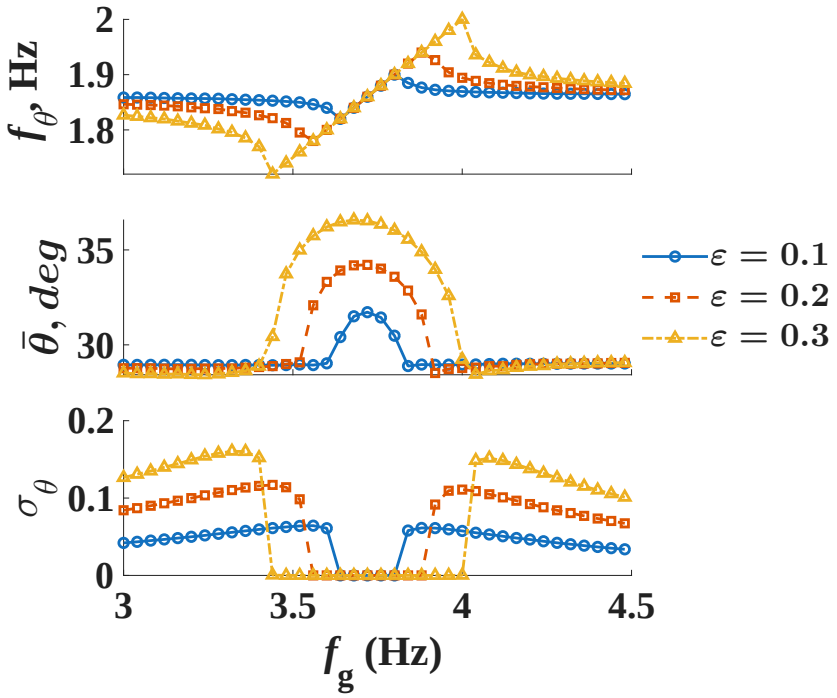

Figure 7.10: Effect of stiffness modulation strength around the 2:1 region: $f_{\theta,0} = 1.87$ Hz, $\bar{\theta}_0 = 29°$, and $\varepsilon = 0.1, 0.2, 0.3$.

Revisiting the 1:1 region in Figs. 7.5(a), 7.6 (experiment), and 7.8 (M-VdP), subtle frequency fluctuations near $f_g \approx f_{\theta,0}$ hint at the presence of a weak interaction. To determine whether stronger parametric modulation could induce 1:1 synchronization in the M-VdP model, numerical sweeps are conducted with modulation strength ε ranging from 0.05 to 0.6. Figure 7.11 confirms that while low modulation strengths result in quasi-periodic beating (implied by non-zero σ_θ), a sufficiently large ε yields definitive 1:1 lock-in. This high-modulation synchronization is a strictly nonlinear phenomenon not captured by the first-order perturbation analysis, thus outside the scope of Sections 7.2.1–7.2.3.

Figure 7.12 presents the global synchronization map in the (f_g, ε) plane. These boundaries are determined numerically using the frequency matching criteria of $f_\theta = f_g$ for the 1:1 zone and $f_\theta = \frac{1}{2} f_g$ for the 2:1 zone. The resulting synchronization regions, classically referred to as Arnold tongues, after V. I. Arnold [73], exhibit two qualitatively distinct behaviors. First, the primary 2:1 parametric lock-in zone forms a sharp V-shaped wedge originating from $\varepsilon = 0$. The numerical boundaries in this region demonstrate excellent agreement with the analytical prediction derived in Eq. (7.17), verifying the validity of the averaging method used to derive the lock-in criteria. Second, the 1:1 lock-in zone exhibits a detached tongue structure. Unlike the 2:1 resonance, the 1:1 synchronization requires a finite threshold of modulation strength ($\varepsilon > 0.2$) to manifest. Below this threshold, the parametric energy input is insufficient to overcome the detuning. This contrast underscores the different physical mechanisms at play: the 2:1 resonance is the primary instability of the Mathieu-type term, whereas the 1:1 lock-in is a higher-order nonlinear effect. Experimentally, generating the large modulation amplitudes required to observe 1:1 lock-in is beyond the current apparatus capabilities, suggesting a compelling direction for future work.

Finally, to justify the exclusion of damping modulation in the primary model, Eq. (7.9), numerical simulations are conducted using an alternative formulation where the gust modulates the damping rather than the stiffness. Assuming the aerodynamic damping

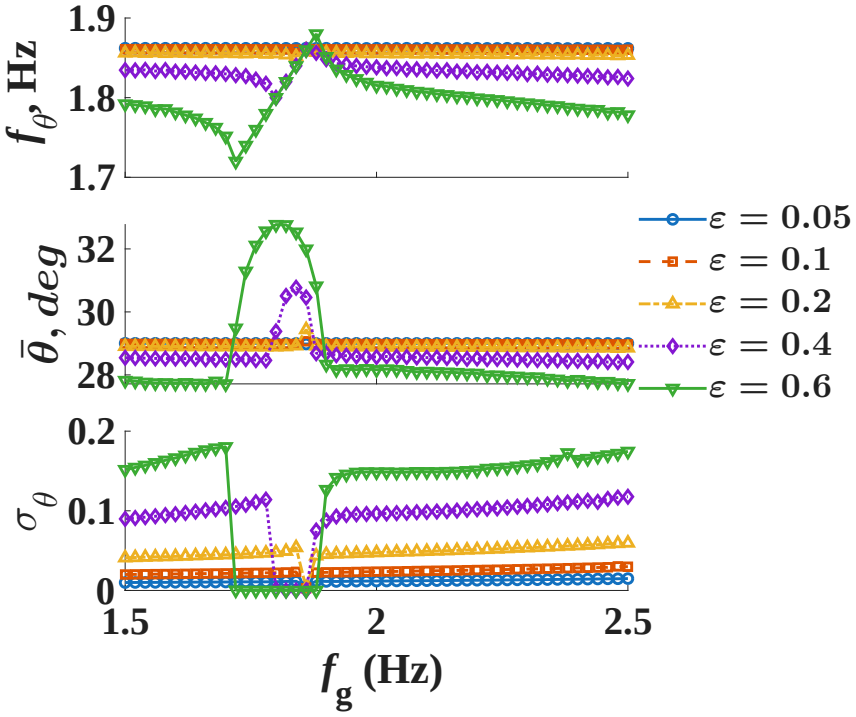

Figure 7.11: Numerical frequency sweep around the 1:1 region for larger stiffness modulation: $f_{\theta,0} = 1.87$ Hz, $\bar{\theta}_0 = 29°$, and $\varepsilon = 0.05, 0.1, 0.2, 0.4, 0.6$.

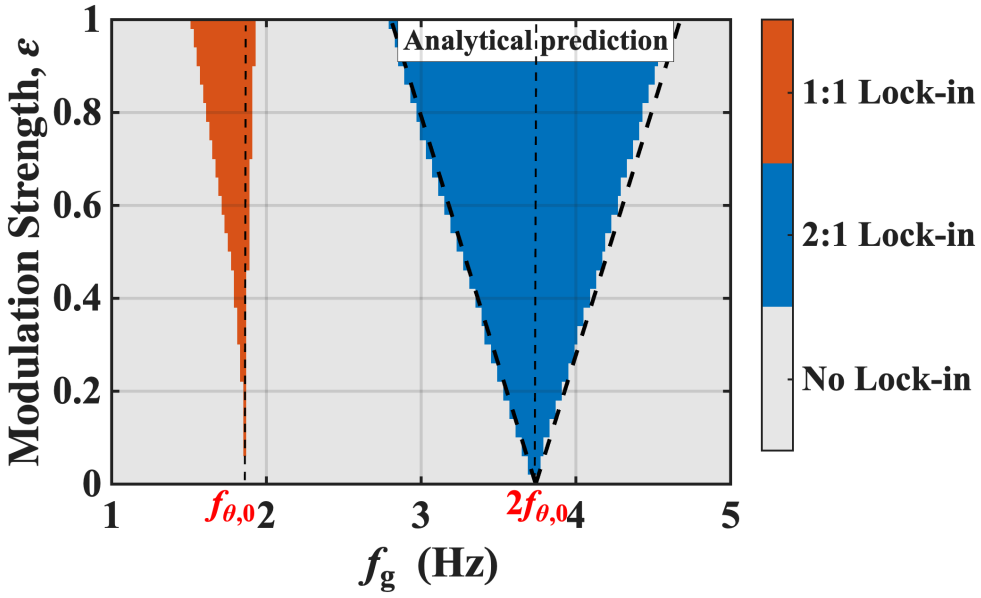

Figure 7.12: Map of synchronization regions (Arnold tongues) for the M-VdP model with stiffness modulation, Eq. (7.9), ($f_{\theta,0} = 1.87$ Hz, $\bar{\theta}_0 = 29°$): 2:1 parametric lock-in (blue) and 1:1 lock-in (red, emerging at higher modulation strengths). The black dashed lines represent the analytical prediction for the 2:1 boundary derived in Eq. (7.17).

inherits the parametric dependence through $D_a(t) \propto U(t) = U_\infty[1+\varepsilon_g \cos(\omega_g t)]$, Eq. (7.9) is modified as:

$$x'' - \tilde{\mu}\big[1 + \varepsilon_g \cos(\Omega\tau)\big](1 - x^2)\, x' + x = 0. \tag{7.18}$$

The resulting synchronization boundaries, shown in Fig. 7.13, reveal a lock-in bandwidth that is significantly narrower than that of the stiffness modulation case (Fig. 7.12). Note that considering the scaling relation $\varepsilon_g = \varepsilon/2$, the difference in bandwidth is even more pronounced than it appears. This reduced bandwidth is consistent with the scaling analysis in Section 7.2.1: the parametric damping term scales as $\mathcal{O}(\tilde{\mu}\varepsilon)$, rendering it a significantly weaker coupling mechanism than the stiffness modulation of order $\mathcal{O}(\varepsilon)$. Furthermore, the numerical amplitude trend for damping modulation (Fig. 7.14) exhibits a symmetric profile, but with a slight increase at lock-in boundaries and a distinct dip in $\bar{\theta}$ (lower than $\bar{\theta}_0$) near the resonance condition $f_g \approx 2f_\theta$, which are contrary to the experimental observations (slight drop at the lower boundary and peak at the upper boundary with the peaking level higher than $\bar{\theta}_0$). These discrepancies denote that damping modulation might not capture the correct physics of the gust interaction, and the dominant physics of longitudinal gust excitation on stall flutter originates from the parametric stiffness modulation.

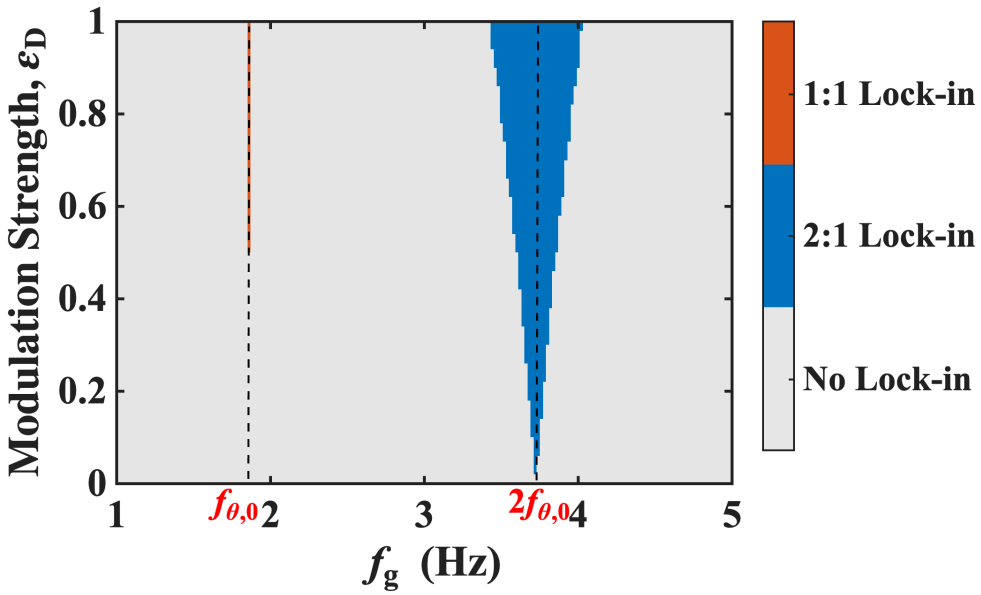

Figure 7.13: Map of synchronization regions (Arnold tongues) for the M-VdP model with damping modulation, Eq. (7.18), ($f_{\theta,0} = 1.87$ Hz, $\bar{\theta}_0 = 29°$): 2:1 parametric lock-in (blue) and 1:1 lock-in (red, fundamentally invisible).

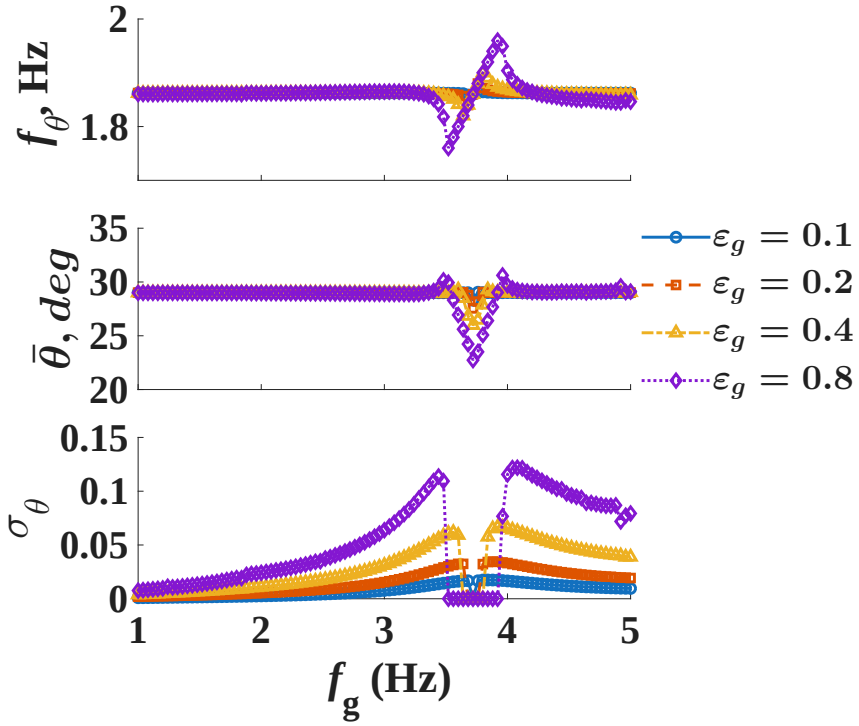

Figure 7.14: Effect of damping modulation strength: $f_{\theta,0} = 1.87$ Hz, $\bar{\theta}_0 = 29°$, and $\varepsilon_g = 0.1, 0.2, 0.4, 0.8$. Unlike the experimental observations (Fig. 7.6) and stiffness modulation results (Fig. 7.8), the response amplitude $\bar{\theta}$ exhibits a distinct dip inside the lock-in band.

Chapter 8

CONCLUSIONS

This dissertation has provided a comprehensive investigation into the aerodynamic and aeroelastic responses of a NACA0012 airfoil subjected to harmonic flow excitations at transitional Reynolds numbers ($Re_c \approx 10^5$). By integrating wind tunnel experiments, high-fidelity numerical simulations, and reduced-order phenomenological modeling, this research maps the nonlinear interactions between unsteady gust environments and structural dynamics. The following sections summarize the primary contributions and findings of this work, and also provide a plan for future work.

8.1 Aerodynamic Gust Response

The investigation of a stationary wing encountering harmonic transverse gusts revealed that while pre-stall responses align with classical linear theories (e.g., Küssner and Sears functions), transverse gusts of sufficient amplitude drive the airfoil into a deep post-stall regime.

- **Gust-induced dynamic stall:** Transverse gusts were shown to induce a dynamic stall process characterized by significant lift enhancement and aerodynamic hysteresis.
- **Qualitative analogy:** A key contribution is the identification of a qualitative analogy between gust- and pitch-induced dynamic stall. By introducing an effective

angle of attack (α_e) that incorporates the instantaneous gust-induced downwash, it was demonstrated that the upwash and downwash phases of a gust encounter are fundamentally analogous to the upstroke and downstroke phases of a pitching motion.

8.2 Numerical Insights and Flow Physics

High-fidelity numerical simulations provided a deeper understanding of the flow physics that drive the observed aerodynamic loads.

- **2D LES and cross-comparison:** 2D LES were successfully employed to assess the frozen gust hypothesis. By prescribing a constant longitudinal (u) velocity, the simulations isolate the aerodynamic contribution of the harmonic transverse (v) component and eliminate the mixed influence of the small experimental u-fluctuations.
- **Necessity of 3D LES:** While 2D LES captured the primary stall process, 3D simulations were found necessary to resolve complex stall features such as delayed vortex shedding that caused the secondary lift loop.
- **Mechanistic flow-physics interpretation:** The simulations delineated the evolution of the LEV and TEV, confirming that the delayed shedding of the LEV during the phase of decreasing α_e is the primary mechanism behind the observed secondary lift loop.

8.3 Stall Flutter Under Transverse Gust Excitation

To investigate the aeroelastic response to harmonic gusts, structural flexibility is introduced by replacing the stationary wing with the one-DOF pitch-only flutter rig. By performing in-phase motion of two gust vanes, transverse gusts are generated. They

act as an *external forcing mechanism* that interacts with self-sustained stall flutter limit cycles.

- **1:1 lock-in:** The system exhibits a finite 1:1 lock-in band where the stall flutter frequency synchronizes with the gust frequency. Outside this band, the response is characterized by quasi-periodic beating with clearly defined spectral sidebands.
- **Instability advancement:** A significant finding of this work is that transverse gusts generally advance the onset of stall flutter. This advancement follows a "wedge-like" trend centered around the natural flutter frequency under uniform flow. Near resonance, the critical airspeed for flutter onset can drop by over 35%, identifying a substantial safety risk for vehicles in unsteady urban environments.
- **Phenomenological modeling:** A forced VdP oscillator was derived from a standard one-DOF pitch-only aeroelastic model. The oscillator effectively reproduced the synchronization windows and amplitude modulation observed experimentally, which may support gust effect mitigation.

8.4 Parametric Excitation by Longitudinal Gusts

Longitudinal gusts are generated with anti-phase vane motion. In contrast to the transverse case, longitudinal (streamwise) gusts excite the aeroelastic system through the *parametric modulation* of aerodynamic parameters.

- **2:1 lock-in:** Unlike the 1:1 synchronization found in transverse gusts, longitudinal gusts drive a 2:1 lock-in band, where the flutter frequency aligns with half of the excitation frequency.
- **Spectral signatures:** A distinct spectral signature is identified: a prominent peak at the beat frequency is present, while a peak at the gust frequency itself is essentially absent.

- **Mathieu-van der Pol model:** The stall flutter dynamics under longitudinal gusts are successfully modeled using an M-VdP equation. The minimal model makes some theoretically grounded predictions beyond the constraints of the current apparatus.

8.5 Scientific and Practical Significance

The significance of the aerodynamic gust response of this research lies in the establishment of a qualitative analogy between gust- and pitch-induced dynamic stall, by demonstrating that these complex separation physics can be unified through a shared framework based on an effective angle of attack. Furthermore, the detailed experimental flow surveys and synchronous force measurements provide a high-fidelity database essential for the scientific community to validate CFD codes against complex airflow conditions that exceed the scope of traditional uniform-flow models.

The aeroelastic significance of this research is established through the critical mechanistic distinction between externally forced and parametrically excited coupling in complex flow separation scenarios. By systematically examining stall flutter under both transverse and longitudinal excitation, this work identifies fundamentally different interaction regimes: transverse gusts act as an external forcing mechanism leading to 1:1 frequency synchronization, while longitudinal gusts drive 2:1 parametric resonance through the modulation of aerodynamic stiffness. This study bridges the gap between nonlinear dynamics and aeroelasticity by importing the perturbation and averaging methods to interpret fluid-structure interactions involving large-scale flow separation, providing a baseline analytical framework to clarify energy and phase balances in such systems.

Practically, these findings provide high-fidelity experimental benchmarks and minimal modeling frameworks, specifically the forced van der Pol and Mathieu–van der Pol surrogates, for exploring the applicability and effectiveness of reduced-order models in capturing the essential dynamics of complex aeroelastic systems. The identified lock-

in bands and beating phenomena, quantified by distinct spectral signatures such as the absence of a gust-frequency peak in longitudinal cases, have direct implications for the structural safety and control of rotorcraft, UAVs, and wind turbines operating in highly unsteady inflows. Ultimately, this work offers theoretically grounded insights that support the development of robust control systems and envelope-aware load-limiting strategies for modern air vehicles in time-varying aerodynamic environments.

8.6 Future Work

The findings of this dissertation establish a mechanistic foundation for understanding gust-excited nonlinear aeroelasticity at transitional Reynolds numbers. To bridge the remaining gaps between these fundamental insights and the practical requirements of robust UAM design, several paths for future research are proposed:

- **Transition from harmonic to realistic gust profiles:** While harmonic excitations successfully isolated the underlying synchronization physics (1:1 and 2:1 lock-in), atmospheric turbulence in operational environments is inherently stochastic and discrete. Future studies should investigate the aeroelastic response to 1-cosine discrete gusts and random PSD-based turbulence. Such research would determine whether the identified instability advancement and frequency-locking regimes persist under broadband excitation or if the system transitions toward a more transient-dominant response.

- **Extension to multi-degree-of-freedom and flexible systems:** The current work employed a one-DOF pitch-only configuration to decouple and isolate the fundamental stall-flutter mechanisms. However, the introduction of additional degrees of freedom—such as plunge (heave) or spanwise bending—would better represent the coupled dynamics of real aircraft wings. Future research should examine how gust-induced phase lags between degrees of freedom influence the net energy ex-

change between the fluid and the structure, potentially uncovering more complex bifurcations and multi-mode interactions.

- **Quantification of 3D spanwise effects and finite-wing aerodynamics:** The 3D LES results in this research underscored the necessity of resolving spanwise flow physics to capture nonlinear load features like secondary lift loops. Expanding this into experimental studies on finite-span wings would allow for the investigation of how gust-induced stall cells interact with tip vortices and spanwise-varying mode shapes. This is of particular relevance to the design of high-aspect-ratio wings for long-endurance UAVs, where structural flexibility and large-scale separation are highly coupled.

- **Development of active gust-mitigation controllers:** The validated van der Pol and Mathieu–van der Pol ROMs developed in this study provide a computationally efficient foundation for control synthesis. Future work could leverage these models to develop "envelope-aware" aeroservoelastic control strategies. By utilizing actuators such as fast-acting flaps or synthetic jets, these controllers could be specifically tuned to disrupt the 1:1 and 2:1 lock-in bands discovered in this research, thereby restoring stability margins and ensuring structural integrity in unsteady urban environments.

References

[1] T. Theodorsen, "General theory of aerodynamic instability and the mechanism of flutter," National Advisory Committee for Aeronautics, Langley Field, VA, Tech. Rep. NACA Report 496, 1935. [Online]. Available: https://ntrs.nasa.gov/citations/19930090935.

[2] H. Wagner, "Über die entstehung des dynamischen auftriebes von tragflügeln," *Zeitschrift für Angewandte Mathematik und Mechanik (ZAMM)*, vol. 5, no. 1, pp. 17–35, 1925. DOI: 10.1002/zamm.19250050103.

[3] H. G. Küssner, "Zusammenfassender bericht über den instationären auftrieb von flügeln," *Luftfahrtforschung*, vol. 13, pp. 410–424, 1936.

[4] W. R. Sears, "Some aspects of non-stationary airfoil theory and its practical application," *Journal of the Aeronautical Sciences*, vol. 8, no. 3, pp. 104–108, 1941. DOI: 10.2514/8.10655.

[5] S. J. Corkery, "Unsteady aerodynamics of wing-gust encounters," Ph.D. dissertation, University of Cambridge, 2019. DOI: 10.17863/CAM.43887.

[6] S. J. Corkery, H. Babinsky, and J. K. Harvey, "On the development and early observations from a towing tank-based transverse wing–gust encounter test rig," *Experiments in Fluids*, vol. 59, 2018, Art. no. 135. DOI: 10.1007/s00348-018-2586-0.

[7] H. Biler, C. Badrya, and A. R. Jones, "Experimental and computational investigation of transverse gust encounters," *AIAA Journal*, vol. 57, no. 11, pp. 4608–4622, 2019. DOI: 10.2514/1.J057646.

[8] X. Zhang, M. Kheiri, and W. F. Xie, "Nonlinear dynamics and gust response of a two-dimensional wing," *International Journal of Non-Linear Mechanics*, vol. 123, 2020, Art. no. 103478. DOI: 10.1016/j.ijnonlinmec.2020.103478.

[9] X. Zhang, M. Kheiri, and W. F. Xie, "Aeroservoelasticity of an airfoil with parametric uncertainty and subjected to atmospheric gusts," *AIAA Journal*, vol. 59, no. 11, pp. 4326–4341, 2021. DOI: 10.2514/1.J060089.

[10] D. Poirel and S. Price, "Post-instability behavior of a structurally nonlinear airfoil in longitudinal turbulence," *Journal of Aircraft*, vol. 34, no. 5, pp. 619–626, 1997. DOI: 10.2514/2.2238.

[11] D. Poirel and S. Price, "Structurally nonlinear fluttering airfoil in turbulent flow," *AIAA Journal*, vol. 39, no. 10, pp. 1960–1968, 2001. DOI: 10.2514/2.1186.

[12] J Farnsworth, D Sinner, D Gloutak, L Droste, and D Bateman, "Design and qualification of an unsteady low-speed wind tunnel with an upstream louver system," *Experiments in Fluids*, vol. 61, no. 8, 2020, Art. no. 181. DOI: 10.1007/s00348-020-03018-1.

[13] K. Fukami and K. Taira, "Grasping extreme aerodynamics on a low-dimensional manifold," *Nature Communications*, vol. 14, 2023, Art. no. 6480. DOI: 10.1038/s41467-023-42213-6.

[14] C. J. Barnes and M. R. Visbal, "Gust response of rigid and elastically mounted airfoils at a transitional Reynolds number," *Aerospace Science and Technology*, vol. 74, pp. 112–119, 2018. DOI: 10.1016/j.ast.2017.12.025.

[15] C. J. Barnes and M. R. Visbal, "Angle of attack and core size effects on transitional vortical-gust–airfoil interactions," *AIAA Journal*, vol. 58, no. 7, pp. 2881–2898, 2020. DOI: 10.2514/1.J058654.

[16] G. Sedky, F. D. Lagor, and A. Jones, "Unsteady aerodynamics of lift regulation during a transverse gust encounter," *Physical Review Fluids*, vol. 5, no. 7, 2020, Art. no. 074701. DOI: 10.1103/PhysRevFluids.5.074701.

[17] G. Sedky, A. Gementzopoulos, I. Andreu-Angulo, F. D. Lagor, and A. R. Jones, "Physics of gust response mitigation in open-loop pitching manoeuvres," *Journal of Fluid Mechanics*, vol. 944, no. A38, 2022. DOI: 10.1017/jfm.2022.509.

[18] I. Andreu-Angulo and H. Babinsky, "Controlling upwards and downwards gust loads on aerofoils by pitching," *Experiments in Fluids*, vol. 64, no. 7, 2023, Art. no. 129. DOI: 10.1007/s00348-023-03670-3.

[19] W. Yuan, X. Zhang, D. Poirel, and A. Wall, "Numerical modelling of aerodynamic response to gusts and gust effect mitigation," *Aerospace Science and Technology*, vol. 154, 2024, Art. no. 109467, ISSN: 1270-9638. DOI: 10.1016/j.ast.2024.109467.

[20] D. M. Tang, P. Cizmas, and E. H. Dowell, "Experiments and analysis for a gust generator in a wind tunnel," *Journal of Aircraft*, vol. 33, no. 1, pp. 139–148, 1996. DOI: 10.2514/3.46914.

[21] H. Mai, J. Neumann, and H. Hennings, "Gust response: A validation experiment and preliminary numerical simulations," in *Proceedings of the 15th International Forum on Aeroelasticity and Structural Dynamics (IFASD)*, 2011.

[22] V. Brion *et al.* "Generation of vertical gusts in a transonic wind tunnel," *Experiments in Fluids*, vol. 56, 2015, Art. no. 145. DOI: 10.1007/s00348-015-2016-5.

[23] A. J. Saddington, M. V. Finnis, and K. Knowles, "The characterisation of a gust generator for aerodynamic testing," *Proceedings of the Institution of Mechanical Engineers, Part G: Journal of Aerospace Engineering*, vol. 229, no. 7, pp. 1214–1225, 2015. DOI: 10.1177/0954410014548237.

[24] K. T. Wood, R. C. Cheung, T. S. Richardson, J. E. Cooper, O. Darbyshire, and C. Warsop, "A new gust generator for a low speed wind tunnel: Design and commissioning," in *55th AIAA Aerospace Sciences Meeting*, 2017, 0502. DOI: 10.2514/6.2017-0502.

[25] P. Lancelot, J. Sodja, N. Werter, and R. De Breuker, "Design and testing of a low subsonic wind tunnel gust generator," *Advances in Aircraft and Spacecraft Science*, vol. 4, no. 2, pp. 125–144, 2017. DOI: 10.12989/aas.2017.4.2.125.

[26] N. T. Nguyen, J. Xiong, and N. B. Cramer, "Simulation and modeling of flow generated by gust generator in a wind tunnel," in *AIAA SciTech 2020 Forum*, 2020, 0212. DOI: 10.2514/6.2020-0212.

[27] D. A. Olson, A. M. Naguib, and M. M. Koochesfahani, "Development of a low-turbulence transverse-gust generator in a wind tunnel," *AIAA Journal*, vol. 59, no. 5, pp. 1575–1584, 2021. DOI: 10.2514/1.J059962.

[28] G. Perrotta and A. R. Jones, "Unsteady forcing on a flat-plate wing in large transverse gusts," *Experiments in Fluids*, vol. 58, 2017, Art. no. 101. DOI: 10.1007/s00348-017-2385-z.

[29] K. Granlund, B. Monnier, M. Ol, and D. Williams, "Airfoil longitudinal gust response in separated vs. attached flows," *Physics of Fluids*, vol. 26, no. 2, 2014, Art. no. 027103. DOI: 10.1063/1.4864338.

[30] R. L. Bisplinghoff, H. Ashley, and R. L. Halfman, *Aeroelasticity*. Addison-Wesley Publishing Company, 1955.

[31] Y.-C. Fung, *An introduction to the theory of aeroelasticity*. Wiley, 1955.

[32] T. von Karman and W. R. Sears, "Airfoil theory for non-uniform motion," *Journal of the Aeronautical Sciences*, vol. 5, no. 10, pp. 379–390, 1938. DOI: 10.2514/8.674.

[33] B. P. Epps and B. T. Roesler, "Vortex sheet strength in the Sears, Küssner, Theodorsen, and Wagner aerodynamics problems," *AIAA Journal*, vol. 56, no. 3, pp. 889–904, 2018. DOI: 10.2514/1.J056399.

[34] J. R. Wright and J. E. Cooper, *Introduction to Aircraft Aeroelasticity and Loads*. Chichester, UK: John Wiley & Sons, 2008, ISBN: 978-0470858400.

[35] R. Isaacs, "Airfoil theory for flows of variable velocity," *Journal of the Aeronautical Sciences*, vol. 12, no. 1, pp. 113–117, 1945. DOI: 10.2514/8.11202.

[36] J. M. Greenberg, "Airfoil in sinusoidal motion in a pulsating stream," National Advisory Committee for Aeronautics, Washington, DC, Tech. Rep. NACA-TN-1326, 1947. [Online]. Available: https://ntrs.nasa.gov/citations/19930082084.

[37] B. G. van der Wall and J. G. Leishman, "On the influence of time-varying flow velocity on unsteady aerodynamics," *Journal of the American Helicopter Society*, vol. 39, no. 4, pp. 25–36, 1994. DOI: 10.4050/JAHS.39.25.

[38] T. Wang, L. H. Feng, Y. T. Cao, and J. J. Wang, "Airfoil response to periodic vertical and longitudinal gusts," *Journal of Fluid Mechanics*, vol. 979, 2024, Art. no. A35. DOI: 10.1017/jfm.2023.1000.

[39] S. J. Corkery and H. Babinsky, "An investigation into gust shear layer vorticity and the added mass force for a transverse wing-gust encounter," in *AIAA SciTech 2019 Forum*, 2019, AIAA 2019–1145. DOI: 10.2514/6.2019-1145.

[40] R. Stevens, C. Pitt Ford, and H. Babinsky, "Experimental studies of an accelerating, pitching, flat-plate at low Reynolds number," in *51st AIAA Aerospace Sciences Meeting including the New Horizons Forum and Aerospace Exposition*, 2013, 677. DOI: 10.2514/6.2013-677.

[41] R. J. Stevens and H. Babinsky, "Low Reynolds number experimental studies on flat plates," in *52nd Aerospace Sciences Meeting*, 2014, 0743. DOI: 10.2514/6.2014-0743.

[42] S. J. Corkery, H. Babinsky, and W. R. Graham, "Quantification of added-mass effects using particle image velocimetry data for a translating and rotating flat plate," *Journal of Fluid Mechanics*, vol. 870, pp. 492–518, 2019. DOI: 10.1017/jfm.2019.231.

[43] W. J. McCroskey, L. W. Carr, and K. W. McAlister, "Dynamic stall experiments on oscillating airfoils," *AIAA Journal*, vol. 14, no. 1, pp. 57–63, 1976. DOI: 10.2514/3.61332.

[44] L. W. Carr, K. W. McAlister, and W. J. McCroskey, "Analysis of the development of dynamic stall based on oscillating airfoil experiments," National Aeronautics and Space Administration, Washington, DC, Tech. Rep. NASA TN D-8382, 1977. [Online]. Available: https://ntrs.nasa.gov/citations/19770010056.

[45] W. J. McCroskey, "The phenomenon of dynamic stall," NASA Ames Research Center, Moffett Field, CA, Tech. Rep. NASA TM-81264, 1981. [Online]. Available: https://ntrs.nasa.gov/citations/19810011501.

[46] L. W. Carr, "Progress in analysis and prediction of dynamic stall," *Journal of Aircraft*, vol. 25, no. 1, pp. 6–17, 1988. DOI: 10.2514/3.45534.

[47] L. W. Carr and M. S. Chandrasekhara, "Compressibility effects on dynamic stall," *Progress in Aerospace Sciences*, vol. 32, no. 6, pp. 523–573, 1996. DOI: 10.1016/0376-0421(95)00009-7.

[48] M. R. Visbal and D. J. Garmann, "Analysis of dynamic stall on a pitching airfoil using high-fidelity large-eddy simulations," *AIAA Journal*, vol. 56, no. 1, pp. 46–63, 2017. DOI: 10.2514/1.J056108.

[49] S. I. Benton and M. R. Visbal, "The onset of dynamic stall at a high, transitional Reynolds number," *Journal of Fluid Mechanics*, vol. 861, pp. 860–885, 2019. DOI: 10.1017/jfm.2018.939.

[50] J. Z. Wu, X. Y. Lu, A. G. Denny, M. Fan, and J. M. Wu, "Post-stall flow control on an airfoil by local unsteady forcing," *Journal of Fluid Mechanics*, vol. 371, pp. 21–58, 1998. DOI: 10.1017/S0022112098002055.

[51] R. Miotto, W. Wolf, D. Gaitonde, and M. R. Visbal, "Analysis of the onset and evolution of a dynamic stall vortex on a periodic plunging aerofoil," *Journal of Fluid Mechanics*, vol. 938, 2022, Art. no. A24. DOI: 10.1017/jfm.2022.165.

[52] J. G. Leishman and T. S. Beddoes, "A semi-empirical model for dynamic stall," *Journal of the American Helicopter Society*, vol. 34, no. 3, pp. 3–17, 1989. DOI: 10.4050/JAHS.34.3.3.

[53] J. Boutet, G. Dimitriadis, and X. Amandolese, "A modified Leishman–Beddoes model for airfoil sections undergoing dynamic stall at low Reynolds numbers," *Journal of Fluids and Structures*, vol. 93, 2020, Art. no. 102852. DOI: 10.1016/j.jfluidstructs.2019.102852.

[54] G. Bangga, S. Parkinson, and W. Collier, "Development and validation of the IAG dynamic stall model in state-space representation for wind turbine airfoils," *Energies*, vol. 16, no. 10, 2023, Art. no. 3994. DOI: 10.3390/en16103994.

[55] Z. Shi, C. Gao, and W. Zhang, "Data-knowledge-driven dynamic stall modeling guided by stall patterns and semi-empirical model," *Physics of Fluids*, vol. 37, no. 4, 2025, Art. no. 045106. DOI: 10.1063/5.0263116.

[56] Y.-T. Cao and L.-H. Feng, "Gust response of an airfoil with a flexible trailing edge," *Physics of Fluids*, vol. 37, no. 1, 2025, Art. no. 017161. DOI: 10.1063/5.0251878.

[57] L. G. P. Dos Santos and F. D. Marques, "Nonlinear aeroelastic analysis of airfoil section under stall flutter oscillations and gust loads," *Journal of Fluids and Structures*, vol. 102, 2021, Art. no. 103250. DOI: 10.1016/j.jfluidstructs.2021.103250.

[58] R. L. Halfman, H. C. Johnson, and S. M. Haley, "Evaluation of high-angle-of-attack aerodynamic-derivative data and stall-flutter prediction techniques," National Advisory Committee for Aeronautics, Washington, DC, Tech. Rep. NACA-TN-2533, 1951. [Online]. Available: https://ntrs.nasa.gov/citations/19930083408.

[59] D. Poirel and F. Mendes, "Experimental small-amplitude self-sustained pitch–heave oscillations at transitional Reynolds numbers," *AIAA Journal*, vol. 52, no. 8, pp. 1581–1590, 2014. DOI: 10.2514/1.J052541.

[60] L. Goyaniuk, D. Poirel, and A. Benaïssa, "Pitch–heave symmetric stall flutter of a NACA0012 at transitional Reynolds numbers," *AIAA Journal*, vol. 58, no. 8, pp. 3286–3298, 2020. DOI: 10.2514/1.J059008.

[61] D. Poirel, L. Goyaniuk, and A. Benaïssa, "Frequency lock-in in pitch–heave stall flutter," *Journal of Fluids and Structures*, vol. 79, pp. 14–25, 2018. DOI: 10.1016/j.jfluidstructs.2018.01.006.

[62] R. F. Huang and C. L. Lin, "Vortex shedding and shear-layer instability of wing at low-Reynolds numbers," *AIAA Journal*, vol. 33, no. 8, pp. 1398–1403, 1995. DOI: 10.2514/3.12561.

[63] R. F. Huang, W. W. Shy, S. W. Lin, and F. B. Hsiao, "Influence of surface flow on aerodynamic loads of a cantilever wing," *AIAA Journal*, vol. 34, no. 3, pp. 527–532, 1996. DOI: 10.2514/3.13100.

[64] T. Lutz, W. Würz, and S. Wagner, "Numerical optimization and wind-tunnel testing of low reynolds-number airfoils," in *Fixed and Flapping Wing Aerodynamics for Micro Air Vehicle Applications*, ser. Progress in Astronautics and Aeronautics, vol. 195, Reston, VA: American Institute of Aeronautics and Astronautics, 2001, pp. 169–190. DOI: 10.2514/5.9781600866654.0169.0190.

[65] D. Poirel, Y. Harris, and A. Benaïssa, "Self-sustained aeroelastic oscillations of a NACA0012 airfoil at low-to-moderate Reynolds numbers," *Journal of Fluids and Structures*, vol. 24, no. 5, pp. 700–719, 2008. DOI: 10.1016/j.jfluidstructs.2007.11.005.

[66] D. Poirel and W. Yuan, "Aerodynamics of laminar separation flutter at a transitional Reynolds number," *Journal of Fluids and Structures*, vol. 26, no. 7-8, pp. 1174–1194, 2010. DOI: 10.1016/j.jfluidstructs.2010.06.005.

[67] W. Yuan, D. Poirel, and B. Wang, "Simulations of pitch–heave limit-cycle oscillations at a transitional Reynolds number," *AIAA Journal*, vol. 51, no. 7, pp. 1716–1732, 2013. DOI: 10.2514/1.J052225.

[68] W. Yuan, D. Poirel, B. Wang, and A. Benaissa, "Effect of freestream turbulence on airfoil limit-cycle oscillations at transitional reynolds numbers," *Journal of Aircraft*, vol. 52, no. 4, pp. 1214–1225, 2015. DOI: 10.2514/1.C032807.

[69] R. B. Langtry and F. R. Menter, "Correlation-based transition modeling for unstructured parallelized computational fluid dynamics codes," *AIAA Journal*, vol. 47, no. 12, pp. 2894–2906, 2009. DOI: 10.2514/1.42362.

[70] S. H. Strogatz, *Nonlinear Dynamics and Chaos: With Applications to Physics, Biology, Chemistry, and Engineering*. Reading, MA: Addison-Wesley, 1994, ISBN: 978-0201543445.

[71] E. H. Dowell, H. C. Curtiss Jr, R. H. Scanlan, and F. Sisto, *A Modern Course in Aeroelasticity*. Alphen aan den Rijn, The Netherlands: Sijthoff & Noordhoff, 1978, ISBN: 9028600574.

[72] M. L. Facchinetti, E. De Langre, and F. Biolley, "Coupling of structure and wake oscillators in vortex-induced vibrations," *Journal of Fluids and Structures*, vol. 19, no. 2, pp. 123–140, 2004. DOI: 10.1016/j.jfluidstructs.2003.12.004.

[73] A. Pikovsky, M. Rosenblum, and J. Kurths, *Synchronization: A Universal Concept in Nonlinear Sciences* (Cambridge Nonlinear Science Series). Cambridge: Cambridge University Press, 2001, vol. 12. DOI: 10.1017/CBO9780511755743.

[74] A. H. Nayfeh and D. T. Mook, *Nonlinear Oscillations*. New York: John Wiley & Sons, 1979, ISBN: 978-0471035558.

[75] C. Feng, "The measurement of vortex induced effects in flow past stationary and oscillating circular and d-section cylinders," M.S. thesis, University of British Columbia, 1968.

[76] A. Khalak and C. H. Williamson, "Motions, forces and mode transitions in vortex-induced vibrations at low mass-damping," *Journal of Fluids and Structures*, vol. 13, no. 7-8, pp. 813–851, 1999. DOI: 10.1006/jfls.1999.0236.

[77] Z. Hong, X. Wang, X. Jing, and X. Sun, "Frequency lock-in mechanism in flow-induced acoustic resonance of a cylinder in a flow duct," *Journal of Fluid Mechanics*, vol. 884, 2020, Art. no. A42. DOI: 10.1017/jfm.2019.966.

[78] L Tregidgo, Z. Wang, and I Gursul, "Frequency lock-in phenomenon for self-sustained roll oscillations of rectangular wings undergoing a forced periodic pitching motion," *Physics of Fluids*, vol. 24, no. 11, 2012. DOI: 10.1063/1.4767468.

[79] E. H. Dowell, J. Doherty, M. Joshi, M. Sharma, R. Kielb, and M. Rauseo, "Investigation of the nonlinear interaction of a flutter/limit cycle oscillation of a cantilevered wing with a gust excitation," in *AIAA SciTech 2019 Forum*, 2019, AIAA 2019–1862. DOI: 10.2514/6.2019-1862.

[80] R. E. Sheldahl and P. C. Klimas, "Aerodynamic characteristics of seven symmetrical airfoil sections through 180-degree angle of attack for use in aerodynamic analysis of vertical axis wind turbines," Sandia National Labs., Albuquerque, NM (USA), Tech. Rep., 1981. DOI: 10.2172/6548367.

[81] H. H. Bruun, *Hot-wire Anemometry: Principles and Signal Analysis*. Oxford: Oxford University Press, 1995, ISBN: 978-0198563426.

[82] P. Lancelot, J. Sodja, and R. De Breuker, "Investigation of the unsteady flow over a wing under gust excitation," in *17th International Forum on Aeroelasticity and Structural Dynamics*, International Forum on Aeroelasticity and Structural Dynamics (IFASD), 2017, IFASD–2017.

[83] W. C. Young, R. G. Budynas, and A. M. Sadegh, *Roark's Formulas for Stress and Strain*. McGraw-Hill Education, 2012.

[84] S. Yarusevych, P. E. Sullivan, and J. G. Kawall, "On vortex shedding from an airfoil in low-Reynolds-number flows," *Journal of Fluid Mechanics*, vol. 632, pp. 245–271, 2009. DOI: 10.1017/S0022112009007058.

[85] A. Benaïssa, S. Biskri, L. Goyaniuk, D. Poirel, and N. N. Bouda, "Beating phenomenon in frequency lock-in 2DOF stall flutter," *Journal of Fluids and Structures*, vol. 100, 2021, Art. no. 103176. DOI: 10.1016/j.jfluidstructs.2020.103176.

[86] L. Goyaniuk, D. Poirel, A. Benaïssa, and H. Amari, "The energy extraction potential from pitch-heave coupled flutter," *Journal of Sound and Vibration*, vol. 555, 2023, Art. no. 117714, ISSN: 0022-460X. DOI: 10.1016/j.jsv.2023.117714.

[87] M. Sytsma and L. Ukeiley, "Wind tunnel generated turbulence," in *49th AIAA Aerospace Sciences Meeting including the New Horizons Forum and Aerospace Exposition*, 2011, 1159. DOI: 10.2514/6.2011-1159.

[88] A. R. Jones, O. Cetiner, and M. J. Smith, "Physics and modeling of large flow disturbances: Discrete gust encounters for modern air vehicles," *Annual Review of Fluid Mechanics*, vol. 54, no. 1, pp. 469–493, 2022. DOI: 10.1146/annurev-fluid-031621-085520.

[89] N. Gregory and C. L. O'Reilly, "Low-speed aerodynamic characteristics of NACA 0012 aerofoil section, including the effects of upper-surface roughness simulating hoar frost," Aeronautical Research Council, London, Tech. Rep. 3726, 1970, Also issued as NPL Aero Report 1308. [Online]. Available: https://reports.aerade.cranfield.ac.uk/handle/1826.2/3003.

[90] W. Yuan, X. Zhang, and D. Poirel, "Numerical investigation of aerodynamic response to gust including gust-induced dynamic stall," in *AIAA Aviation 2024 Forum*, 2024, 4475. DOI: 10.2514/6.2024-4475.

[91] G. I. Taylor, "The spectrum of turbulence," *Proceedings of the Royal Society of London. Series A-Mathematical and Physical Sciences*, vol. 164, no. 919, pp. 476–490, 1938. DOI: 10.1098/rspa.1938.0032.

[92] X. Zhang, D. Poirel, A. Benaïssa, and W. Yuan, "Aerodynamic response to transverse gusts in pre-and post-stall regimes," in *AIAA SCITECH 2024 Forum*, 2024, p. 0079. DOI: 10.2514/6.2024-0079.

[93] D. C. Montgomery and G. C. Runger, *Applied statistics and probability for engineers*. John Wiley & Sons, 2010.

[94] K. Mulleners and M. Raffel, "The onset of dynamic stall revisited," *Experiments in Fluids*, vol. 52, no. 3, pp. 779–793, 2012. DOI: 10.1007/s00348-011-1118-y.

[95] G. Dimitriadis and J. Li, "Bifurcation behavior of airfoil undergoing stall flutter oscillations in low-speed wind tunnel," *AIAA Journal*, vol. 47, no. 11, pp. 2577–2596, 2009. DOI: 10.2514/1.39571.

[96] R. H. Rand, *Lecture Notes on Nonlinear Vibrations*. Ithaca, NY: The Internet-First University Press, 2012, Version 53. [Online]. Available: http://hdl.handle.net/1813/28989.

[97] A. Pikovsky, M. Rosenblum, and J. Kurths, "Phase synchronization in regular and chaotic systems," *International Journal of Bifurcation and Chaos*, vol. 10, no. 10, pp. 2291–2305, 2000. DOI: 10.1142/S0218127400001481.

[98] D Poirel and S. Price, "Random binary (coalescence) flutter of a two-dimensional linear airfoil," *Journal of Fluids and Structures*, vol. 18, no. 1, pp. 23–42, 2003. DOI: 10.1016/S0889-9746(03)00074-4.

[99] M. Pandey, R. H. Rand, and A. T. Zehnder, "Frequency locking in a forced Mathieu–van der Pol–Duffing system," *Nonlinear Dynamics*, vol. 54, no. 1, pp. 3–12, 2008. DOI: 10.1007/s11071-007-9238-x.

[100] F Veerman and F Verhulst, "Quasiperiodic phenomena in the van der pol–mathieu equation," *Journal of Sound and Vibration*, vol. 326, no. 1-2, pp. 314–320, 2009. DOI: 10.1016/j.jsv.2009.04.040.

[101] J. A. Sanders, F. Verhulst, and J. Murdock, *Averaging Methods in Nonlinear Dynamical Systems* (Applied Mathematical Sciences), 2nd. New York: Springer, 2007, vol. 59, ISBN: 978-0-387-48916-2. DOI: 10.1007/978-0-387-48918-6.

Appendix A

Publication Record

Journal Publications During PhD Candidacy

1. **Xiaoyang Zhang**, Dominique Poirel, and Weixing Yuan. Lock-in during stall flutter under parametric excitation by harmonic longitudinal gusts. *Journal of Fluid Mechanics*, under revision, 2026.

2. **Xiaoyang Zhang**, Dominique Poirel, and Weixing Yuan. Lock-in during stall flutter forced by periodic transverse gusts. *Journal of Fluids and Structures*, under review, 2026.

3. **Xiaoyang Zhang**, Dominique Poirel, and Weixing Yuan. Dynamic stall induced by a periodic transverse gust of an airfoil at transitional Reynolds numbers. *Physics of Fluids*, vol. 37, no. 12, 2025.

4. Weixing Yuan, **Xiaoyang Zhang**, Dominique Poirel, and Alanna Wall. Numerical modeling of aerodynamic response to gusts and gust effect mitigation. *Aerospace Science and Technology*, vol. 154, Art. no. 109467, 2024.

5. Weixing Yuan and **Xiaoyang Zhang**. Numerical stabilization for flutter analysis procedure. *Aerospace*, vol. 10, no. 3, Art. no. 302, 2023.

Conference Proceedings/Presentations During PhD Candidacy

1. **Xiaoyang Zhang**, Dominique Poirel, and Weixing Yuan. Stall flutter response to longitudinal gusts at transitional Reynolds numbers. *The 7th Symposium on Flow-Induced Vibration and Fluid-Structure Interaction (FSSIC 2025)*, Oshawa, ON, 2025.

2. **Xiaoyang Zhang**, Weixing Yuan, and Dominique Poirel. Numerical investigation on transverse-gust-induced dynamic stall. *CSME-CFDSC-CSR 2025 Congress*, Montreal, QC, 2025.

3. **Xiaoyang Zhang**, Dominique Poirel, and Weixing Yuan. Parametric study on gust-forced stall flutter. *The 6th International Conference on Experimental Fluid Mechanics (ICEFM 2025)*, Niagara-on-the-Lake, ON, 2025.

4. **Xiaoyang Zhang**, Dominique Poirel, and Weixing Yuan. Experimental investigation of lock-in during stall flutter forced by transverse harmonic gust. *AIAA SciTech 2025 Forum*, Orlando, FL, 2025.

5. Weixing Yuan, **Xiaoyang Zhang**, Dominique Poirel. Numerical investigation of aerodynamic response to gust including gust-induced dynamic stall. *AIAA Aviation Forum and ASCEND 2024*, Las Vegas, NV, 2024.

6. **Xiaoyang Zhang**, Dominique Poirel, and Weixing Yuan. Comprehensive investigation on gust-induced dynamic stall. *CSME-CFD 2024 Congress*, Toronto, ON, 2024.

7. **Xiaoyang Zhang**, Dominique Poirel, Azemi Benaïssa, and Weixing Yuan. Aerodynamic response to transverse gusts in pre- and post-stall regimes. *AIAA SciTech 2024 Forum*, Orlando, FL, 2024.

8. **Xiaoyang Zhang**, Dominique Poirel, Azemi Benaïssa, and Weixing Yuan. Dynamic stall induced by harmonic gust. *CASI AERO 2023 Conference*, Ottawa, ON, 2023.

9. **Xiaoyang Zhang**, Dominique Poirel, Azemi Benaïssa, and Weixing Yuan. Study of the wake flow downstream of two oscillating vanes. *CSME-CFD 2023 Congress*, Sherbrooke, QC, 2023.

10. Weixing Yuan, Alanna Wall, **Xiaoyang Zhang**, Dominique Poirel (2022). *Numerical modelling of pitching wings for gust mitigation. ICAS 2022 Congress*, Stockholm, Sweden, 2022.

11. **Xiaoyang Zhang**, Dominique Poirel, and Weixing Yuan. Numerical simulation of gust response of a one-DOF wing in stall flutter. *CASI AERO 2021 Conference (Virtual)*, 2021.

12. Weixing Yuan, **Xiaoyang Zhang**, Dominique Poirel. Flutter analysis solution stabilization for the PK-method. *AIAA Aviation 2021 Forum (Virtual)*, 2021.

13. Weixing Yuan, **Xiaoyang Zhang**, Dominique Poirel. Numerical modelling of aerodynamic response to gust. *AIAA SciTech 2021 Forum (Virtual)*, 2021.

Previous Publications Before PhD Candidacy

1. **Xiaoyang Zhang**, Mojtaba Kheiri, and Wen-Fang Xie. Aeroservoelasticity of an airfoil with parametric uncertainty and subjected to atmospheric gusts. *AIAA Journal*, vol. 59, no. 11, pp. 4326–4341, 2021.

2. **Xiaoyang Zhang**, Mojtaba Kheiri, and Wen-Fang Xie. Nonlinear dynamics and gust response of a two-dimensional wing. *International Journal of Non-Linear Mechanics*, vol. 123, Art. no. 103478, 2020.

3. **Xiaoyang Zhang**, Mojtaba Kheiri, and Wen-Fang Xie. Adaptive control of a two-dimensional nonlinear wing with structural stiffness and damping uncertainties. *The 27th Canadian Congress of Applied Mechanics (CANCAM)*, Sherbrooke, QC, 2019.

4. **Xiaoyang Zhang**, Mojtaba Kheiri, and Wen-Fang Xie. Active control of a two-dimensional nonlinear wing encountering a gust. *The 27th Canadian Congress of Applied Mechanics (CANCAM)*, Sherbrooke, QC, 2019.

5. **Xiaoyang Zhang**, Mojtaba Kheiri, and Wen-Fang Xie. Gust response of a two-dimensional nonlinear wing. *CSME International Congress*, Toronto, ON, 2018.